EXPERIMENTAL STUDY OF MULTIPHASE TURBULENT BUOYANT JETS AND THE FORMATION OF COMPOUND DROPLETS

by

Xinzhi Xue

A dissertation submitted to The Johns Hopkins University

in conformity with the requirements for the degree of

Doctor of Philosophy

Baltimore, Maryland

August, 2020

Abstract

Experimental techniques capable of yielding simultaneous measurements of both the carrier and dispersed phase is developed. First, the effects of dispersant concentrations on the droplet size distribution within a crude oil plume in crossflow are investigated using high-speed visualization and submerged inline holography. Increasing the dispersant concentration dramatically decreases the droplet sizes and reduces the rise rates of droplets and the upper boundary of the plume. In the near field, refractive-index matching liquid pairs, simultaneous planar laser-induced fluorescence, and particle image velocimetry are performed to elucidate the fragmentation and characterize the turbulence of a vertical buoyant oil jet. Close to the nozzle, as oil ligaments begin to extend outward, vortices form around their tips in the water. Further downstream, as the oil breaks up into droplets, some are compound, containing multiple water droplets, some with multilayers. Such droplets regularly form at moderate and high Re and persist for at least up to 30 nozzle diameters. In contrast, they rarely appear at low Re. The origin of some of the encapsulated water droplets can be traced back to the entrained water ligaments during the initial roll up of KH vortices. Analysis using random forest-based procedures shows that the fraction of compound droplets does

not vary significantly with *Re*, but increases rapidly with droplet diameter. Consequently, the size distributions of compound droplets have peaks that increase in magnitude and shift to a lower diameter with increasing *Re*. On average, the interior pockets raise the oil–water interfacial area by 15%, increasing with the diameter and axial location. Also, while the oil droplets are deformed by the jet's shear field, the interior interfaces remain nearly spherical. The spreading and decay rates of the jet centerline oil fraction are lower than those of the axial momentum. Comparison to a single-phase jet at the same *Re* shows that the transition from azimuthal shear layers to self-similar profiles of velocity and Reynolds stresses occur earlier in the oil jet. Phase-conditioned statistics in the oil jet reveal significant spatially varying discrepancies between the turbulence level in the oil and water phases. The peripheral turbulence in the water is higher near the jet exit, but lower after six diameters. The latter trend is attributed to the intermittency and lower peripheral shear-dominated turbulence production in the entrained water. In contrast, near the center, the production rate, hence the turbulent kinetic energy, is higher in the water. Here, while the axial contraction increases the turbulence in both phases, the radial extension in the spreading oil, as opposed to the radial contraction in the entrained water, causes a discrepancy in the production rates.

Primary Reader and Advisor: Dr. Joseph Katz

Secondary Reader: Dr. Rui Ni, Dr. Gretar Tryggvason

Acknowledgments

It would not be possible for me to complete this journey at the Johns Hopkins University without the inspiration and support from many individuals. First, I would like to express my sincere gratitude to my advisor, Dr. Joseph Katz, for his guidance and encouragement during my graduate study. His persistent emphasis on details and incisive comments on the experimental data and analyses have greatly influenced me and elevated my work. When I wandered off the course, he knows how to knock me back and motivate me to improve. Besides helping me become a better researcher, I also thank him for giving me the freedom to explore different aspects of my interest.

I would also like to thank Dr. Rui Ni and Dr. Gretar Tryggvason, for being on my thesis committee and reviewing this thesis. I benefit immensely from the help of many other faculties and staff as well. Among many, courses on various topics from Dr. Andrea Prosperetti, Dr. Charles Meneveau, Dr. Rajat Mittal, and Dr. Tamer Zaki prepared me well for research. I wish to thank Dr. Kirsten Koehler, Dr. Thomas Haine, Dr. Ciaran Harman, and Dr. Gretar Tryggvason for serving on my GBO committee. I thank Dr. Yury Ronzhes for helpful advices on the facility design and timely encouragement. I also like to thank Stephen King for help with electronics. I thank Dr. Steven Marra

Table of Contents

List of Tables

List of Figures

Chapter 1

Introduction

Immiscible multiphase buoyant jets and plumes, which consist of a momentum and buoyancy-driven dispersed phase (bubbles, droplets, or particles) discharged into a quiescent or co-flowing continuous phase, are important in a variety of engineering, biological and environmental processes. Some examples include spray atomization (Machicoane et al., 2019), virus transmission (Mittal, Ni, and Seo, 2020), volcanic eruption (Woods, 2010), and subsurface oil spill (Gros et al., 2017; Johansen, Brandvik, and Farooq, 2013; Zhao et al., 2016; Zheng, Yapa, and Chen, 2003). These multiphase jets and plumes have some different features than the miscible or single-phase jets and plumes (Charonko and Prestridge, 2017; Darisse, Lemay, and Benaïssa, 2015; Dowling and Dimotakis, 1990; Ezzamel, Salizzoni, and Hunt, 2015; Hussein, Capp, and George, 1994; Panchapakesan and Lumley, 1993a; Wang and Law, 2002). For miscible single-phase flow, the discharged fluid is irreversibly mixed at scales on which molecular diffusivity dominates (the Batchelor scale). Instead, multiphase jets

and plumes fragment near the discharge exit and contain distinct interfaces between two phases at scales that vary with the droplet size distributions. While there is little to no scalar mixing and density changes within each phase, the soluble components and momentum can still diffuse across the interfaces due to stresses, along with buoyancy- and interfacial tension-related instabilities (Mychkovsky and Ceccio, 2012; Stebe and Barthes-Biesel, 1995; Wegener et al., 2007).

The difficulties to simulate turbulent multiphase flows owing to the wide range of scales involved, and the challenges in measuring them are summarized in (Balachandar and Eaton, 2010). The breakup of immiscible liquid jets and plumes and resulting droplet size distributions have been studied extensively (Lin and Reitz, 1998; Villermaux, 2007), mostly focusing on the atomization of liquid jets in gas (Aliseda et al., 2008; Desjardins et al., 2013; Gorokhovski and Herrmann, 2008; Lasheras and Hopfinger, 2000; Lin and Reitz, 1998; Jarrahbashi et al., 2016; Marmottant and Villermaux, 2004; Shinjo and Umemura, 2010; Lowe, Kourmatzis, and Masri, 2017). Fragmentation of a buoyant immiscible liquid jet injected into another liquid, which is relevant e.g. to a subsurface oil well blowout, has received considerable attention after the Deepwater Horizon spill in the Gulf of Mexico. Experimental studies have shown that the droplet diameters vary from microns to millimeters, depending on the flow conditions and fluid properties, which are typically expressed in terms of the jet Weber (*We*) and Reynolds (*Re*) numbers (Johansen, Brandvik, and Farooq, 2013; Brandvik et al., 2018) as well as the density ratio, ρ_o/ρ_w, and viscosity ratio, μ_o/μ_w. Here, $We = \rho_o u_{mean}^2 d/\sigma$, $Re = \rho_o u_{mean} d/\mu_o$, ρ is

the density, u_{mean} is the jet mean velocity, d is the nozzle diameter, σ is the interfacial tension, μ is the viscosity, and the subscripts w and o refer to the continuous water and dispersed oil phase, respectively. In parallel, numerous numerical simulations have attempted to model the dispersion of the droplet plume under the influence of buoyancy, surrounding flow, turbulence, and stratification using prescribed droplet size distributions (Crounse, Wannamaker, and Adams, 2007; Socolofsky, Adams, and Sherwood, 2011; Yang et al., 2016).

The regimes of jet fragmentation, namely axisymmetric Rayleigh breakup, sinuous wave breakup and atomization, have been established for liquid jets in air (Lasheras and Hopfinger, 2000) and extended to oil-water systems based on the Reynolds and Ohnesorge numbers ($Oh = We^{1/2}/Re$), by Masutani and Adams, 2001. For low Re and Oh, Eggers, 1997 extends the classical Rayleigh-Plateau instability to non-linear slender jets. More recently, Homma et al., 2006 have used direct numerical simulations to capture and classify several breakup modes on a Weber number-viscosity ratio diagram. The processes involved at high Re are less clear, leading to introduction of e.g. statistical theories that describe the droplets size distribution based on sequential cascades of breakup and aggregation (Martínez-Bazán, Montanes, and Lasheras, 1999; Zhao et al., 2014b), or maximum entropy and random breakups (Cohen, 1990). These approaches do not account for the influence of flow structure and ligament dynamics, which are essential for explaining the differences between predicted and measured droplet size spectrum (Villermaux, 2007). Recently, Aiyer et al., 2019 extended the breakup kernel using a structure function model.

Factors affecting multiphase plume behavior may be divided into initial discharge characteristics and water column characteristics. The former include exit geometry, gas-to-oil ratio, and the droplet and bubble-size distributions resulting from the oil properties, discharge flow rate, and possible dispersant application. Water column characteristics include depth, ambient stratification, crossflow current, and turbulence. A change in any of these factors may alter the plume behavior and oil dispersion. For example, the addition of dispersants to the Deepwater Horizon blowout created much smaller and more slowly rising oil droplets which took longer to reach the surface. These tiny droplets can then be retained in plumes or intrusion layers, be swept much further downstream, and may biodegrade more before surfacing (North et al., 2011; Socolofsky et al., 2015; Aman et al., 2015).

For multiphase jet in crossflow, Zhang and Zhu, 2014 examine bubbly water jets in crossflow (without oil) as well as measure the plume trajectories and the bubble characteristics, which they also use for developing an empirical expression for the separation height. They show that the bubble size decreases with increasing water injection rate, and that the bubbles enhance the mixing rate with external water. Upon separation, their bubbles rise at terminal speed while being advected by the freestream flow. The separated plume has an elliptical cross section for a bubbly plume (injection of air only), and a kidney shape for a bubbly jet with equal injection rates of air and water. The latter is attributed to the counterrotating vortex pair (CVP) characterizing single-phase jets in crossflow (Smith and Mungal, 1998). In a dynamically similar system, Decrop et al., 2015 report on experiments and simulations of

inverted sediment plumes in crossflow containing 5 mm diameter, low Stokes number particles. The Stokes number is the ratio between the particle and turbulence time scales. They note the large-scale turbulent structures, which, in addition to the CVP, include wake vortices behind the plume, similar to those seen by Fric and Roshko, 1994 and Kelso, Lim, and Perry, 1996. The spatial distribution of sediment concentration and its vertical turbulent flux are linked to both large-scale features, with the wake structures transporting the sediment from the plume toward the water surface.

The coupling between the dispersed droplet and the surrounding flow turbulence are also associated by the droplets' geometrical and dynamic properties. Flows containing very small volume fractions ($\gamma \ll 1$) of small particles satisfying $D < \eta$, where D is the particle size and η is the Kolmogorov scale, have a continuous phase turbulence that is nearly the same as that of the single-phase counterparts (Squires and Eaton, 1990). However, at high volume fraction, or $D > \eta$, as typically occurs in the near field an immiscible liquid jet, the presence of a dispersed phase could either cause turbulence attenuation or enhancement (Feng and Bolotnov, 2017; Ferrand et al., 2003; Lee and Chu, 2012). The transfer of momentum and energy between phases in suspension laden flows can be affected by the shape, deformation of the dispersed phase, and the relative motions between the two phases (Bellani et al., 2012; Bunner and Tryggvason, 2003; Rensen and Roig, 2001). It is essential to understand and predict how the turbulence is generated and modulated by the addition of length and time scales associated with the immiscible interfaces. Such data would be beneficial for extending the classical theories for the mean

velocity, Reynolds stresses and self-similarity assumptions in jets and plumes (Morton, Taylor, and Turner, 1956; Turner, 1986) to more generalized non-Boussinesq multiphase models (Carlotti and Hunt, 2005; Dissanayake, Gros, and Socolofsky, 2018; Rooney and Linden, 1996; Reeuwijk and Craske, 2015).

Recent progress has led to a better understanding of the fragmentation, entrainment, and the evolution of droplet size distributions in liquid-liquid immiscible jets and plumes (Aiyer et al., 2019; Brandvik et al., 2019; Landeau, Deguen, and Olson, 2014; Saito, Abe, and Koyama, 2017). A comprehensive summary is provided in Boufadel et al., 2020. Conversely, there are very limited experimental data on the flow structure and turbulence in the near field of immiscible buoyant liquid jets in another liquid, such as oil jets in water, where phase-interactions, fragmentation, and droplet formation play dominant roles. Experimental observations on processes occurring in the near field of liquid-liquid jet breakup in the atomization regime is a challenge owing to optical obstruction. Consequently, the most available data are restricted to the periphery or far field of the jet where the droplet are rather sparse.

This thesis is structured in three parts: Chapter 2 presents an *in situ* holography measurement on the time evolution of droplet size distributions in a crude oil plume in crossflow with different dispersant concentrations. The effect of far-field droplet size spectrum on the plume trajectory will be briefly discussed. In the near field, Chapter 3 will elucidates several processes occurring during the near field fragmentation of a buoyant immiscible vertical oil jet injected into quiescent water. Unobstructed visual access is achieved by matching the refractive indices of the two fluids: silicone oil and sugar water. High speed

planar laser induced fluorescence (PLIF) will demonstrates several phenomena, most notably, the ubiquitous generation of compound oil droplets, which contain smaller water droplets. The mechanisms involved are demonstrated, followed by an analysis showing e.g. the fraction of compound droplets, their impact on the oil-water interfacial area, and the striking differences between the odd exterior shapes of the oil droplets and the nearly spherical interior water droplets. Chapter 4 will focus on the near field flow structures, the ensemble-averagedd phase and velocity distributions, the Reynolds stresses, turbulent intermittency, and the turbulence production rate of each phase in the fragmentation region of the vertical buoyant jet. Simultaneous Particle Image Velocimetry (PIV) and Planar Laser-Induced Fluorescence (PLIF) are used for probing this flow. Details of the experimental setup and image registration procedures will be presented. The streamwise evolution of the mean velocity profiles, root mean square (RMS) values of velocity fluctuations, and Reynolds shear stress will be discussed. The differences between the evolution of the oil volume fraction and mean momentum distribution will also be presented. Trends are compared with those of a single-phase jet at a very similar Reynolds number. Among the findings, the phase-conditioned turbulence statistics reveal a sizable difference between the mean velocity, turbulence level and the Reynolds shear stress, in the two phases along the periphery of the jet. It is demonstrated that the difference in peripheral turbulence can be linked to the intermittency of the water flow. Furthermore, partitioning of the terms contributing to the turbulence production indicate that shear production is the dominant term along the periphery of the jet, and that there is a significantly higher total production rate in the water near the center line

of the jet. Finally, the summary and conclusions are presented in Chapter 5.

Chapter 2

Holography measurements of on the droplet size distribution in a crude oil jets in crossflow

To study the effect of dispersant concentration on the plume and quantify the evolution of droplet size distributions in a crude oil jet transitioning into a plume in a crossflow, sychronized high speed visualization and submerged *in situ* digital inline holography imaging technique is deployed within the oil plume in crossflow. Section 2.1 provides the details of the experimental setup and the data processing techniques. The large-scale plume behavior will be presented in section 2.2, followed by the statistics and the evolution of droplet size distributions within the plume in section 2.3. A breif summary of the findings are provided in section 2.4.

2.1 Experimental techniques

Digital inline holography have been applied to measure the droplet-size distributions within the oil plume. The oil plume in cross flow have been conducted in a $2.5 \times 0.9 \times 0.9$ m (length $\times$ width $\times$ height) transparent acrylic towing tank (figures 2.1a and 2.1b). A carriage, driven by a stepper motor at speeds up to 200 mm/s, is mounted on rails located above the tank. This carriage supports a flow system for injection of crude oil, consisting of a regulated, nitrogen-pressurized oil reservoir, a solenoid valve, a variable area flowmeter (Omega, FL-6102A), and a streamlined injection arm leading to an upward pointing nozzle. The arm penetrates the water surface near the sidewall, ahead of the nozzle, descends to the bottom of the tank, and then extends to the center plane. A slotted rail with a low friction linear bearing supports the injection arm under the nozzle to facilitate smooth travel. Near the exit, a tube located inside the arm is connected to a 3-D printed injection nozzle that has a polished, cosine-shaped, converging interior surface, leading to a $d = 54$ mm diameter orifice. This orifice is located 14 cm above the tank floor. The tank is filled with artificial seawater (Instant Ocean) with a salinity of 33 ppt and density $\rho = 1018.3$ kg/m^3. Experiments have been conducted with crude oil alone, which is defined as the control case, and with crude oil-dispersant mixtures at dispersant to oil ratios (DOR) of 1:100 and 1:25. They are referred to as 1:100 DOR and and 1:25 DOR oils, respectively. The properties, namely density ρ, kinematic viscosity ν, and oil-water interfacial tension σ, of the present crude oils can be found in table 2.1. The methods used to measure them can be found in Murphy et al., 2015. The uncertainties
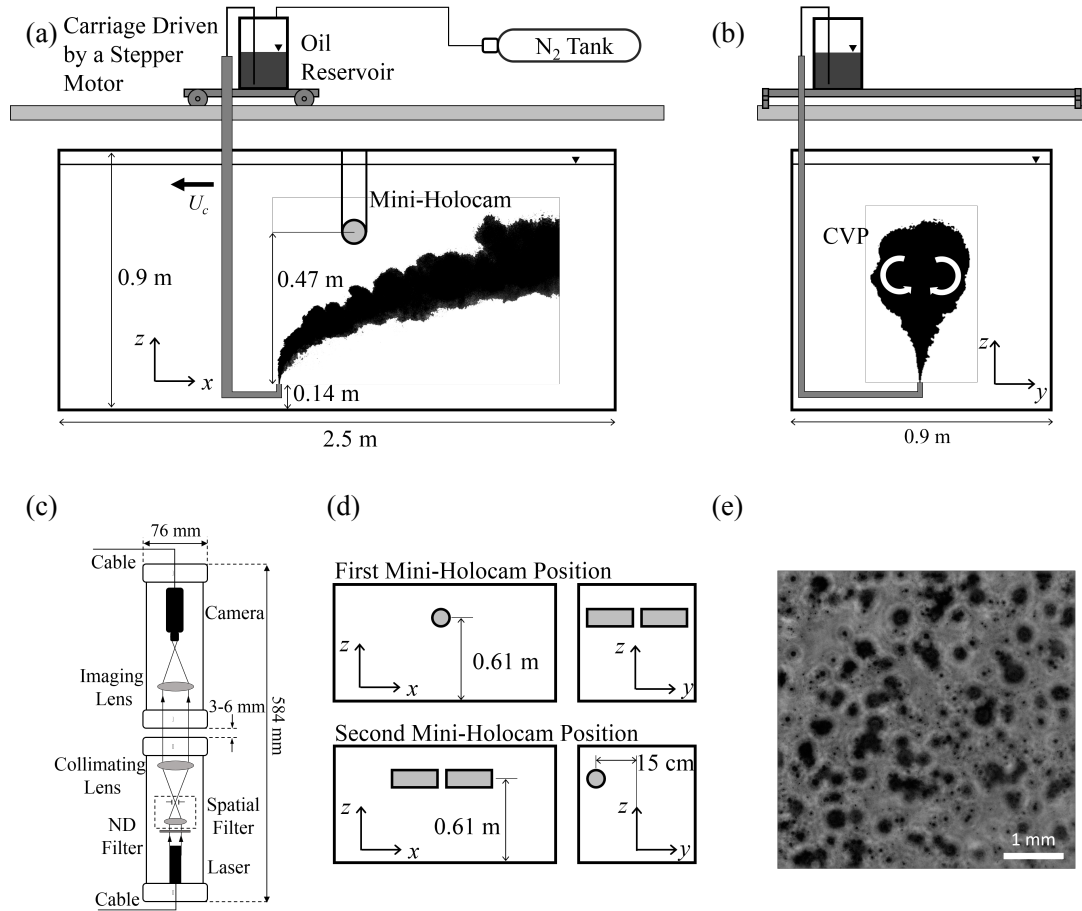
Figure 2.1: (a) A schematic drawing of the towing tank showing the carriage translating at speed U_c, a sample image of the plume, and the location of the submerged Mini-Holocam. (b) An end view of the towing tank illustrating the position of the counter-rotating vortex, (c) Optical components of the Mini-Holocam showing key dimensions, (d) Illustrations of the two Mini-Holocam positions within the tank, and (e) sample processed hologram of droplets within the plume (oil-dispersant mixture at 1:25 DOR).

	ρ (kg/m^3)	ν (m^2/s)	σ (N/m)	Re	We	Oh	d_{50} (μm)
Crude Oil	864	1.02×10^{-5}	1.9×10^{-2}	1000	1100	0.034	734
1:100 DOR	855	1.15×10^{-5}	1.2×10^{-3}	900	18000	0.15	275
1:25 DOR	867	1.22×10^{-5}	2.8×10^{-4}	800	77000	0.34	234
Miscible	893	1.28×10^{-5}	NA	800	NA	NA	NA

Table 2.1: Physical properties of the fluids used in the present experiments along with the values of Re, We, and Oh characterizing the jets, and the time-averaged volume median diameter d_{50}.

in property measurements reflect the standard deviation of measurements using different samples of Macondo surrogate crude oil obtained from BP. It is a so-called "dead oil", i.e., many of the most volatile dissolved gases have been removed. These fluids are injected at a flow rate of $Q = 1.9$ L/min, corresponding to a jet exit speed $u_j = 2.5$ m/s, and the carriage is towed at a speed of $U_c = 150$ mm/s, resulting in a jet speed to crossflow ratio of $u_j/U_c = 17$. The resulting values of the Reynolds number ($Re = \rho u d/m$), Weber number ($We = \rho u^2 d/\sigma$), and Ohnesorge number ($Oh = We^{1/2}/Re$) are also given in Table 1. Though the values of Re fall in the laminar regime for pipe flow, the values of Re and Oh for the oil jets fall in the atomization regime, $Oh > 18/Re$, for immiscible jets, in which the jet disintegrates into fine droplets shortly after injection Masutani and Adams, 2001. The current Re and Oh also fall near those of experiments performed by Brandvik et al., 2013; Brandvik et al., 2014 and Johansen, Brandvik, and Farooq, 2013, which also clearly show that the jet becomes atomized shortly after injection.

A high-speed camera (pco.dimax) equipped with a 28 mm lens (Nikon Nikkor) operating at 250 fps is used to visualize the large-scale plume behavior. The field of view and resolution in the nozzle plane are 0.62×0.62 m^2 and 305

mm/pixel, respectively. Backlighting, diffused by lining the tank wall with translucent bond paper, is provided by up to six 500 W halogen lamps. This test is also used for measuring the size of the largest droplets (>3 mm), since they rapidly rise above the predominantly opaque plume.

Digital inline holography is also applied to measure the droplet size distributions within the oil plume. These measurements are synchronized with high-speed imaging in order to relate the measured droplet sizes to the location and evolution of the large-scale plume. Background on digital holography and holographic microscopy can be found in Malkiel et al., 2003; Sheng, Malkiel, and Katz, 2006; Gopalan, Malkiel, and Katz, 2008; Katz and Sheng, 2010. The present digital holograms are recorded by the "Mini-Holocam" (figure 2.1c), a custom-built, submersible inline holography system, which is suspended in the tank in order to record data at high magnification within the opaque plume. It contains a 1 mW, 635 nm diode laser beam, which passes through an ND filter and a spatial filter with a 5 mm aperture, is focused by an 8 mm focal length doublet lens, and is then collimated to a 22 mm diameter beam. Using a Schneider imaging lens ($f = 2.8/35$ mm), the holograms are recorded at a magnification of 0.66 by a 2 Hz, miniature, 2592×1944 pixel CMOS camera that has a pixel size of 2.2 μm, resulting in a resolution of 4.03 mm/pixel. The laser and illuminating optics are mounted inside a sealed 70 mm diameter and 292 mm long aluminium tube with a glass window on one end. The imaging lens and CMOS camera are installed in an identical tube, and both are mounted on an optical rail, allowing adjustment of the sample volume depth between them. Choice of this depth is a compromise

between our desire to maximize the sample volume size and the opacity of the oil cloud, i.e., the dense microdroplet concentration, especially when dispersants are involved. For the present measurements, the gap between the two halves of the Mini-Holocam system is 6.06 mm for the crude oil, 3.00 mm for the 1:100 DOR, and 3.25 mm for the 1:25 DOR oil. Hence, they are only suitable for characterizing sub mm droplets. The sample volume dimensions are $4.9 \times 4.9 \times 16$ mm^3, $4.9 \times 4.9 \times 13$ mm^3, and $4.9 \times 4.9 \times 13$ mm^3 for the crude, 1:100 DOR and 1:25 DOR cases. The droplet-size distributions are normalized to account for differences in sample volume. The magnification of holographic measurements is calibrated in air prior to submerging it. Since the hologram plane imaged by the magnifying lens is located just inside the glass window, the magnification of this system remains valid when the Mini-Holocam is submerged. The Mini-Holocom is rigidly suspended from the tank lid in one of two positions. In the first (figure 2.1d), the optical and y axes are aligned, with the sample volume aligned with the tank centerline, 46.8 cm above the nozzle exit. In this position, the plume bulk is sampled as it rises through the sample volume. Results provide both the time-resolved droplet-size distributions, and, by temporally averaging the data, the bulk droplet-size distributions. In the second position (figure 2.1d), the elevation remains the same, but the system is rotated so the optical and x axes are aligned, and the sample volume center is offset from the tank-center plane by 15 cm. This latter position, for which only crude oil experiments will be presented, is selected to record the droplets trapped within the CVP, whose location is determined based on measurements described below. The high-speed camera operating concurrently is located outside of the tank, and records images

15

at 100 Hz, while being synchronized with the Mini-Holocam. The purpose of these observations is to correlate the droplet statistics with their location within the plume. The likely effect of the Mini-Holocam instrument on the flow structure and turbulence within the plume prevents us from using these visualizations alone to determine the plume shape, which is characterized during the independent first phase. However, submersible holography is essential for measuring the size distribution of submillimeter droplets within the opaque oil plume. We assume that most of the submillimeter droplets are formed when the oil is located well below the sample volume. Using available in-house codes, the holograms are processed to obtain in-focus images of the droplets in a series of parallel planes across the sample volume (figure 2.1e). The procedure includes subtraction of a time-averaged hologram to reduce background noise and numerical reconstruction at axial intervals of 0.2 mm (Sheng, Malkiel, and Katz, 2006; Talapatra et al., 2013). Compressing the 3-D field onto a 2-D plane is used for identifying low-intensity "subregions of interest" containing droplets. If needed, local instead of global thresholds are used for the segmentation to refine these regions. The 3-D positions and radii of all possible droplets are found using the Hough transform, based on a series of criteria involving edge gradients, outside-to-inside intensity ratio, and uniformity within the droplet. To detect small droplets (12 pixels), the analysis is performed after high-pass filtering the reconstructed field to minimize the effect of larger droplets. Gradient-based edge detection is used to determine the droplet depth. For the smallest droplets (<6 pixels diameter), the plane of focus is identified by edge detection, and the droplet size is estimated based on its in-focus image size. In presenting results, we include only droplets with

16

size of 4 pixels (16.2 μm) or higher.

2.2 The overall plume behavior

Figures 2.2(a–d) shows composite, instantaneous images of the crude oil, oil-dispersant, and oil analog plumes, with the two parts divided by a dashed line. The right part is taken from the same time series as the left part, but shows the right-most 358.2 mm portion of the image recorded 2.4 s later. The horizontal shift in displaying them corresponds to the distance traveled by the nozzle during this time. Joining these two images allows visualization of the plume over a larger spatial domain than would otherwise be possible. In all cases, the jet is injected vertically and is bent over by the crossflow, with the oil and oil-dispersant jets breaking up into droplets. The decrease in droplet sizes with increasing dispersant concentration is evident from the complete views and is highlighted in the insets. Millimeter scale droplets are present in crude and 1:100 DOR oil plumes (figures 2.2a and 2.2b), but not for the 1:25 DOR case (figure 2.2c). The increasing opacity with dispersant concentration is a global indicator of the presence of increasing concentration of fine droplets (e.g., figure 2.2c). Ignoring the wake structures under the plume momentarily, the bottom boundaries of the crude, 1:100 DOR, and analog plumes do not differ substantially, but are higher than that of the 1:25 DOR case (statistics follow). However, the upper boundaries differ substantially, with the plume height increasing with decreasing DOR (increasing droplet size). Large-scale billows are evident in all cases, but for the crude oil, the upper boundary is "diffused"

17
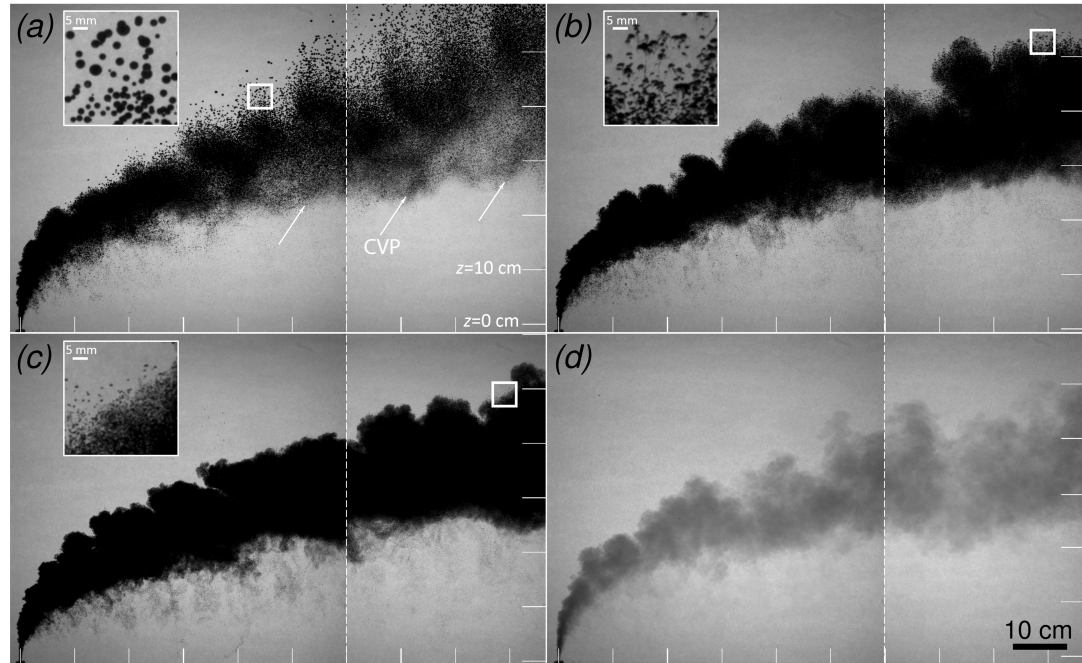
Figure 2.2: Sample composite images of jet/plumes injected at $u_j = 2.5$ m/s and towed at $U_c = 0.15$ m/s, of (a) crude oil, (b) 1:100 DOR oil, (c) 1:25 DOR oil, and (d) a dyed miscible fluid with matched density and viscosity. Dashed lines separate the image segments, with the horizontal shift matching the nozzle displacement. The insets above the plume show magnified sections corresponding to areas bounded by white squares. The white arrows indicate the location of the CVP core.

as large (3–5 mm) droplets escape from the plume, as is evident from their vertical trajectory, which is unaffected by plume turbulence. Consequently, the upper plume boundary appears to be inclined at a higher angle. A few escaping droplets appear at the upper boundary for the 1:100 DOR plume as well (inset in figure 2.2b). Many of these ~ 2 mm droplets in figure 2.2(b) are nonspherical, and have long threads trailing vertically behind, clearly illustrating the vertical droplet trajectory, which again, is affected very little by the plume turbulence. As discussed in Gopalan and Katz, 2010, these threads are associated with low interfacial tension and contribute to a substantial increase in the number of micron-scale droplets. The number and size (sub mm) of droplets that appear above the 1:25 DOR plume are much smaller, and the movies show that their motion is still dominated by the plume turbulence. These droplets do not have observable threads for two possible reasons, one being their complex trajectories and the other being the image resolution limits.

The high-speed videos also show that some of the droplets near the bottom boundary of the plume reside in largely horizontal vortices, which as visualization from the end view show, is the CVP. Although present for all cases, the CVP is particularly evident in the crude oil plume, where it appears as a region with increased concentration of small droplets, which is separated from the bulk of plume. Its location is marked by the white arrows in figure 2.2(a). As discussed later, the droplets appear to be trapped by this vortex structure and are transported in the positive x direction at a velocity that is higher than that of the bulk. Figure 2.2 also shows nearly vertical bands of fine droplets

19

trapped beneath all the oil plumes. They are easier to detect in the 1:100 DOR and 1:25 DOR cases, with more droplets present under the 1:25 DOR case. The movies reveal that these droplets are entrained from the plume edges by nearly vertical vortices extending downward from the bottom of the plume. These structures have been seen and analyzed in a series of jet in crossflow studies, e.g., Fric and Roshko, 1994 and Kelso, Lim, and Perry, 1996, and have been attributed to wake structures developing because of jet-induced blockage to the crossflow. As confirmed later, the amount of oil trapped beneath the plume seems to increase with decreasing interfacial tension and the resulting increase in concentration of fine droplets.

2.3 Evolution and dispersant effects of the droplet size distributions

Figures 2.3(a)–2.3(e) compares sample droplet-size distributions for the crude, 1:100 DOR, and 1:25 DOR plumes in the first Mini-Holocam position. These data are recorded as the plume bulk, in particular the space between CVP vortices, rises through the tank centerline. Each distribution represents an average over three realizations recorded during 1 s, and the samples are separated by 3.5 s. All the distributions appear to be multi-modal, with a primary distribution peak for small droplets, and another smaller peak for droplets of approximately 200 μm. Transiently bimodal distributions have been found in simulations applying the VDROP model for oil well blowouts (Zhao et al., 2014a) and breaking waves (Zhao et al., 2014b). Multimodal
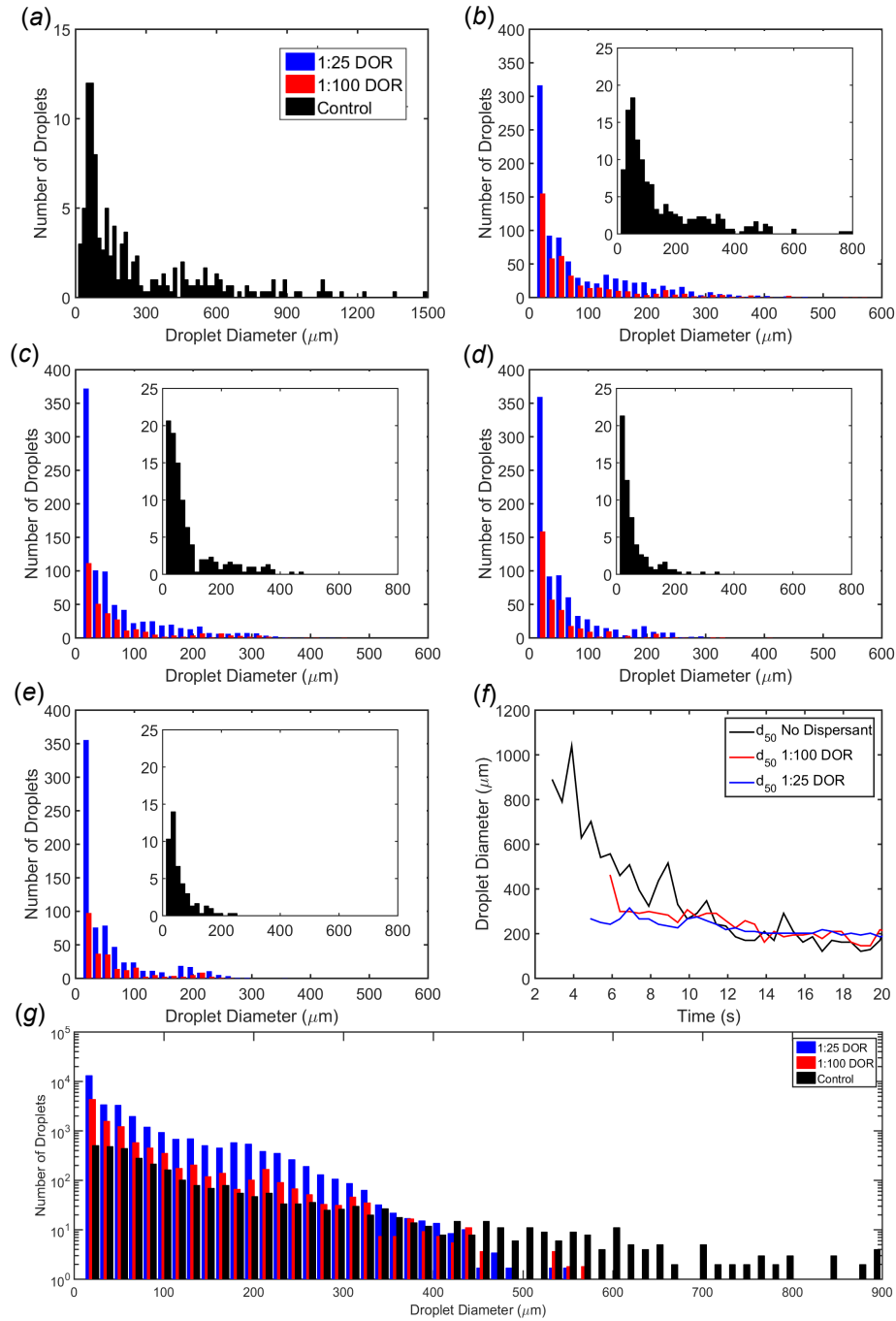
Figure 2.3: Droplet size distributions for the crude oil, 1:100 DOR, and 1:25 DOR plumes averaged over 1 s at centerline location at (a) $t = 3.4$ s (crude oil only), (b) 6.9 s, (c) 10.4 s, (d) 13.9 s, and (e) 17.4 s; (f) variations in d_{50} with time; (g) Combined droplet-size distributions at all time points. The insets represent the crude oil droplet-size distributions.

21

distributions have also been seen experimentally under breaking waves (Li et al., 2008). Temporal trends associated with the crude oil plume are considered first. Droplets appear in the sample volume at $t = 2.9$ s, so the results for $t = 3.4$ s (figure 2.3a) represent the earliest droplets reaching the holographic field of view. Conversely, droplets of the oil-dispersant plumes have not yet reached the sample volume, consistent with the plume shapes in figures 2.2. The crude oil droplets range in size from 16 mm to 1.5 mm, with the probability peak at approximately 50 mm. This set does not show larger droplets, the size of which, based on the high-speed movies, reaches about 5 mm. Both the scarcity of these large droplets, and the narrow gap between the Mini-Holocam tubes (6 mm), which may prevent the large droplets from penetrating, might affect this discrepancy. Crude oil distributions obtained at latter times are shown as insets in figures 2.3(b–e) due to the much lower droplet concentrations compared to those of the oil-dispersant cases. The number of droplets peaks at $t = 6.9$ s (figure 2.3b) as the center of the plume passes through the measurement volume, but the maximum droplet diameter (750 μm) is smaller than that obtained at earlier times, presumably due to diameter-based differences in rise velocity. At $t = 10.4$ s (figure 2.3c), the droplet number is already lower than its peak value, and the maximum droplet size decreases to 450 mm, as much of the plume already has passed through the sample volume. These trends of decreasing droplet count and maximum size continue for the last two measurements ($t = 13.9$ s in figure 2.3d and $t = 17.4$ s in figure 2.3e), and based on end view visualization, these droplets may originate from the wake vortices under the plumes.

The total number of droplets increases, but the fraction of large droplets and the size of the most abundant droplets decrease substantially with increasing dispersant concentration. For example, at $t = 6.9$ s (figure 2.3b), the distribution peaks are 50, 20, and 20 μm for the crude, 1:100 DOR, and 1:25 DOR cases, respectively. The size distributions at subsequent times (figures 2.3c–e) retain similar shapes, but the droplet concentrations decrease. However, the decrease rate is slower for the oil-dispersant cases, suggesting that the spatial distribution of droplets in them is more homogeneous. A consistent picture is provided in figure 2.3(f), which shows temporal variations in the volume median diameter d_{50} (Reid and Hobbs, 1998). For the crude oil, d_{50} begins at ~ 900 μm at $t = 3$ s and sharply declines over the next 5 s to approximately 350 μm. Subsequently, the decline is milder, decreasing to ~ 150 μm at $t = 20$ s. For the 1:100 DOR plume, d_{50} begins at 450 mm, declines sharply for 1 s, and declines slowly with values that are not significantly different from those of the crude oil case. For the 1:25 DOR plume, d_{50} declines slowly over time, after beginning at 250 μm, and after $t = 10$ s, does not differ from that of the 1:100 DOR case. The sharp decrease in d_{50} for the crude oil plume, and to a lesser extent for the 1:100 DOR case, reflects the effect of "droplet fractionation", as large droplets escape rapidly, leaving the smaller droplets, which are more susceptible to remaining trapped within the turbulent eddies. The fact that, after the initial period the values of d_{50} no longer depend significantly on the DOR, indicates that the characteristic sizes are more a function of, for example, turbulence level or CVP strength than the Weber number. However, one should keep in mind that the number of entrained droplets is vastly different. Figure 2.3(g) shows a combined histogram at all

23

times, i.e., the entire spectrum of droplets involved (though the abscissa is cut off at 900 μm). The droplet numbers are presented on a log scale to facilitate a comparison among the three cases. The crossover diameter, above which the number of crude oil droplets is larger than that of the DOR cases is about 400 μm. Although there is no such crossover between the DOR cases, the difference between them is striking below $\sim$ 300 mm, though not as evident for larger droplets. As shown in table 2.1, the values of d_{50} calculated from the bulk distributions for the crude, 1:100 DOR, and 1:25 DOR cases are 734, 275, and 234 μm, respectively. The corresponding values of d_{50} predicted by the modified We model of Brandvik et al., 2013; Brandvik et al., 2014 and Johansen, Brandvik, and Farooq, 2013, using their coefficients ($A = 24.6$, $B = 0.08$), are 1508, 368, and 233 mm. Hence, the measured and predicted values agree for the 1:25 DOR case, but not for the others. This discrepancy might be affected by the previously discussed effect of the narrow gap between the Mini-Holocam windows. Finally, figure 2.4 shows variations with time of the droplet-size distributions for position two (figure 2.1d), i.e., within the crude oil CVP. Again, each distribution is an average of three measurements performed within 1 s. The first time that droplets appear in this sampling region is after about 6.9 s. By this time, there are very few large droplets within the CVP, indicating that most have escaped before; in other words, the CVP flow field is not powerful enough to retain droplets larger than about 200 μm.
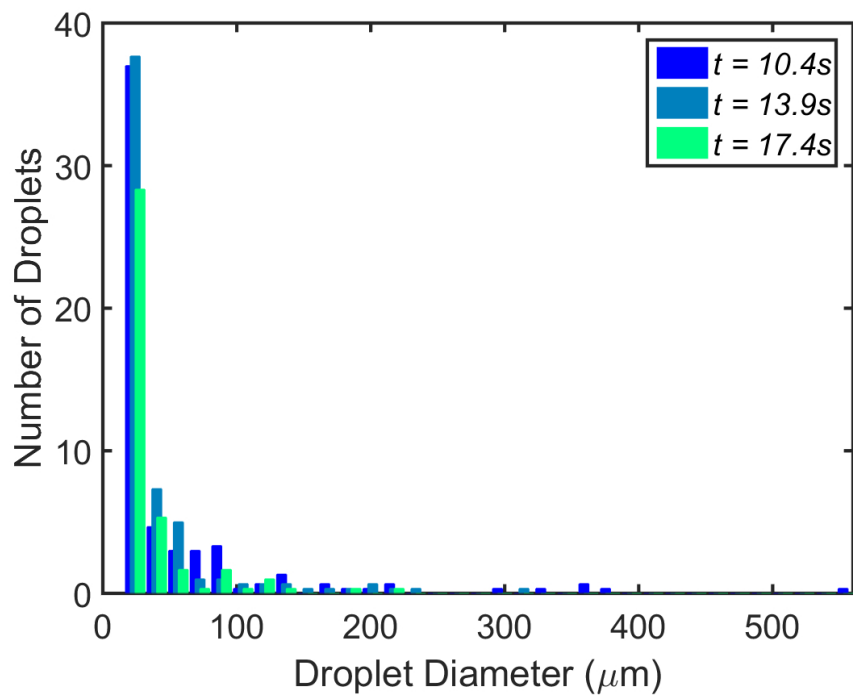
Figure 2.4: Droplet-size distributions for the crude oil plume averaged over 1 s in CVP core location (second position in figure 2.1d) at $t = 10.4, 13.9$, and 17.4 s.

2.4 Summary

This chapter investigate the behavior of an oil jet transitioning into a plume in a crossflow at high velocity ratios. High-speed imaging and *in situ* digital inline holography are applied to observe the global structure of the flow and measure the size distribution of crude oil droplets. The experiments are performed using crude oil as well as oil premixed with dispersants at DOR of 1:100 and 1:25. A dyed miscible liquid with the same density and viscosity as the crude is also examined as a reference.

As expected, the dispersants dramatically reduce the droplet sizes, consistent with many previous studies involving other types of shear flows (Li et al., 2008; Johansen, Brandvik, and Farooq, 2013), and accordingly, increase the number of droplets. The size of droplets retained by the plume decreases in time. For the crude and 1:100 DOR cases, the initial decreases are sharp, but different, and then change to a mild rate that converges with that of the 1:25 DOR case. Detailed statistics for several plumes are provided. The dispersant concentration and corresponding droplet sizes cause substantial changes to the overall structure of the plume. In particular (i) the upper boundary of the plume rises at a sharper angle with decreasing dispersant concentration; and (ii) the number of droplets entrained by large vortical structures (CVP) under the plume increases with dispersant concentration.

Given the importance of the droplet size distribution on the subsequent oil dispersion, it is of practical interest to understand how the droplets form in the near field. Therefore, the next chapter will elucidate the fragmentation and droplet formation process of a vertical buoyant jet with surrogate liquid

pairs, while matching the non-dimensional parameters to those of the crude

oil jet injected into seawater.

Chapter 3

Fragmentation and the formation of compound droplets

This chapter will discuss the droplet formation with a focus on the formation and quantitative analysis of compound droplets, which contains one or multiple layered water droplets. The high speed Planar Laser Induced Fluorescence (PLIF) experimental setup and the Machine Learning processing techniques will be discussed in section 3.1. Several phenomena related to compound droplets generation will be demonstrated in section 3.2, followed by an analysis showing the fraction of the compound droplets, their impact on the oil-water interfacial area, and the striking differences between the odd exterior shapes of the oil droplets and the nearly spherical interior water droplets. The implication of such characteristics of the compound droplet will be discussed and summarized in section 3.3.

3.1 Experimental techniques

3.1.1 Laser-induced fluorescence

Aimed at studying phenomena associated with mixing of light crude oil with seawater, but using refractive index-matched fluids, we have selected silicone oil (polydimethylsiloxane, trimethylsiloxy terminated) as the dispersed phase and sugar water (64% by weight) as the continuous phase. Their density, viscosity, interfacial tension and those for oil-water systems are presented in table 3.1.The viscosity is determined by a capillary viscometer, the interfacial tension by a pendant drop method, and the refractive indices (1.4022) by a refractometer. The crude oil is originated from the Marlin platform located 60 km northeast of the Deepwater Horizon platform and provided by BP. Both the crude oil and seawater properties have been measured in the lab by Murphy et al., 2016. As illustrated in figure 3.1, the experiments have been conducted in a $39 \times 24.1 \times 76.2$ cm^3 acrylic tank partially filled with sugar water. The silicone oil is injected from a regulated, nitrogen-pressurized reservoir, and then passes through a flowmeter (Omega, FL-6110A), a settling chamber containing honeycomb and screens, as well as a nozzle with 6.35:1 diameter ratio. The exit diameter of the initially laminar jet is 10 mm. Three sets of experiments have been conducted at $u_o = 1.5$, 3.4 and 5.3 m/s, corresponding to Reynolds numbers of 594, 1358 and 2122, and Weber numbers of 785, 4100 and 10000, respectively. The Ohnesorge number is $Oh = 0.047$ for all cases. Based on Masutani and Adams, 2001, all three cases fall in the so-called atomization regime, where droplets of a wide size range are generated close
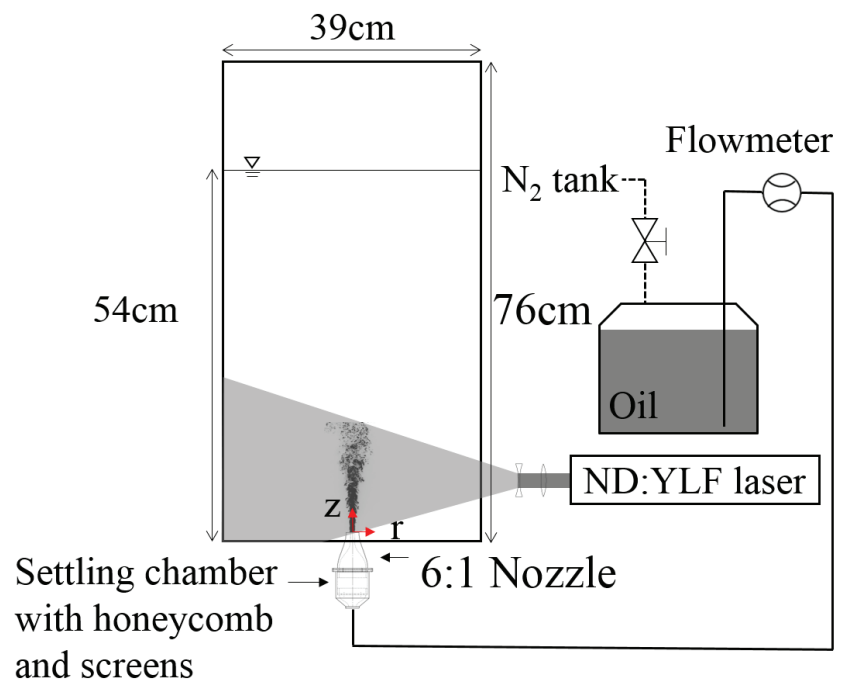
Figure 3.1: Experimental setup for observing the index-matched buoyant oil jet superimposed on a sample PLIF image.

	$\rho \ (kg/m^3)$	$\mu \ (kg/m \cdot s)$	$\sigma \ (N/m)$
Silicone oil (SI)	960	$(2.40 \pm 0.2) \times 10^{-2}$	$(27 \pm 0.5) \times 10^{-3}$
Sugar water (SW)	1155	$(5.65 \pm 0.2) \times 10^{-3}$	
Light crude oil (CR)	864	$(8.81 \pm 0.04) \times 10^{-3}$	$(19 \pm 0.1) \times 10^{-3}$
Seawater (SE)	1018	$(1.07 \pm 0.02) \times 10^{-3}$	
Ratio of SI to SW	0.83	4.25	
Ratio of CR to SE	0.85	8.24	

Table 3.1: Physical properties of surrogate fluid pair associated the present experiments

to the jet exit. The viscosity ratio and interfacial tension of the present fluids differ by less than 2:1 from those of the crude oil-seawater pair. They have been selected because they allow us to cover a 4:1 range in Reynolds numbers while maintaining speeds that are low enough that the near field of the jet is not contaminated by oil droplets entrained by the circulating external flow.

The center plane of the jet is illuminated with a 1mm thick sheet of pulsed 527 nm Nd:YLF laser, which is synchronized with a high-speed camera (PCO.dimax). The silicone oil is visualized using Nile Red, which is insoluble in water, and has an emission wavelength of 635-650 nm. Because Nile Red is also insoluble in silicone oil, it is mixed with 1.25% by volume mineral oil, which serves as a soluble carrier, and the properties in table 1 correspond to the oil mixture. A long-pass filter with a cutoff wavelength of 550 nm is placed in front of the camera to remove the green light from the recorded images. The 2016×2016 pixel^2 images have been recorded at two magnifications: large fields of view (FOV) of 208.5×208.5 mm^2 have been recorded at 500 frames per second (fps) for Re=594 and 1358, and at 1000fps for $Re = 2122$. High magnification images with a view of 12.9×12.9 mm^2 (6.4μm/px) have been

recorded at 1000 fps in regions centered at z/d=10.6, 20.6 and 30.6.

3.1.2 Random forest based droplet morphology analysis

To measure the statistics of droplet size distributions and shapes, specialized data processing procedures have been developed. The compound droplets are identified and measured by machine learning based image processing techniques. The scheme consists of image enhancement, classification of oil and water, identification of compound droplet, as well as measurements of their size and perimeter. As illustrated in figure 3.2(a), the original PLIF images have stripes due to refraction of light from the top and bottom of droplets owing to a slight mismatch ($<$0.0005) in refractive indices. Therefore, a combined wavelet-Fourier filtering (Münch et al., 2009) has been applied to alleviate these stripes, resulting in the sample shown in figure 3.2(b). Briefly, Daubechies wavelets (DB25) are used as basis functions for 2D multi-resolution (5 levels) wavelet decomposition. Then, a 2D Fourier transform is applied on the horizontal detail coefficients to identify the spectral range containing the signature of the stripes. A Gaussian band-pass filter with a damping factor of 5 is then applied in the Fourier space to suppress the stripes. When the resulting images are reconstructed, dynamic masks maintain the filtered image within the bright oil signature but preserve the original background in dark area. Owing to the complexity of the PLIF images, global single-value or adaptive local threshold segmentation techniques are inadequate for correctly separating the oil from the water. Consequently, a machine learning-based pixel-wise classification has been implemented, following
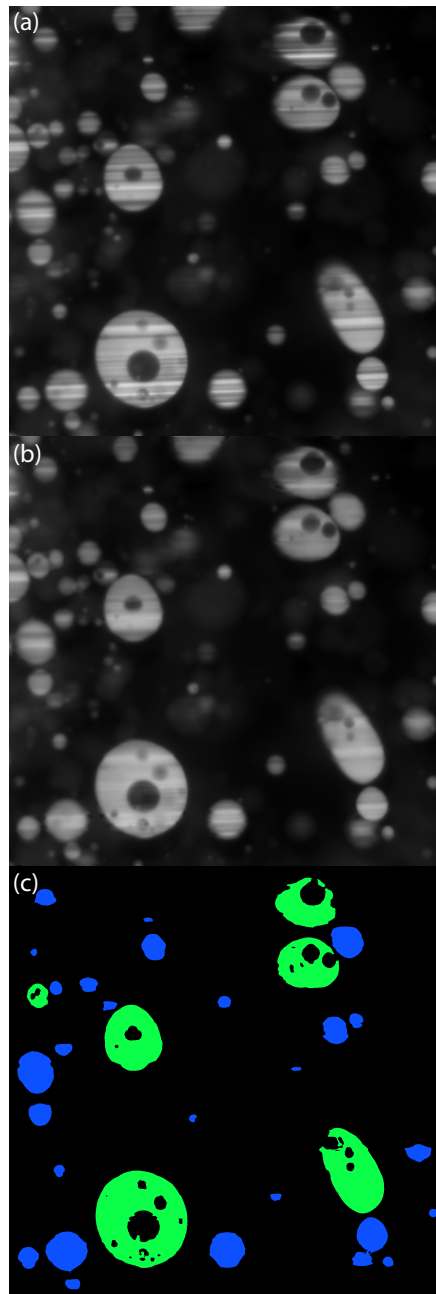
Figure 3.2: A sample demonstrating the removal of stripe from images, and machine learning-based segmentation: (a) Original image; (b) the same image after stripe removal; and (c) thresholded images with green indicating compound droplets.

Arganda-Carreras et al., 2017. The training features include the original intensity, its mean and variance, the Gaussian-blurred and Sobel-filtered intensity, as well as the trace, first, and second eigenvalues of the Hessian matrix at each pixel. Except for the original intensity, all the training features are performed for five kernel sizes: $\kappa = 1, 2, 4, 8$ and 16. The choice of training features takes noise reduction, edge detection and texture description features of varying neighboring scales for each pixel into consideration. The random forest, which consists of 200 decision trees and two features per node, is trained based on labeled training sets. The resulting probability maps of classified pixels are then segmented by the Otsu's method. Distance watershed transformation is subsequently performed to separate overlapping droplets, blob analysis is used to determine the droplet statistics. Ligaments and droplets cut by the border of images are not accounted for in any of the number density or fraction statistics. Sample results are shown in figure 3.2(c), with color gray indicating compound droplets. The sample volume depth and associated threshold limits and uncertainty are estimated by traversing a 500 μm pendant droplet through the laser sheet and using the same trained classifier to gauge the detection boundaries (1 ± 0.1 mm). Following Wu et al., 2013, the misclassification error rate in pixel is estimated as 8.7%. The relative combined uncertainty in number density, 10% and in diameter, 4.5%, is indicated for a couple of data points in figure 3.9(a) and 3.10.
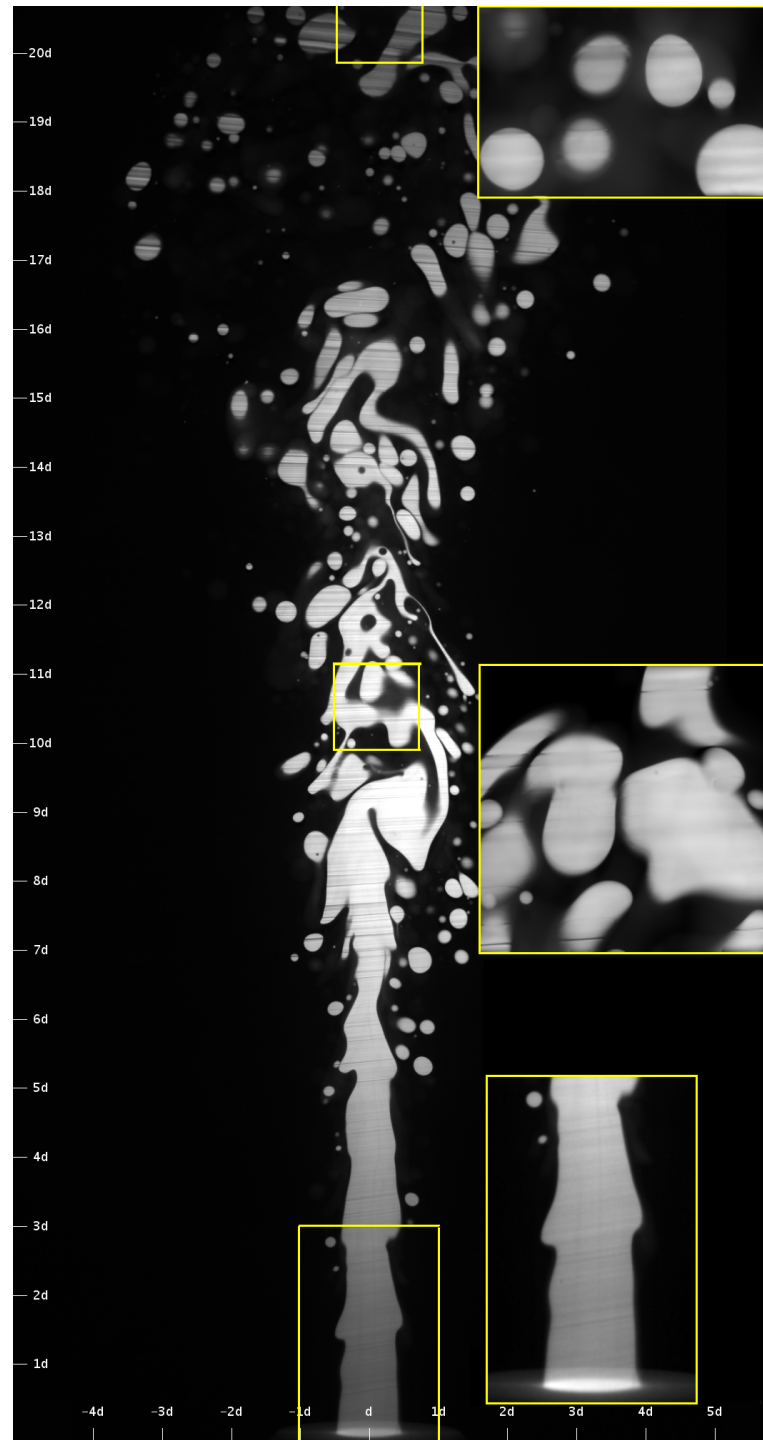
Figure 3.3: Sample images of the oil jet fragmentation at $Re = 594$, $We = 785$. Bottom inserts are enlarged 30×20 mm^2 sections of the areas marked by yellow boxes; middle and top inserts are enlarged 12.9×12.9 mm^2 sections of the marked areas recorded at a different time and at a higher magnification.
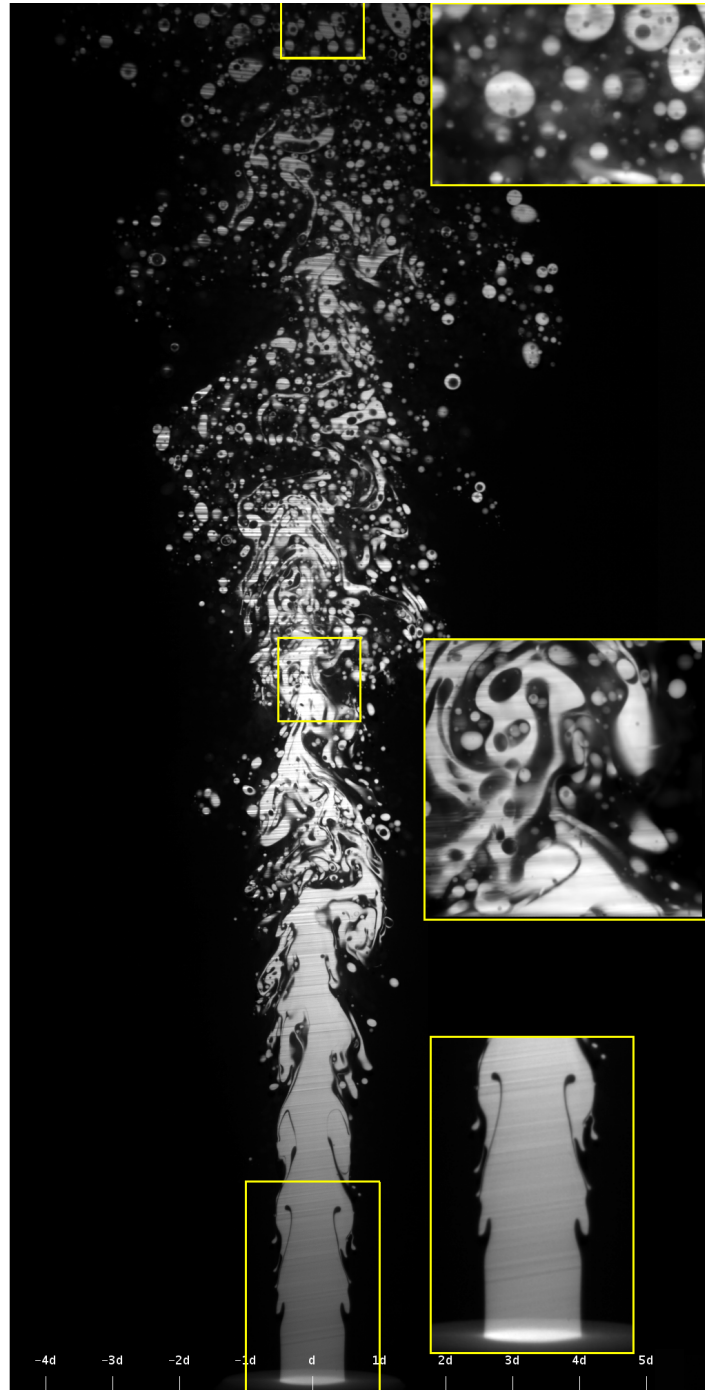
Figure 3.4: Sample images of the oil jet fragmentation at $Re = 1358$, $We = 4100$. Bottom inserts are enlarged 30×20 mm^2 sections of the areas marked by yellow boxes; middle and top inserts are enlarged 12.9×12.9 mm^2 sections of the marked areas recorded at a different time and at a higher magnification.
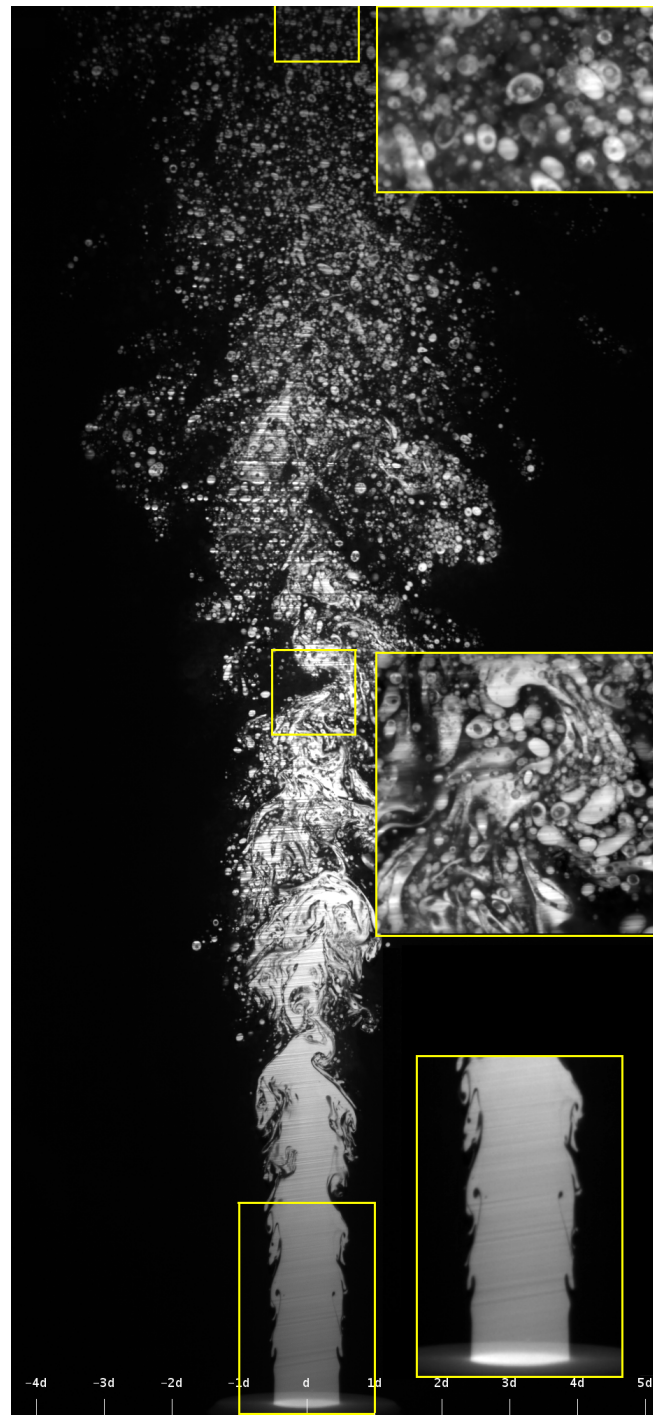
Figure 3.5: Sample images of the oil jet fragmentation at $Re = 2122$, $We = 10000$. Bottom inserts are enlarged 30×20 mm^2 sections of the areas marked by yellow boxes; middle and top inserts are enlarged 12.9×12.9 mm^2 sections of the marked areas recorded at a different time and at a higher magnification.
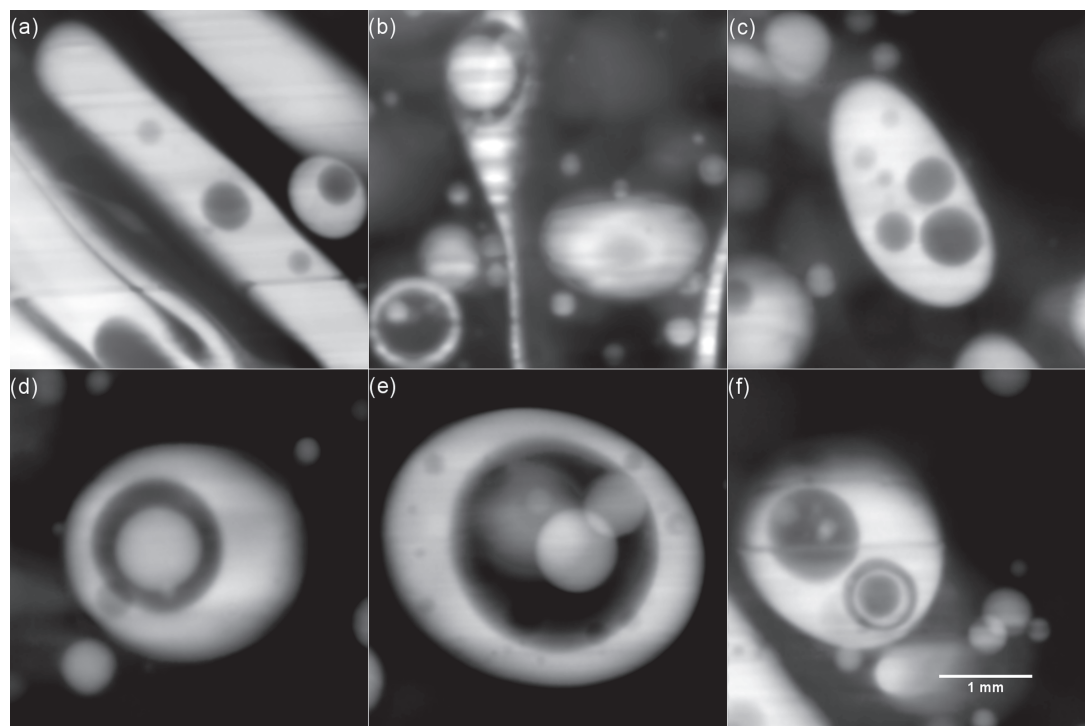
Figure 3.6: Samples of compound oil ligaments and droplets at $Re = 1358$ and $z/d = 20.6$.

3.2 Results

Setting the framework for the present observations, sample large FOV images illustrating the jet fragmentation process are presented in figures 3.3, 3.4, and 3.5, with the nozzle exit visible at the bottom. The (originally square) images have been cropped to 208.5×100 mm^2 but are presented undistorted with scales expressed in nozzle diameters provided along the left and bottom edges of the figure. Corresponding movie (movie 1) is provided as supplementary material in Xue and Katz, 2019. Inserts showing magnified images of the regions are also presented. Focusing initially on the two higher Reynolds number cases (figures 3.4 and 3.5, the streamwise evolution of the jet consists of three regions, namely Kevin-Helmholtz (K-H) roll-up at low z/d, ligament dominated region at mid range, and dispersed droplet region at high z/d. The initial roll-up and the end of the nearly axisymmetric K-H region occur closer to the nozzle with increasing Re. During roll-up, the jet entrains thin layers of water. In parallel, stretching of the upstream tail of one ring by flow induced by the one following it generates thin oil ligaments, which break up into a limited number of oil droplets. These droplets are subsequently entrained back into the jet. Further downstream, i.e. around $z/d > 4.5$ and 3 for $Re = 1358$ and 2122, respectively, the axisymmetry is lost, similar to miscible jets (Liepmann and Gharib, 1992). Here, the jet structure transitions into elongated ligaments of varying shapes that wrap around each other, some breaking into droplets. At about $7 < z/d < 13$ and $6 < z/d < 12$ for $Re = 1358$ and 2122, respectively, the width of these ligaments decreases, and they break up into droplets (quantitative data follows). While a few ligaments persist up

to $z/d = 20$ at $Re = 1358$, they mostly disappear at $Re = 2122$. As for the $Re = 594$ jet (figure 3.3), thick ligaments still form and then break up into large blobs, but later than the other cases. However, the jet is not axisymmetric even at the exit from the nozzle and tends to meander downstream. There are two possible contributors to this phenomenon. First, it appears that some water penetrates into the periphery of the nozzle. For this case, the densimetric Froude number, defined as $Fr = u_o / \sqrt{gd(\rho_w - \rho_o)/(\rho_w + \rho_o)}$, is 15.6, and $Re_t = Re/Fr$ is 38. Based on studies of displacement flows in vertical pipes by Amiri, Larachi, and Taghavi, 2016 and Hasnain, Segura, and Alba, 2017, under these conditions an interface between the exterior and interior fluids exist inside the pipe, consistent with the present observations. In contrast, for the present higher Reynolds numbers, the oil is expected to displace the water. Second, meandering of jets has been observed at $Re < 1000$, even without buoyancy effects (Crow and Champagne, 1971).

Focusing on $Re = 1358$ and 2122, many of the oil ligaments in the middle inserts, and the droplets in the upper inserts contain water pockets. In contrast, they rarely appear at $Re = 594$. Higher magnification samples of such compound droplets/ligaments containing one or more water droplets are presented in figure 3.6 (and movie 2). In some cases, the internal water droplets contain smaller oil droplets and so on, creating a "Russian Doll" like phenomenon. Note that while the external interfaces have odd shapes, the internal ones are largely spherical, as will be quantified later. A typical process leading to the formation of compound ligaments is demonstrated in figure 3.7 and corresponding movie 3. Starting from the K-H roll-up, the red solid

40

z/d	Re	ΣN	ΣN_c	$\Sigma N_c/\Sigma N$	$D_{32}\ (\mu m)$ (all droplets)	$d_{50}\ (\mu m)$ (all droplets)
20.6	594	815	8	1%	3.4×10^3	3.8×10^3
	1358	7853	1333	17%	2.0×10^3	2.3×10^3
	2122	25527	2563	10%	1.1×10^3	1.1×10^3
30.6	594	675	1	0.2%	3.0×10^3	3.6×10^3
	1358	4309	867	20%	1.8×10^3	2.1×10^3
	2122	15031	1727	11%	0.9×10^3	0.9×10^3

Table 3.2: Numbers and statistics of detected droplets

arrow tracks the same water film, which appears as a thin ligament in the planar view. At $z/d < 3.5$, the film is elongated by the local shear, and at $4 < z/d < 9.5$, it separates from the bulk water, breaking up into multiple water droplets at $z/d \sim 10$. The entrainment point, as well as the time history of stretching and breakup vary, as the orange dashed arrows indicate, but the process repeats itself. Samples of subsequent stretching and fragmentation of an oil ligament containing water pockets by a large eddy is presented figure 3.8 (and movie 4). As is evident, the compound droplets and ligaments are ubiquitous by $z/d > 11$.

Statistical information derived from the procedures described in the experimental techniques 3.1 is provided in figures 3.9-3.13 and table 3.2. Figures 3.9(a) is the number density of *all* the oil droplets, $dN/d(D_a)$, at $20 < z/d < 21.3$, plotted vs. their apparent diameter, D_a, which is calculated based on their total cross section area, A, including the pockets. Each plot is based on analyzing 209 instantaneous realizations, with error bar representing the uncertainty in the number density and diameter. The total number of droplets, ΣN, is listed in table 3.2. For all cases, the slopes of $dN/d(D_a)$ is mild: -0.5

and -1 for $Re = 594, 1358$ respectively and nearly flat for Re=2122. However, for large droplets, the slope steepens to about -4.5. The increasing steepness in slope of the droplet size distribution represents an increasing contribution of number density by the small droplets. The peak in volumetric contribution at the point where the slope changes from more to less than -3, which is indicated by bold points in figure 3.9(a), decreases with increasing Re. Figure 3.9(b) shows the cumulative distribution of volume fraction, V_{cum}/V, plotted vs. droplet size normalized by the Sauter mean diameter, D_{32}, defined as

$$D_{32} = (\int_0^\infty D_a^3 N'(D_a)dD_a)/(\int_0^\infty D_a^2 N'(D_a)dD_a) \qquad (3.1)$$

where $N' = dN/d(D_a)$ (Brennen, 2005). The values of D_{32} is provided in table 3.2. In agreement with Simmons, 1977, the curves nearly collapse for $V_{cum}/V <\sim 0.8$, but fluctuate at higher values, presumably owing to the small number of large droplets in the present dataset. Figure 3.9(c) compares the values of D_{32}/d plotted vs. We to the data points and empirical fit by of Wu, Miranda, and Faeth, 1995 measured for liquid jets in air, $D_{32}/d = 32We^{-3/5}$. As is evident, the present results for $Re = 1358$ and 2122 agree with the line fit, but is lower than extrapolation of the line fit for $Re = 594$. Figure 3.9(d) compares the present volume median diameter, d_{50} (table 3.2), defined as the diameter where the cumulative volume fraction reaches 50%, to a semi-empirical model introduced by Johansen, Brandvik, and Farooq, 2013. The semi-empirical fit is $d_{50}/d = A(We^*)^{-3/5}$, where $We^* = We^{-3/5}/[1 + BCa(d_{50}/d)^{1/3}]$ is a modified Weber Number, $Ca = \mu_d u_d/\sigma$ is the capillary number, and A and B are empirical constants. In a later report by the same group (Brandvik

et al., 2014), they report A=24.6 and B=0.08. The data points and line fit are reproduced from that later report. All the present cases, including those of $Re = 594$ agree with this model. Before concluding, figure 3.9(b) also shows a least-squared lognormal fit to the cumulative volume distributions based on all three datasets. The results show a reasonable agreement for a mean and standard deviation of $ln(D_a/D_{32})$ being 0.13 and 0.57, respectively. A similar agreement could be obtained for D_a/d_{50}, but with mean and standard deviation of $ln(D_a/d_{50})$ being 0.0 and 0.57, respectively. Fitting a Rosin-Rammler distribution instead (not shown), gives a spread coefficient of 2.2 vs. 2.0 in Brandvik et al., 2014.

The ratio of the number of compound droplets, N_c, to the total number, N, for each size bin is presented in figure 3.10(a), including only points with more than 60 droplets. Very few compound droplets exist at $Re = 594$. In contrast, there is a small difference between the results for the other two cases, i.e. the fraction of compound droplets depends mostly on the diameter. For $D_a/d > 0.07$, the slope of these curves is about two, possibly suggesting that the fraction increase with the droplet surface area. This rapid increase implies that while only 30% and 38% of the 1mm droplets are compound for $Re = 1358$ and 2122, respectively, this fraction increases to 71% and 84% for 2mm droplets. The size distributions of compound droplets, which is presented in figure 3.10(b), have peaks that shift to a lower diameter with increasing Re. Existence of this peak and shift are results of the combined effects of the distributions of both N_c/N and $dN/d(D_a)$. The peaks are caused by the opposite trends of N_c/N and $dN/d(D_a)$ with diameter. The shift is

caused by the decrease in the concentration of large droplets, which are more likely to be compound, with increasing Re. Before proceeding, note that trends of $\sum N_c / \sum N$ depicted in table 3.2 might appear contradictory to those displayed in figure 3.10(a). Specifically, the table shows that the total number of compound droplets, $\sum N_c$, increases with Re, but their fraction ($\sum N_c / \sum N$) decreases from 17% at $Re = 1358$, to 10% at $Re = 2122$. Figure 3.10(a) shows that the size-dependent fraction corresponding to large droplets increases slightly with Re, and that of small droplets decreases with increasing Re. Since the total number of small droplets is orders of magnitude higher than the large ones, the small droplets dominate the statistics in table 3.2 even when the corresponding values of N_c / N are low.

The inner water droplets increase the oil-water interfacial area. Figure 3.11 shows the joint probability distribution (PDF) of D_a / d and the fractional increase in interfacial area, $\Delta S / S$, for $Re = 1358$ and 2122 at $z/d = 20.6$ and 30.6. The interfacial area is calculated from the perimeter, P, of droplets assuming spherical symmetry. The dashed line shows the limit below which the internal droplet perimeter cannot be measured with reasonable certainty. Several trends are evident. First, the distributions, including the upper limit, broaden with increasing diameter. Second, the areas covered by the joint PDF decrease, and the peak probabilities increase with increasing Re. This trend is consistent with the decrease in concentration of large droplets with increasing Re (figure 3.10b). Third, the most probable values and upper bounds of the PDFs tend to shift upward with increasing z/d. As a plausible explanation for this trend, note that between $z/d = 20.6$ and 30.6, both D_{32} and d_{50} of all

44

the droplets (table 3.2) decrease, representing the effect of reduction in the fraction of large droplets, presumably by the shear-induced breakup. During this process, the interior droplets are less likely to breakup, as suggested by their nearly spherical shape, i.e. they maintain their size. Consequently, $\Delta S/S$ should be expected to increase. For example, the mean values of $\Delta S/S$ at $z/d = 20.6$, 15% and 8% for $Re = 1358$ and 2122, respectively, increases to 23% and 15% at z/d=30.6. Note that, the values of $\Delta S/S$ are plotted in a log scale, whereas the PDF magnitude is presented on a linear scale. The large tail with values of $\Delta S/S$ well above 0.1 results in a mean value significantly higher than the most probable one. While it is difficult to infer the trend with Re from the PDF owing to the broad distributions at $Re = 1358$, the data shows that the mean $\Delta S/S$ decreases with increasing Re. This trend implies that the decrease in size of inner droplets outweighs the decrease in outer size with increasing Re. It might be associated with differences in the size of water ligament during the early K-H roll-up phase, as suggested by figures 3.3, 3.4, and 3.5. A similar analysis has been performed for the volume fraction of water in the oil droplets (figure 3.12). Quantitatively, the trends are similar to those of $\Delta S/S$, but values differ. At $z/d = 20.6$, the mean volume fraction is 3% and 2% at $Re = 1358$ and 2122, respectively. On average, the compound droplets have small effects ($\sim 3\%$), on their buoyancy.

While the oil droplets have odd exterior shapes owing to the influence of turbulence, the interior droplets appear more circular. To compare the degree of deformation, we define a surrogate asphericity, $\Phi = (P/\pi)/\sqrt{4A/\pi}$, i.e. the ratio between the droplet diameter calculated from the perimeter and that

calculated from the area. The magnitude of Φ ranges from one for a sphere to higher values as the shape complexity increases. The trends for the outer shapes at $Re = 1358$ are presented in figure 3.13(a), and those for the inner droplets, in figure 3.13(b). They are plotted vs. the corresponding capillary numbers, $Ca_o = \mu_w u_o D_a / d\sigma$ for the outside surface, and $Ca_i = \mu_o u_o D_i / d\sigma$, where D_i is the diameter for the inner droplet. Sample corresponding images are shown in figure 3.13(c-e). For the outer droplets, the Φ scatters between 1 and 3.5, with the upper bound increasing with Ca_o. Hence, the average asphericity for each capillary number, $\overline{\Phi(Ca_o)}$, also increases with droplet size. In contrast, figure 3.13(b) shows that the inner droplets deviate only slightly from a spherical shape, irrespective of the Ca_i or the shape of the outer droplets, indicating that the inner droplets are only weakly influenced by the external shear. As discussed below, these observations are consistent with analyses of isolated compound droplet subjected to shear.

3.3 Discussions and Summary

Refractive index matching and PLIF are used to study the fragmentation process of buoyant oil jets in water. Although it rarely happens at $Re = 594$ ($We = 785$), compound droplets form regularly at $Re = 1358$ and $Re = 2122$ and persist at least up to $z/d = 30.6$. The origin of some of the water pockets can be traced back to engulfment of water ligaments during roll-up of the K-H vortices near the exit from the jet. In contrast, long thin water ligaments rarely form at $Re = 594$ before the oil breaks up, suggesting that for the

present $Oh = 0.047$, the near field shear is not strong enough to generate such ligaments. In other words, when the characteristic time scale of the jet, d/u_d, is compared to that derived from viscosity and interfacial tension, $\mu_d d/\sigma$, their ratio, i.e. Ca, might have to exceed a minimum value for the formation of elongated ligaments. In the present study, compound droplets are not generated for $Ca = 1.3$ and are abundant for $Ca \geqslant 3.0$.

For the present range, the fraction of compound droplets does not vary significantly with Re, but increases rapidly with droplet diameter, exceeding 78% for droplets larger than 2mm. Since small droplets are less likely to be compound, and the concentration of large droplets diminishes as the Re increases, the size distributions of compound droplets have peaks that increase in magnitude but shift to a lower diameter with increasing Re. Although the internal water pockets reduce the buoyancy by only a few percent, they increase the oil-water interfacial area by about 15%. While the increased surface area could presumably enhance the dissolution rate of soluble components of oil into the water, e.g. during crude oil spills, one cannot simply assume a linear relationship between the enlarged interfacial area and mass diffusion. Two potential effects should be considered: First, owing to the quiescent internal interfaces, the mass diffusion from the oil to the water is not likely to be affected by turbulence, in contrast to the external flow. Therefore, the internal mass diffusion is likely to be slower than that occurring along the outer surfaces. Second, because the soluble oil compounds in the internal water cannot be diluted by mixing with the surrounding water, their concentration is expected to increase over time, further reducing the dissolution rate.

As expected, the oil droplets are deformed in the near field of the jet, becoming increasing more aspherical with increasing diameter (Ca). In contrast, the interior droplets remain nearly spherical irrespective of their sizes, suggesting that they are exposed to a more quiescent environment. There is considerable literature about the behavior of isolated compound droplets subjected to external shear. Reduced deformation of the internal droplet with increasing μ_o/μ_w has been shown for Ca of the same range by Stone and Leal, 1990, Mandal, Ghosh, and Chakraborty, 2016 and Kim and Dabiri, 2017. In contrast, substantial deformations are reported for higher Ca and low interfacial tension of the interior droplet by Smith, Ottino, and Cruz, 2004. Presumably, the small size of the interior droplet and dampening of the external shear by the higher oil viscosity create an environment with low local capillary numbers. It would be of interest to determine whether such a quiescent micro-environment in the middle of high shear zones affects the subsequent interactions of crude oil with the biochemical environment in the ocean during the long bio-degradation process of the oil.
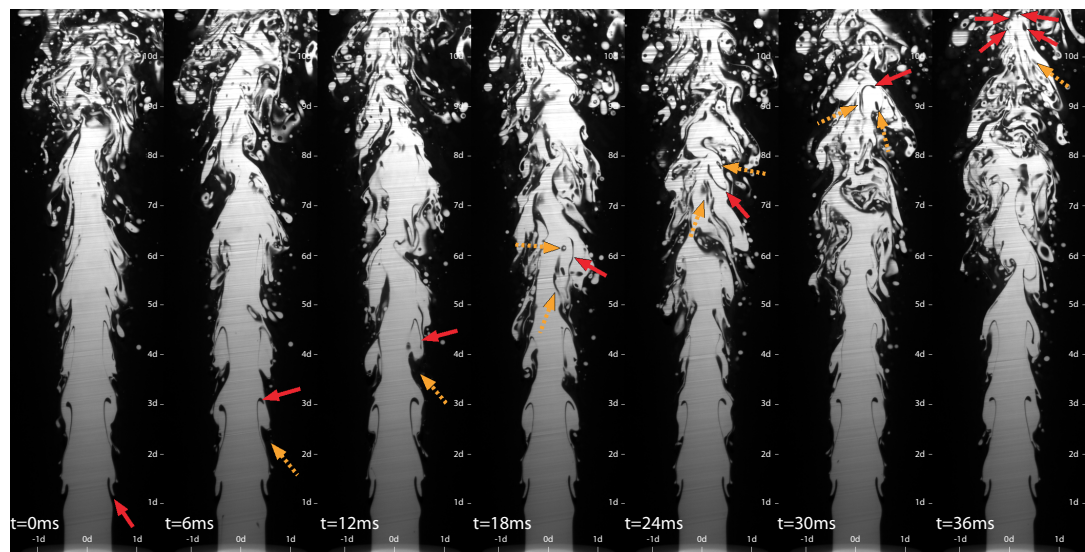
Figure 3.7: A time sequence showing processes leading to compound droplet formation at $Re = 1358$. Arrows of the same color and shape follow the same water ligament in frames separated by 6 ms.
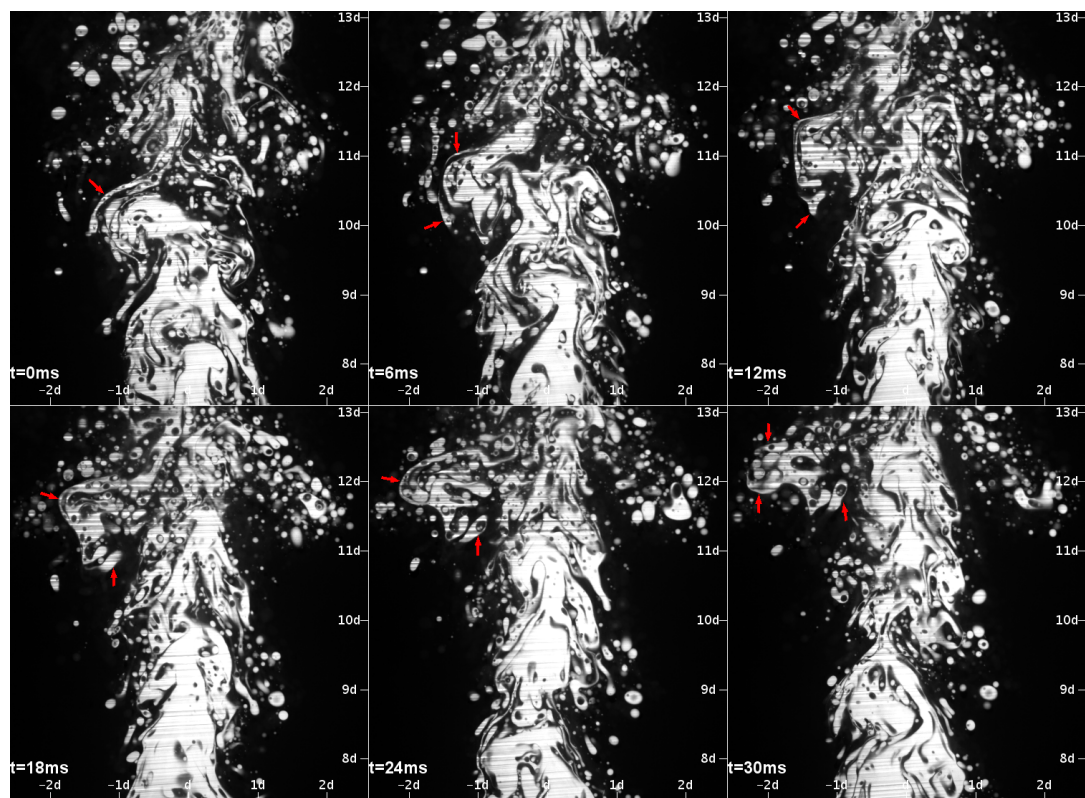
Figure 3.8: Evolution of ligaments resulting in compound droplet formation at $Re = 1358$. The arrows follow the same ligament in frames separated by 6 ms.
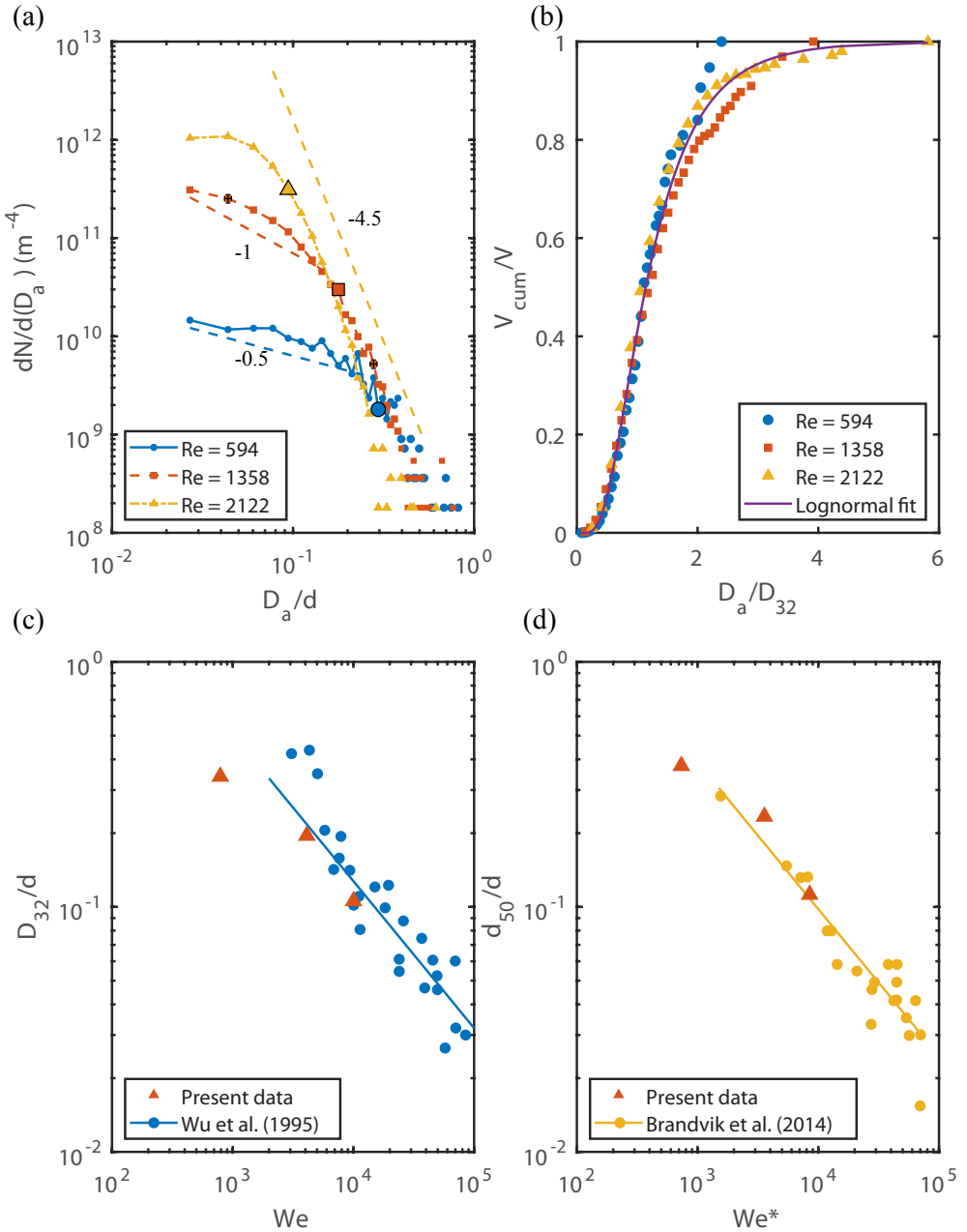
Figure 3.9: Time averaged (a) number density distribution of all oil droplets, bold points represent the peak volumetric contribution, (b) the cumulative distribution of volume fraction vs. droplet size normalized by Sauter mean diameter with a lognormal fit based on all three dataset, (c) Sauter mean diameter vs. Weber number superimposed on previous data points and line fits reproduced from Wu, Miranda, and Faeth, 1995 and (d) volumetric median diameter vs. modified Weber number superimposed on previous data points and line fits with A=24.6 and B=0.08 reproduced from Brandvik et al., 2014.

51
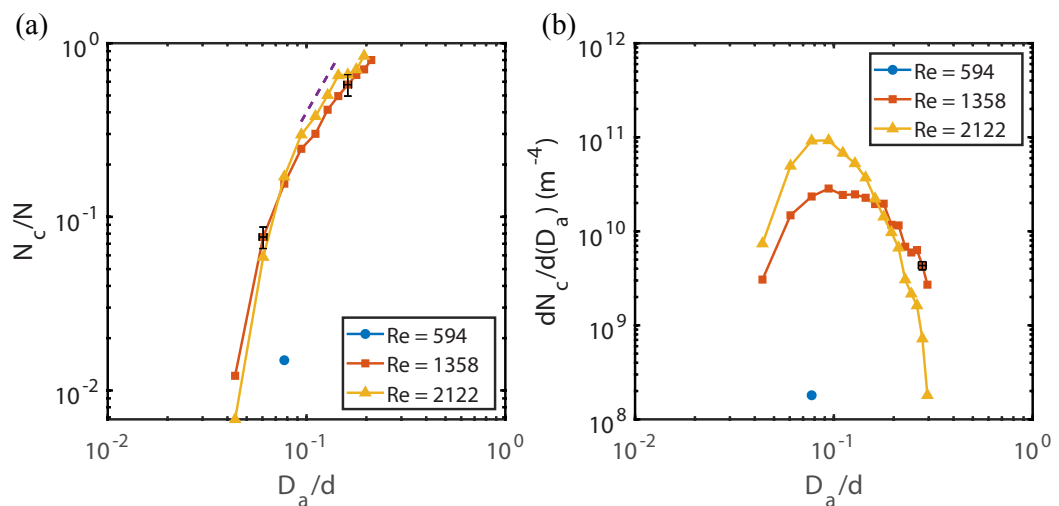
Figure 3.10: Time averaged (a) fraction of compound droplets and (b) the number density distribution of compound droplets at $z/d = 20.6$.
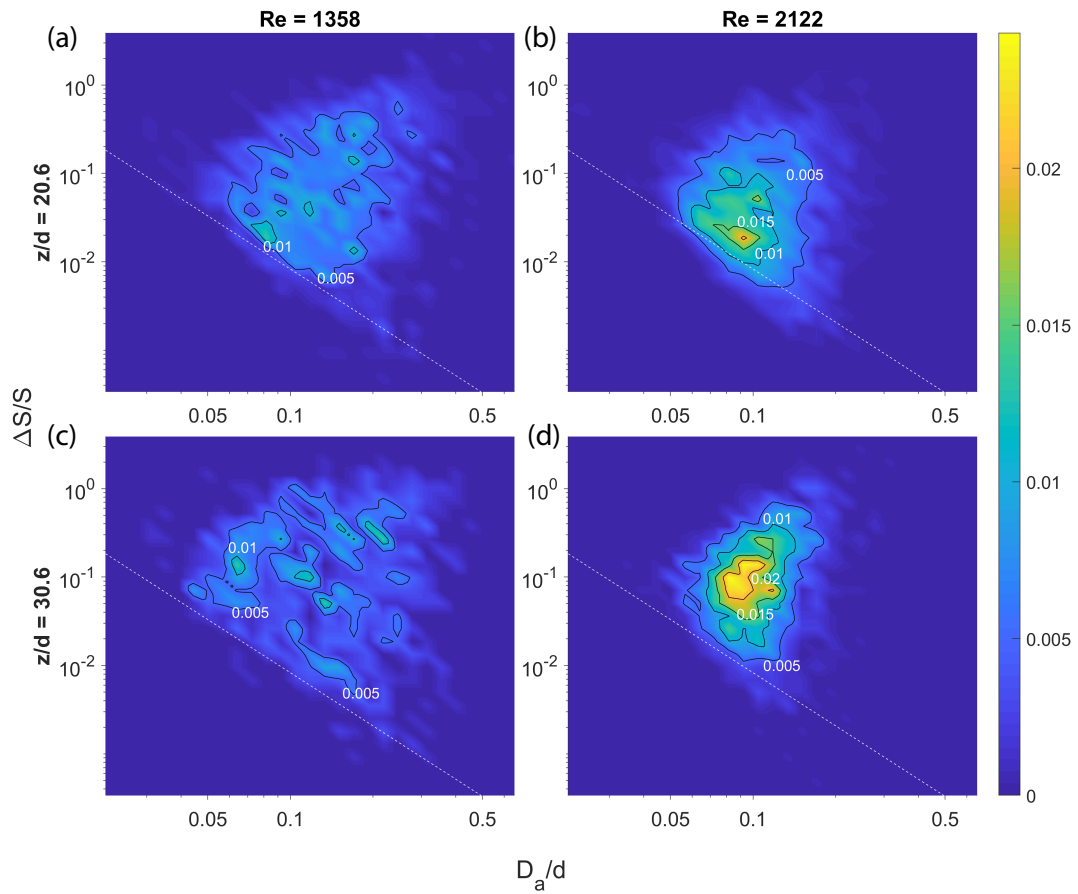
Figure 3.11: Joint probability distributions of droplet diameter and the fractional increase in interfacial area for compound droplets. (a, b) $z/d = 20.6$, (c, d) $z/d = 30.6$, left column (a, c) $Re = 1358$, and right column (b, d) $Re = 2122$. Dashed white line indicates the resolution limit.
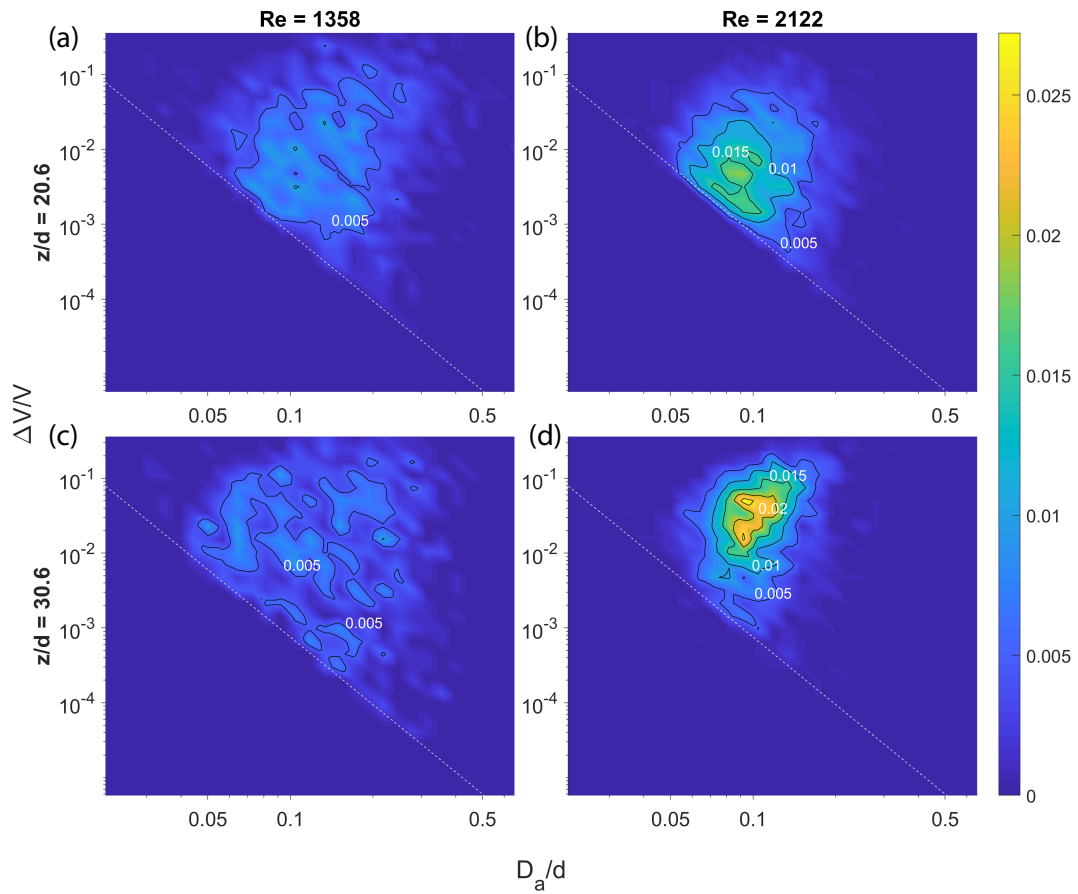
Figure 3.12: Joint probability distributions of droplet diameter and the volume fraction of water inside the compound droplets. (a, b) $z/d = 20.6$, (c, d) $z/d = 30.6$, left column (a, c) $Re = 1358$, and right column (b, d) $Re = 2122$. Dashed white line indicates the resolution limit.
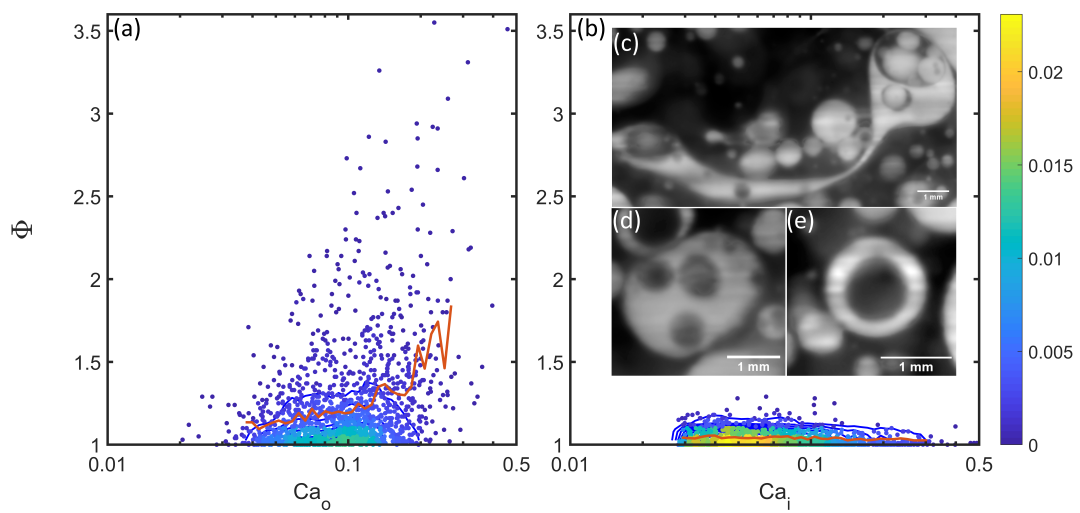
Figure 3.13: Index of asphericity of: (a) outer surface of oil droplets, and (b) inner water droplets, both for compound droplets. The line shows the average asphericity for each diameter. Insert: sample droplets with (c) $\Phi = 3.5$, (d) $\Phi = 1.5$, (e) $\Phi = 1$.

Chapter 4

Phase-conditioned turbulent statistics of an immiscible buoyant jet in the near field

This chapter focuses on the near-field flow structures, Reynolds stresses, ensemble-averaged phase distributions, and turbulence production rate of each phase in the fragmentation region of a vertical buoyant jet. The simultaneous Particle Image Velocimetry (PIV) and Planar Laser-Induced Fluorescence (PLIF) techniques will be discussed in section 4.1. Next, section 4.2 and 4.3 describes the streamwise evolution of the mean velocity profiles, root mean square (RMS) values of velocity fluctuations, and Reynolds shear stress. The differences between the evolution of the oil volume fraction and mean momentum distribution are also presented. Trends are compared with those of a single-phase jet at a very similar Reynolds number. Among the findings, the

phase-conditioned turbulence statistics reveal a sizable difference between the mean velocity, turbulence level and the Reynolds shear stress, in the two phases along the periphery of the jet. It is demonstrated that the difference in peripheral turbulence can be linked to the intermittency of the water flow. Furthermore, partitioning of the terms contributing to the turbulence production indicate that shear production is the dominant term along the periphery of the jet, and that there is a significantly higher total production rate in the water near the center line of the jet. Finally, a summary is presented in section 4.6.

4.1 Experimental techniques

Aiming to understand flow structure and turbulence associated to the fragmentation of oil jets in seawater, the present study utilizes two immiscible refractive index matched fluids that have the relevant interfacial tension, viscosity, and density ratios. The selected liquid pair consists of silicone oil (polydimethylsiloxane, trimethylsiloxy terminated) as the injected liquid, and sugar water (64% by weight) as the surrounding phase. The density and the viscosity of the dispersed silicone oil and the ambient sugar water are provided in table 3.1. Their interfacial tension, σ, is $(27 \pm 0.5)10^{-3}$ N/m. These properties and their ratio compared with that of the crude oil and sea water system are provided in section 3.1. To observe the oil, it is mixed with fluorescent dye (Nile Red).

As shown in figure 4.1, the experiments have been performed in a 39 $\times$
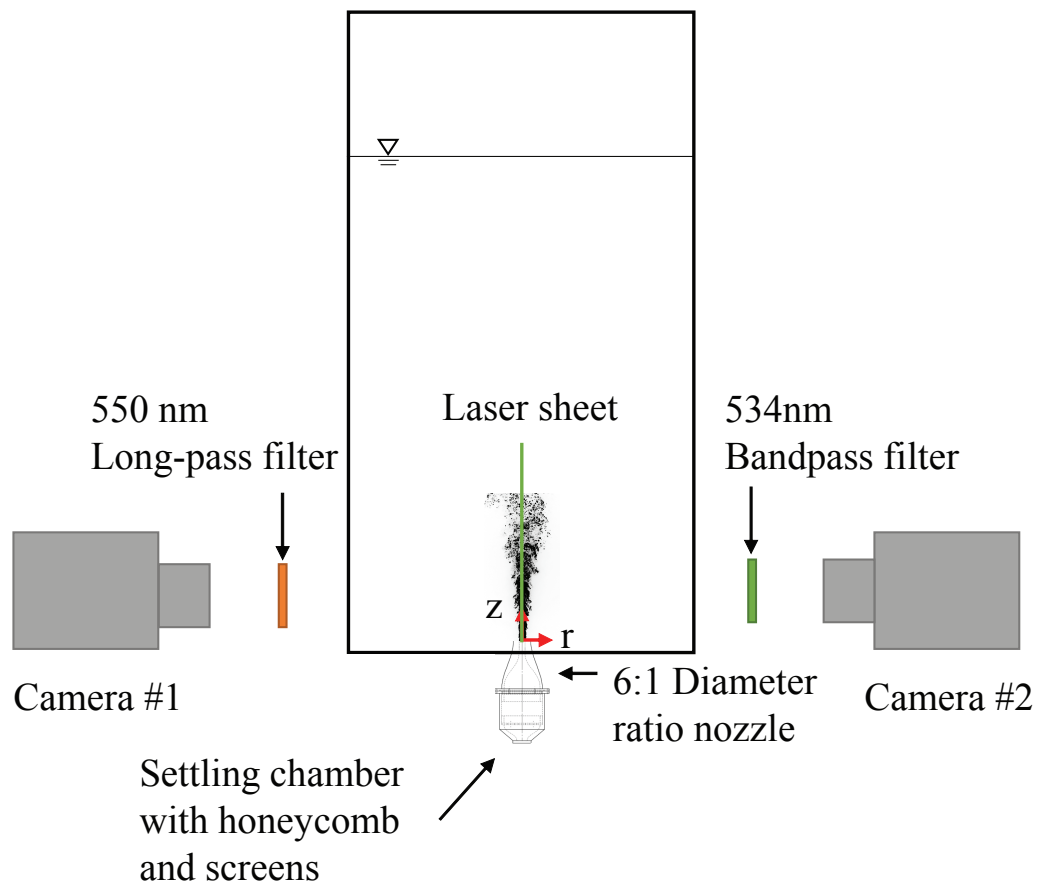
Figure 4.1: The dual camera setup for simultaneous PLIF and PIV measurements, the tank is not to scale.

24.1×76.2 cm^3 acrylic tank filled with sugar water. The silicone oil is injected from a regulated nitrogen-pressurized reservoir through a flowmeter (Omega, FL-6110A), a settling chamber containing honeycomb and screens, and a nozzle with 6.35:1 diameter ratio. The exit nozzle diameter, d, of the initially laminar jet is 10mm. In a separate set of experiments aimed at establishing a baseline, sugar water is injected using the same setup, except for the flowmeter (Omega, FL-6320ABR). The two experiments are performed at nearly the same Reynolds number. Based on the PIV measurements (described below), the centerline velocities of the oil and sugar-water jet are $U_0 = 4.2$ m/s and 0.8 m/s, respectively. The corresponding mean exit velocities, are $U_{mean} = 3.08$ m/s and 0.57 m/s. These values are calculated by integrating the mean velocity profiles close to the exit from the nozzle. The relevant non-dimensional numbers are defined as: (i) the jet Reynolds number, $Re = \rho_o U_{mean} d / \mu_o$, (ii) the Ohnesorge number, $Oh = \mu_o / \sqrt{\rho_o \sigma d}$, and (iii) the combined density and viscosity ratio, $\Gamma = \mu_o \rho_w^{1/2} / \mu_w \rho_o^{1/2}$. The jet Reynolds number are $Re = 1230$ and 1170 for the oil and single-phase water jet, respectively. The Ohnesorge number and the combined density and viscosity ratio for the oil jet are Oh=0.047, and $\Gamma = 5.61$. Based on these Re and Oh, the oil jet fall into the liquid-liquid atomization regime (Masutani and Adams, 2001).

The oil jet structure presented is measured using simultaneous PIV and PLIF in three downstream regions: $z/d = 0.1 - 2.1$, $5.7 - 7.8$, and $11.8 - 13.8$, where z is the axial location, with $z = 0$ located at the center of the nozzle. The center plane of the jet is illuminated by a sheet of pulsed 532 nm Nd:YAG laser with a thickness of about 1 mm. The synchronized PIV and PLIF images
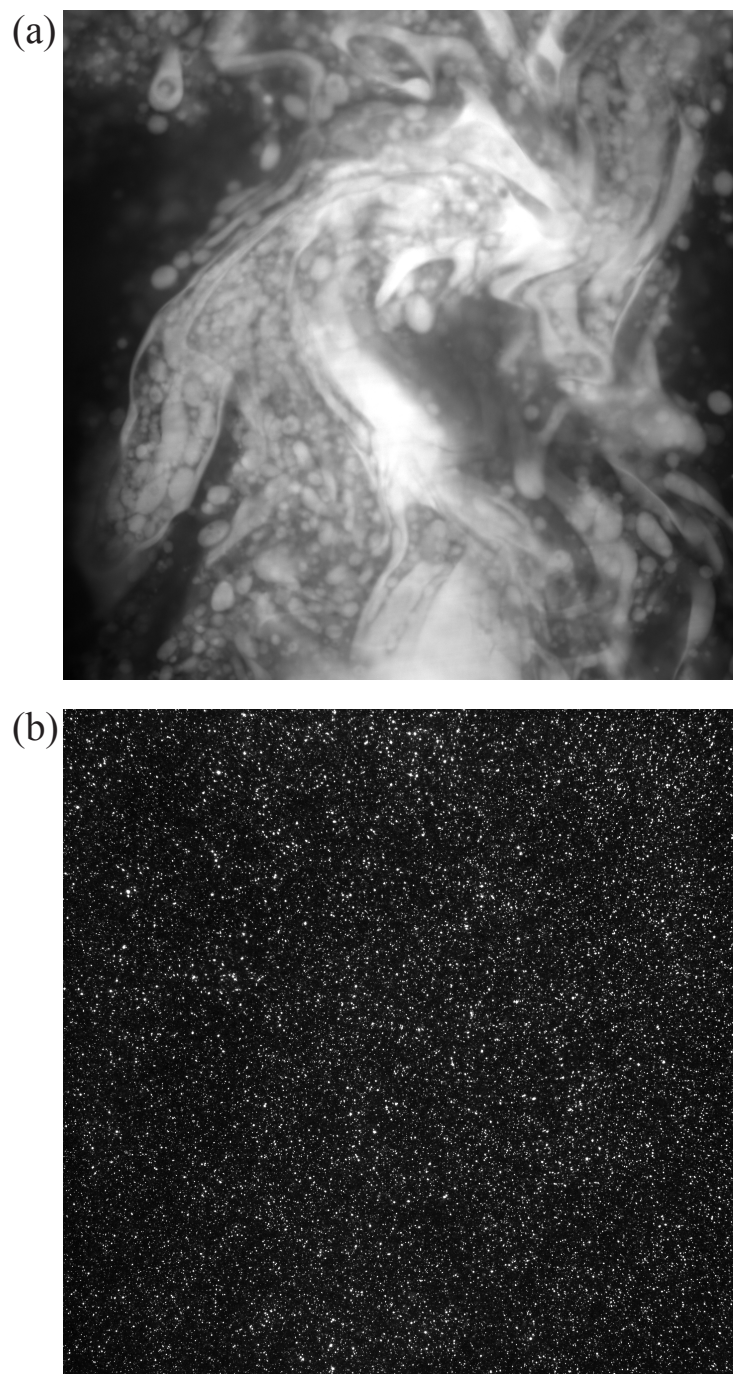
Figure 4.2: Sample of (a) raw PLIF image from camera #1, and (b) raw PIV image from camera #2. Both images are located at z/d=5.7-7.8.

are recorded with two identical cameras (PCO.dimax) located on the opposite sides of the light sheet. The fluid is seeded with 2 μm sliver-coated glass particles that have a specific gravity of 3.1. While the PIV particles reflect the laser light at the illumination wavelength, the silicone oil fluoresces at a peak wavelength of 650 nm. To separate the signals, a 534 nm fluorescence bandpass filter with 25 nm bandwidth is placed in front of the PIV camera lens to reject the fluorescent signal, and a long-pass filter with a cutoff wavelength of 550 nm is placed in front of the PLIF camera to remove the reflected 532 nm laser light. A sample pair of raw PLIF and PIV images are shown in figures 4.2(a) and 4.2(b), respectively. Both the PIV and PLIF images (2016x2016 pixel^2) are recorded at 15 image pairs per second with 50 μs interframe time. The PLIF images, which have a resolution of 11.4 μm/pixel, are positioned to cover the entire PIV field of view whose resolution is 10.7 μm/pixel. Each run lasts only a few seconds before some of the oil circulates back to the vicinity of the nozzle exit, allowing the acquisition of approximately 100 image pairs during the steady-state phase of this run. A total of 2500 realizations are recorded at each location and for each jet to obtain the flow and turbulence statistics of the jet.

For the PIV measurements, the images are enhanced, as described in Roth and Katz, 2001, and the velocity is calculated by multi-pass cross-correlations using the LaVision DaVis software. The final interrogation window size is 24×24 pixels, which with 50% overlap, provides a vector spacing of 128.5 μm. Based on the characteristic displacement and pixel uncertainty using cross-correlation, the uncertainty in the instantaneous axial velocity is 0.5% $-$ 2%.

61

Calculations of the correlation coefficient between successive instantaneous velocity vectors have confirmed that the samples are statistically independent. For the segmentation of the oil and water phase from the PLIF data, a random forest-based pixel-wise classification is applied, the details of which are provided in the pervious chapter 3. Spatial matching between the PIV and PLIF images is performed by placing a transparent dotted grid at the jet centerline and recording its image by both cameras. An affine geometric transformation and bicubic interpolation are used for precise images registration of corresponding images. For the experiments aimed to obtain baseline single-phase data of a sugar water jet injected into sugar water, the PIV image pairs have been recorded at 1Hz with 300 μs inter-pair delay using a 6600×4400 pixel^2 camera. In this case, the total number of realizations is 1000, and the resolution of the PIV images is 14.8 μm/pixel, which corresponds to a vector spacing of 177.6 μm.

4.2 Flow structures and mean flow characteristics

To characterize the near field evolution of the buoyant oil jet structures, we first examine the flow and oil-water interfaces at three different streamwise locations. Samples of contour maps of instantaneous velocity magnitude are presented separately for the oil and water phases in figures 4.3, 4.4, and 4.5. Note that for convenience, different signs of r are used to denote the opposite sides of the jet. The left column focuses on the oil, and the right column, on the water. At $z/d = 0.1 - 2.1$ (figure 4.3a and 4.3b), the interface becomes wavy
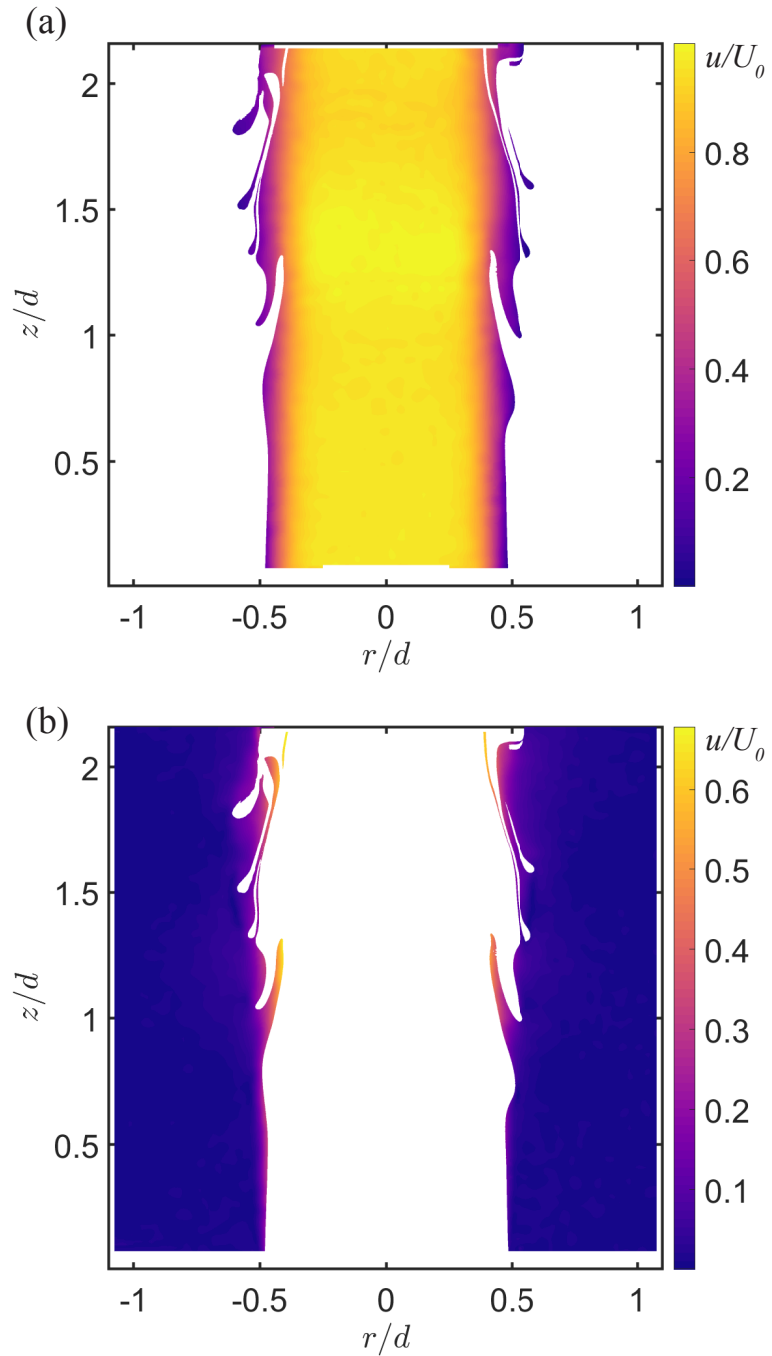
Figure 4.3: Samples of instantaneous velocity magnitude, u, normalized by the jet mean centerline exit velocity, $U_0 = 4.2$ m/s, at $z/d = 0.1 - 2.1$. (a) oil phase, and (b) water phase.
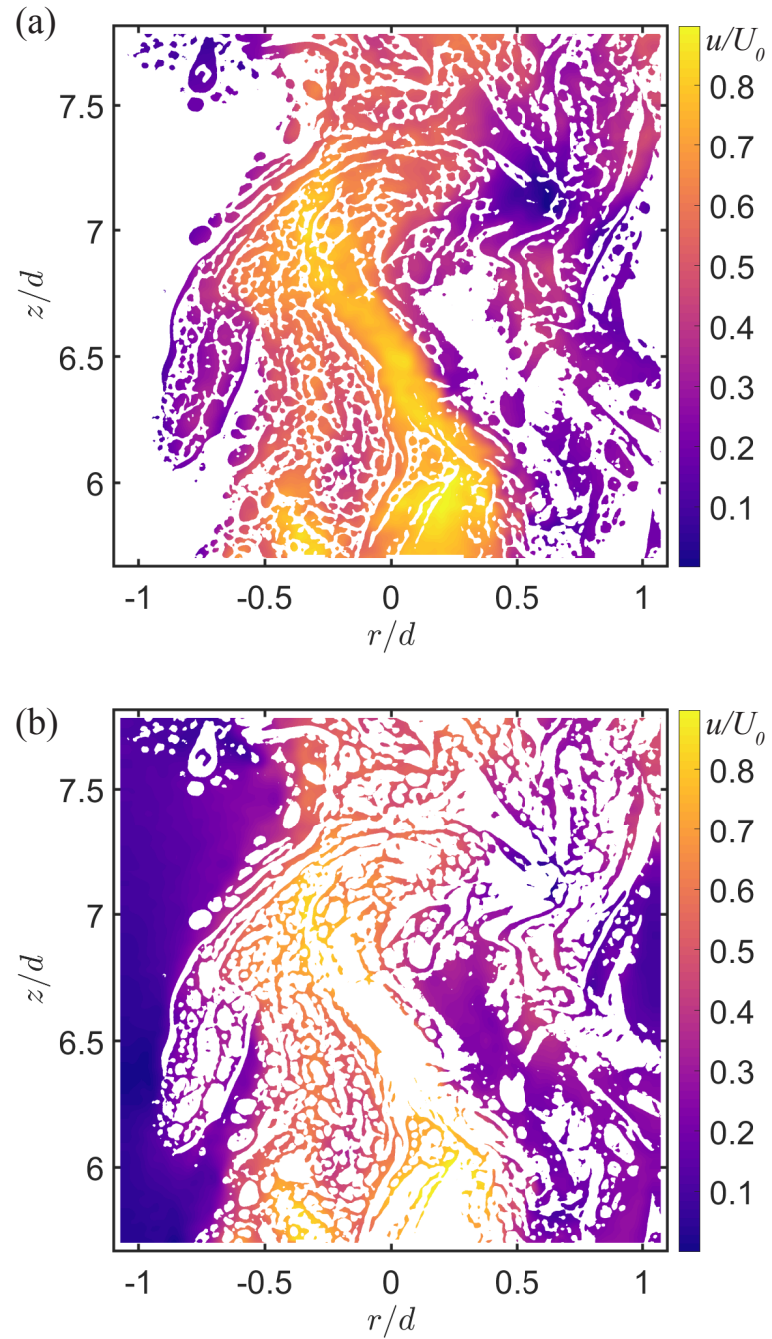
Figure 4.4: Samples of instantaneous velocity magnitude, u, normalized by the jet mean centerline exit velocity, $U_0 = 4.2$ m/s, at $z/d = 5.7 - 7.8$. (a) oil phase, and (b) water phase.
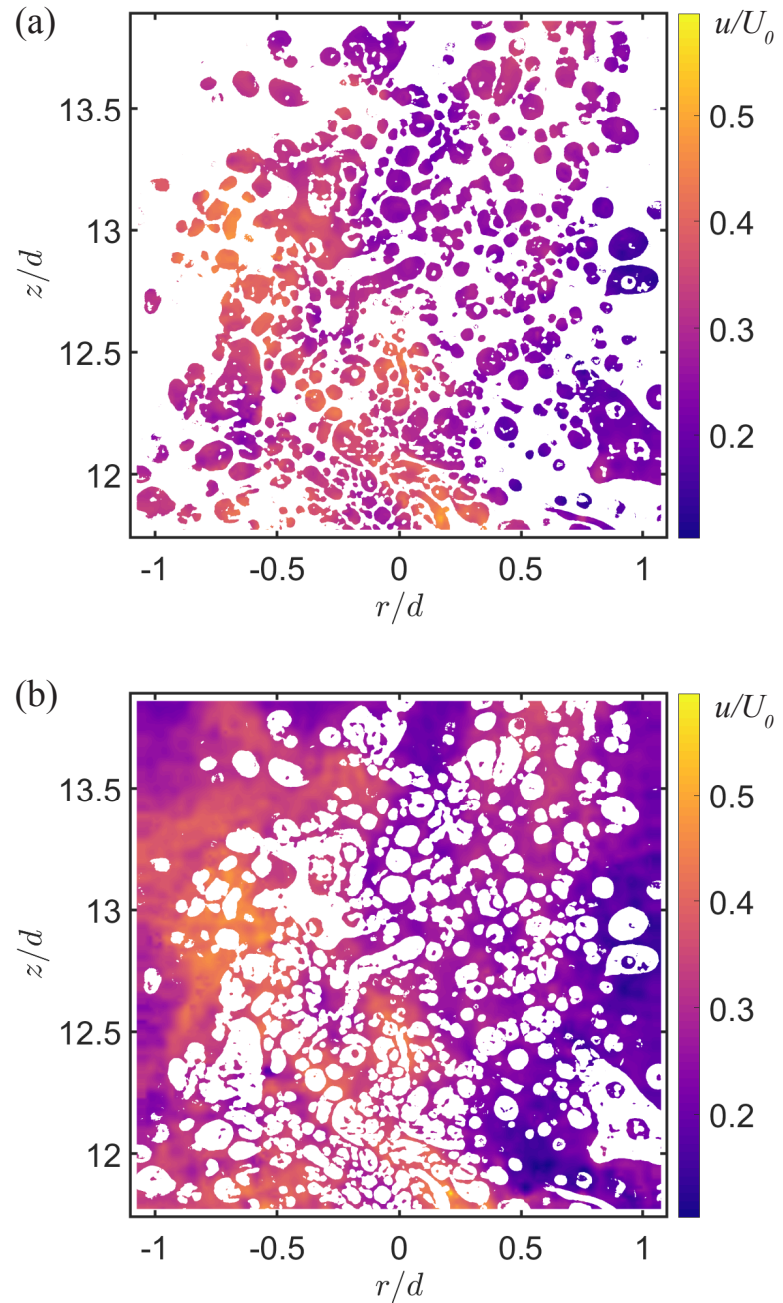
Figure 4.5: Samples of instantaneous velocity magnitude, u, normalized by the jet mean centerline exit velocity, $U_0 = 4.2 \, \text{m/s}$, at $z/d = 11.8 - 13.8$. (a) oil phase, and (b) water phase.

due to the Kevin-Helmholtz (K-H) instability, with most of the momentum concentrated in the oil. Most of the ambient flow has a very low velocity, except for the regions where the water ligaments begin to penetrate into the oil, and oil ligaments start to extend outward. There, the water velocity increases rapidly, reaching about 60% of the U_0. A closer look at another sample is presented in Figure 4.6 and 4.7, focuses on the early K-H rollup along with the oil-water interface. Even before entrainment, the vorticity is already extended to both phases, and once the ligaments form, the water momentum increases rapidly. The vortices forming in the water appear to be centered around the tips of the oil ligaments, e.g. at $r/d = -0.58$ and $z/d = 1.14$. Interestingly, in these regions, the vorticity is mostly concentrated in the water, while the oil ligaments mostly have low vorticity.

Further downstream, at $z/d = 5.7 - 7.8$ (figure 4.4a and 4.4b), the oil is partially fragmented and meanders, but still maintains a high momentum core containing mostly oil. Water with high velocity already appears between the fragmenting oil blobs. The periphery contains both oil and water ligaments with low momentum and sizes comparable to the jet diameter. Fragmentation continues at $z/d = 11.8 - 13.8$ (figure 4.5a and 4.5b) with some of the oil blobs already broken into separate droplets, many appearing to be compound droplets, consistent with the observations reported in chapter 3. A meandering region with elevated momentum is still evident, but it contains a mixture of both phases. Outside of it, the velocity of both phases is low with magnitudes falling in the $0.2 - 0.3U_0$ range.

To characterize the ensemble-averaged near-field, we first quantify the
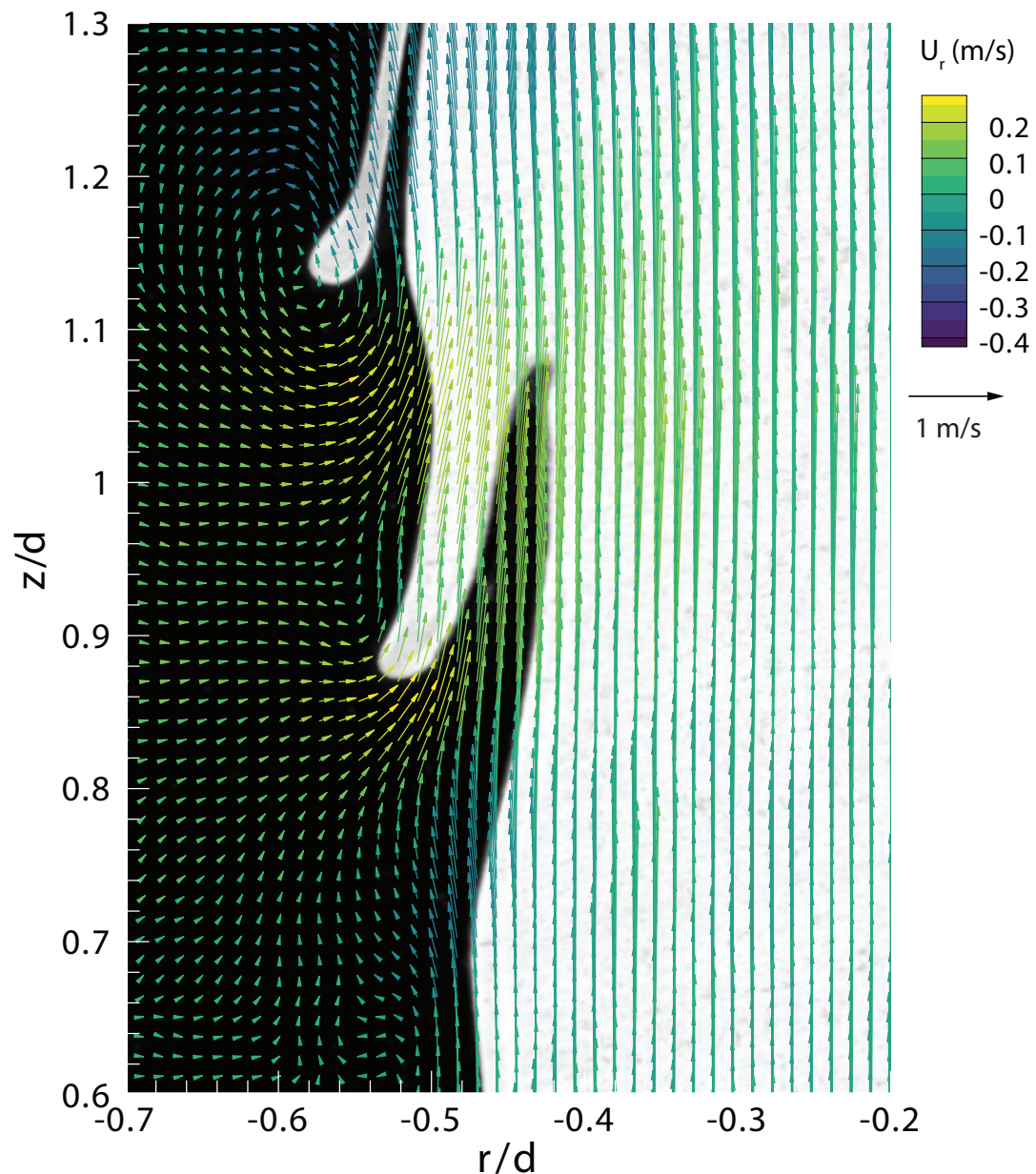
Figure 4.6: A sample of magnified instantaneous flow field of oil jet in water overlaid with the oil-water interface; Vectors are diluted and rescaled for clarity.
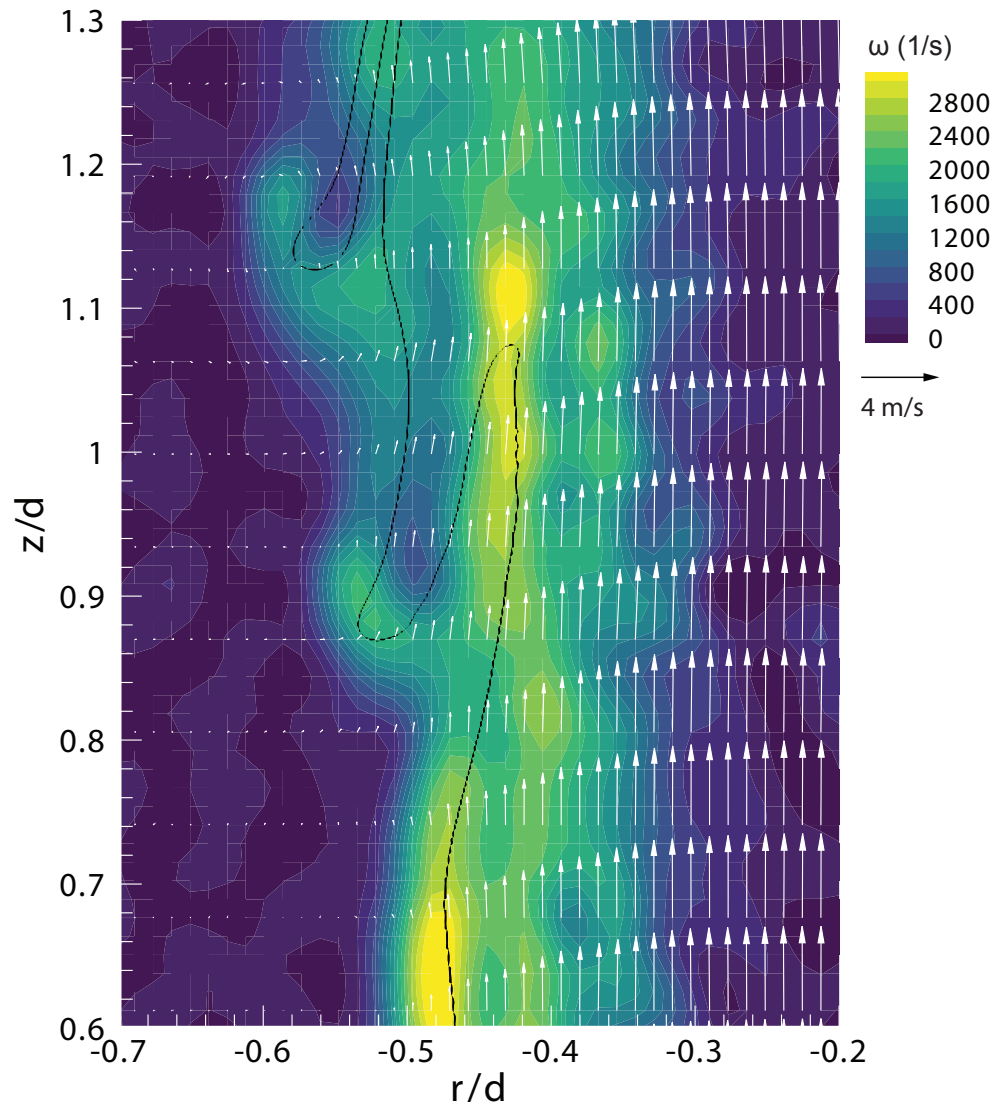
Figure 4.7: A sample of the same magnified instantaneous flow field of oil jet in water overlaid with vorticity magnitude. Vectors are diluted and rescaled for clarity.

axial development of two jet spreading indicators: (i) the velocity half-width, $b_{1/2}$, defined as the radial location where the mean velocity decreases to half of its local centerline values, and (ii) the jet oil fraction half-width, $b_{\gamma 1/2}$, where the oil volume fraction decreases to half of its local centerline value. Figure 4.8(a) shows the streamwise evolution of $b_{1/2}$ and $b_{\gamma 1/2}$ for the oil jet and compares the to $b_{1/2}$ of the single-phase jet at nearly the same Reynolds number. Figure 4.8(b) presents the corresponding values of the centerline velocity, U_{cl}. For the single-phase baseline case, near the nozzle, the half-width remains nearly constant up to $z/d = 7$. Accordingly, the centerline mean velocity remains very close to that at the nozzle exit, with only a slight (3%) decay by $z/d = 7$. At $z/d > 8$, $b_{1/2}$ increases almost linearly with z/d. The spreading rate, $S = \partial b_{1/2}/\partial z$, is equal to 0.11, consistent, e.g. with a prior study of single-phase jet ($S = 0.113$) at a moderate but higher Reynolds number, $Re = 2679$ (Lai and Socolofsky, 2019). The decay of the centerline velocity is typically defined as $U_0/U_{cl}(z) = C(z - z_0)/d$, where C is the decay rate and z_0 is the virtual origin (Hussein, Capp, and George, 1994). Fitting to the current data gives $C = 0.24$ and $z_0 = 3.4d$, consistent with a prior study at a similar Reynolds number ($Re = 1350$) by Todde, Spazzini, and Sandberg, 2009, where $C = 0.24$, and $z_0 = 3.0d$. In Lai and Socolofsky, 2019, $C = 0.17$.

For the oil jet, $b_{1/2}$ and the centerline velocity remains unchanged at $z/d = 0.1$ to 2.1. By $z/d = 5.8$, the jet is already expanding, and the streamwise velocity is decreasing, both earlier than that of the single-phase jet. Yet, once it starts, the spreading rate of the oil jet, $S = 0.10$, is quite similar to that of the single-phase case all the way up to $z/d = 14$. Accordingly, the centerline
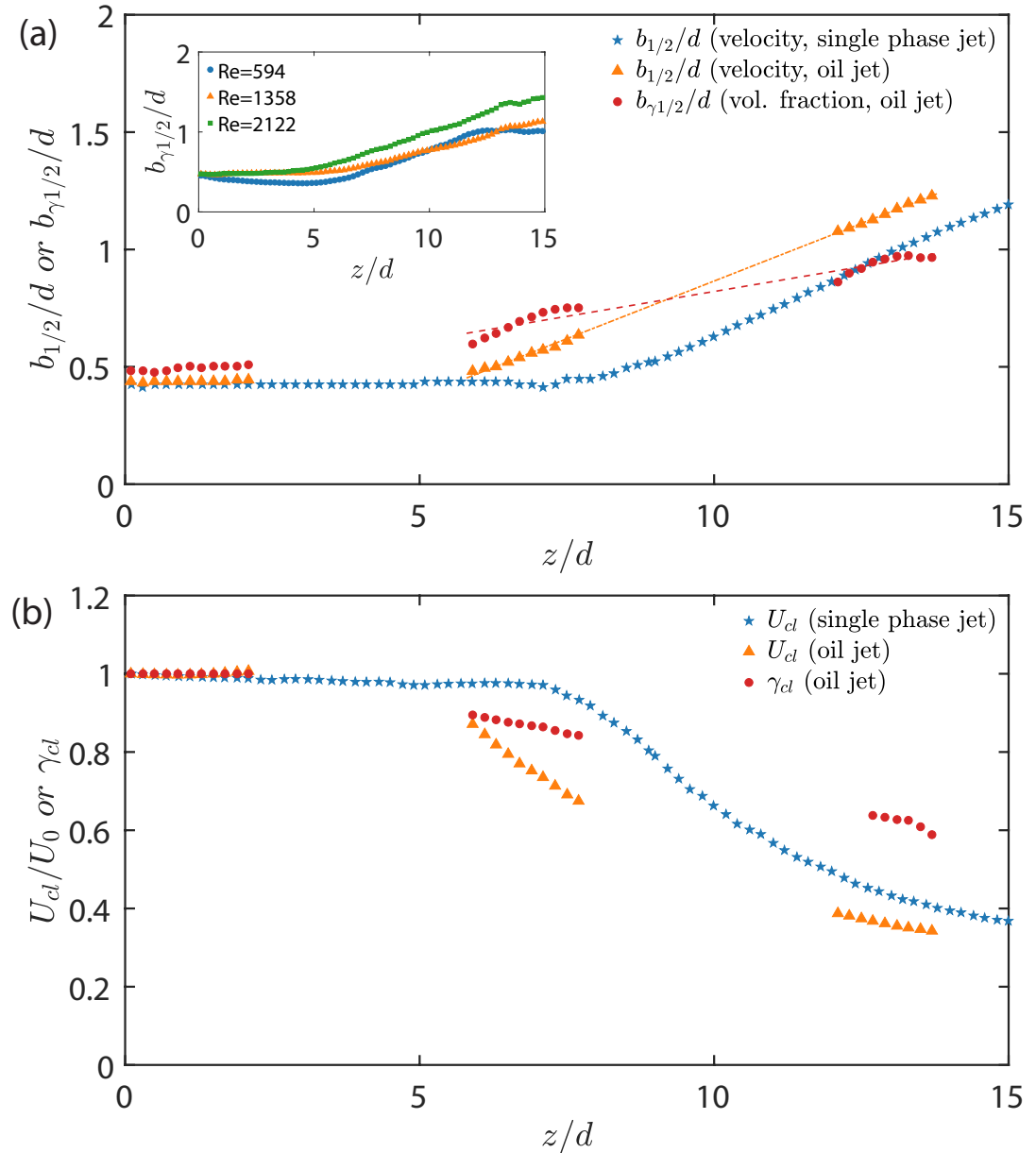
Figure 4.8: (a) Axial development of the jet half widths with distance calculated from the velocity, $b_{1/2}$ for the single phase and oil jet, and the oil volume fraction, $b_{\gamma 1/2}$. Dashed lines are added to show trends. Inset shows the axial development of the $b_{\gamma 1/2}$ different jet Reynolds number calculated from PLIF data in Chapter 3. (b) Axial development of the jet centerline velocity, U_{cl}, normalized by jet mean centerline exit velocity: U_0 =4.2 m/s for oil jet, and 0.8 m/s for single phase jet, and the centerline oil fraction, γ_{cl}.

velocity of the oil jet start to decrease along the axial direction with the same decay rate $C = 0.24$ of the single-phase jet. The growth rate of the oil fraction half-width is different. Near the nozzle, $b_{\gamma 1/2}$ increase slightly but remains close to $0.5d$. Then, it increases at a faster rate than the velocity half-width up to $z/d = 5.8$. In the $z/d = 5.7$ to 7.8 range, both half widths increase at rates that are not significantly different, with $b_{\gamma 1/2} > b_{1/2}$. Further downstream, while $b_{1/2}$ keeps on growing linearly, the growth rate of $b_{\gamma 1/2}$ decreases, resulting in $b_{\gamma 1/2}$ being smaller than $b_{1/2}$ at $z/d > 11.9$. The ratio of the oil half widths, namely $\lambda = b_{\gamma 1/2}/b_{1/2}$, averaged over the measurement domains decreases from 1.2 at $z/d = 5.7 - 7.8$ to 0.8 at $z/d = 11.8 - 13.8$. The present value of λ at $z/d = 5.8 - 7.9$ is consistent with those ($\lambda \approx 1.2$) of some miscible buoyant jets and plumes (Burridge et al., 2017; Ezzamel, Salizzoni, and Hunt, 2015; Panchapakesan and Lumley, 1993b; Papanicolaou and List, 1988), and higher than $\lambda \approx 1$ reported by (Wang and Law, 2002). Yet, in all these miscible jet studies, λ remains above 1 further downstream, i.e. significantly larger than the present value at $z/d = 11.9 - 14$. Accordingly, between $z/d = 5.8$ to 14, the presently measured spreading and decay rates of the oil volume fraction, $S = 0.042$ and $C = 0.07$, are smaller than those ($S = 0.047 - 0.071$, $C = 0.07 - 0.23$) reported for the miscible jet (Charonko and Prestridge, 2017; Djeridane et al., 1996). A likely reason for the different trends involves the buoyancy effect associated with the persistent presence of droplets. While the two fluids mix irreversibly in the miscible jet, causing a reduction in the effect of buoyancy, the cloud of droplets evident at $z/d = 11.8 - 13.8$ persists, and continues to be influenced by buoyancy. Hence, the oil droplets continue to rise at a faster rate than the surrounding liquid and are less prone to diffuse

radially outward. Since the droplet rise velocity increases with diameter, one would expect that an immiscible jet with weaker buoyancy effect, e.g. having smaller droplets, would spread at a faster rate. With increasing Reynolds number, the size of droplet decreases, as shown for the present jet geometry in chapter 3, and consistent with prior studies (Johansen, Brandvik, and Farooq, 2013; Saito, Abe, and Koyama, 2017). Consequently, the oil jet should spread at a faster rate with increasing Reynolds number. Indeed, as shown in the inset presented in figure 4.8a for the experiments described in chapter 3, which provide data for phase and size distributions, but do not involve velocity measurements, $b_{\gamma 1/2}$ at $Re = 2122$ is higher than those the lower Reynolds numbers. The effects of buoyancy and droplet size on the relative velocity between phases are discussed further in section 4.4.

As demonstrated in figure 4.9a, although the present measurements focus on the near-field, the normalized radial profile of the mean axial velocity of the oil jet, $U_z(r,z)/U_{cl}(z)$, still collapse at $z/d \geq 6$, namely appears to develop a self-similar behavior. The top-hat profiles are only limited to the very near field, as shown for $z/d = 1$ and 2. In this range, the mean shear is concentrated along the jet perimeter. Since the spreading of the single-phase jet starts later, its profiles at $z/d = 6$ and 7 have not reached a self-similar state (figure 4.9b). However, once it does, its normalized profiles at $z/d = 12.5$ and 13.5 collapse, and furthermore, appear to have a very similar shape as that of the self-similar oil jet. Hence, the evolution of the mean velocity can be characterized based on $b_{1/2}$ and U_{cl}. The profiles of oil volume fraction plotted vs. $r/b_{1/2}$ is presented in figure 4.10a, and the same data normalized
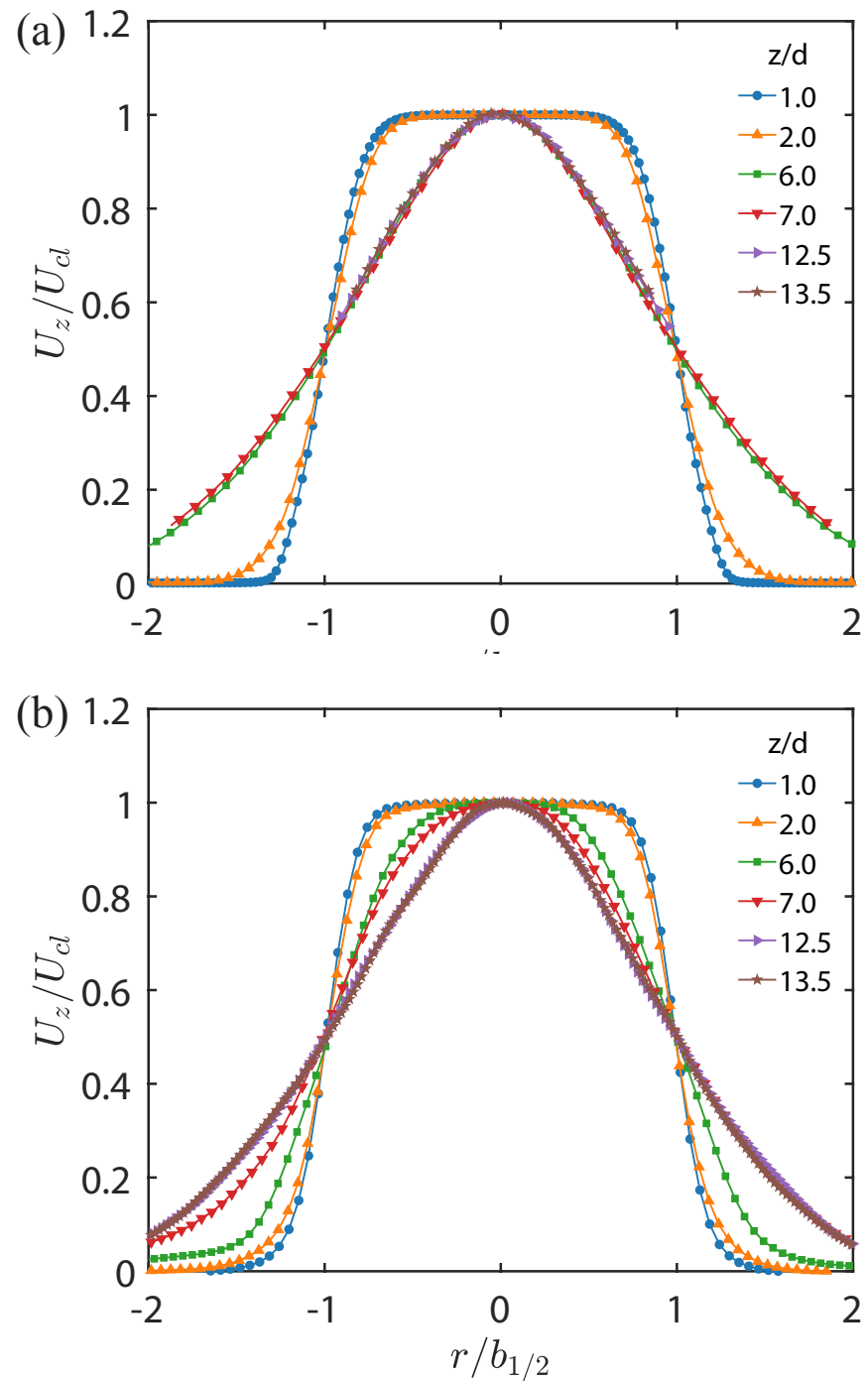
Figure 4.9: Radial profiles of mean axial velocity normalized by the local centerline velocity U_{cl} and velocity half-width $b_{1/2}$, (a) oil jet in water, and (b) single-phase jet.

by γ_{cl} and plotted vs. $r/b_{\gamma 1/2}$ is shown in figure 4.10b. The top hat profiles are confined to the very near field. At $z/d > 6$, all the void fraction profiles collapse; hence their trends could be characterized based on $b_{\gamma 1/2}$ and γ_{cl}. However, note that the shape of the velocity profiles differs from those of the void fraction. The latter decay at a faster rate along the jet periphery, namely, the oil phase is more concentrated near the center of the jet than the jet momentum. Accordingly, the phase profiles are more rounded near the center. The impact of the differences between $b_{1/2}$ and $b_{\gamma 1/2}$ is demonstrated in figure 5a, where $\lambda > 1$ at $z/d = 6 - 7$ implies a broader distribution, and $\lambda < 1$ at $z/d = 12.5 - 13.5$ indicates that the oil is predominantly concentrated near the center of the jet.

4.3 Turbulence statistics

To provide insights for the dynamics that arises within the immiscible buoyant jet, we combine the phase distribution data obtained from the refractive index matched PLIF data to the measurements of the velocity field. Following Burridge et al., 2017, the instantaneous velocity field is interrogated using a Heaviside step function, $H(r, z, t)$, whose value is unity in the oil and zero in the water. Then the phase-conditioned ensemble-averaged velocity in the oil, $U_{i,o}(r, z)$, and in the water, $U_{i,o}(r, z)$, are defined as

$$U_{i,o}(r,z) = \frac{1}{\sum H} \sum_{p=1}^{M} H(r,z,t_p) u_i(r,z,t_p) \tag{4.1}$$
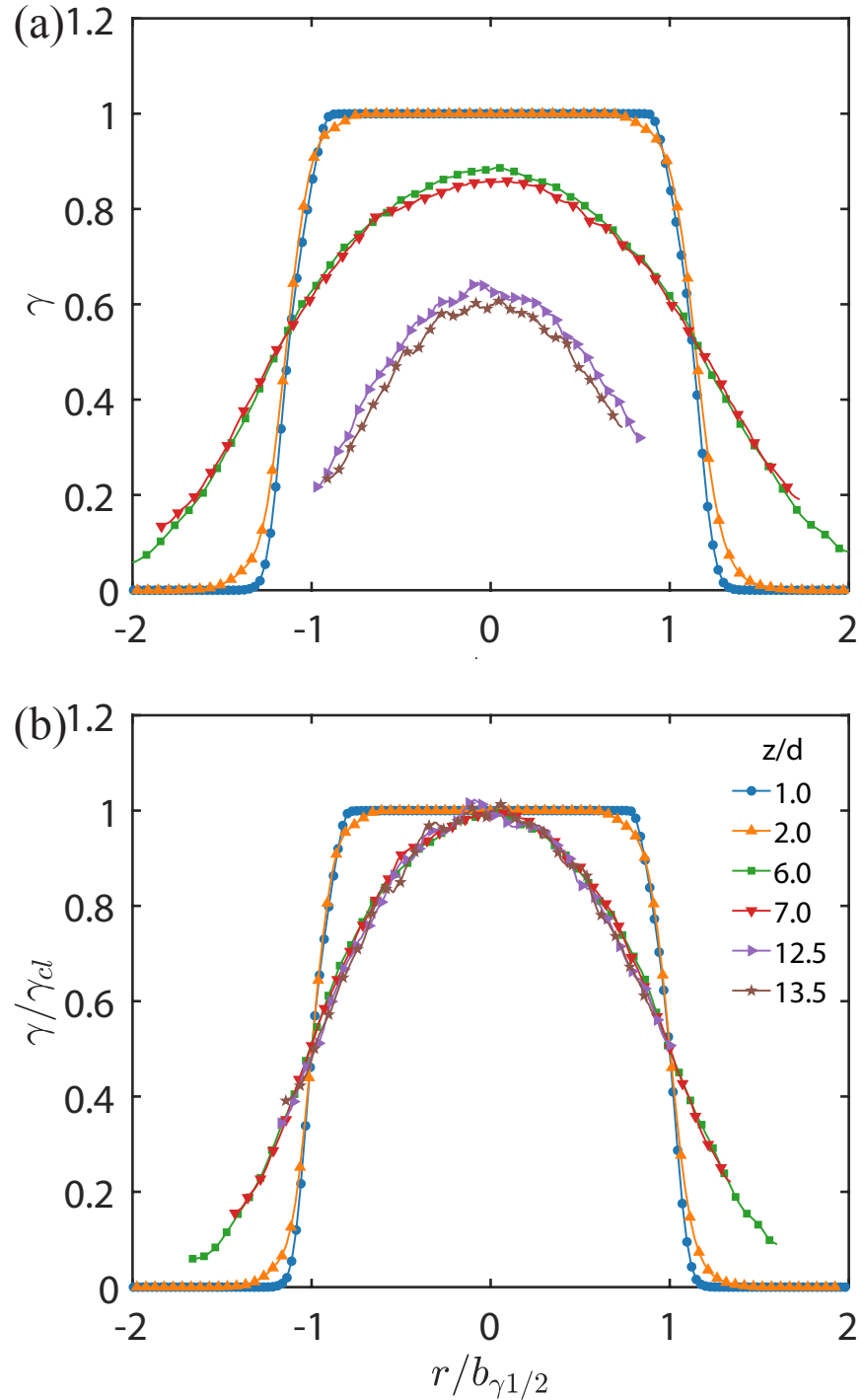
Figure 4.10: Radial profiles of the oil volume fraction. (a) radial location is normalized by $b_{1/2}$, (b) Same data with phase fraction normalized by local centerline fraction γ and radial location normalized by phase half-width $b_{\gamma 1/2}$.

and

$$U_{i,w}(r,z) = \frac{1}{M - \sum H} \sum_{p=1}^{M} [1 - H(r,z,t_p)]u_i(r,z,t_p) \tag{4.2}$$

where M is the total number of measurements at each location. Similarly, to examine the fluctuating velocity components, i.e. $u_i' = u_i - U_i$, in each phase, the RMS values of velocity fluctuations are

$$\langle u_{i,o}' u_{j,o}' \rangle = \frac{1}{\sum H} \sum_{p=1}^{M} H(r,z,t_p)u_i'(r,z,t_p)u_j'(r,z,t_p) \tag{4.3}$$

and

$$\langle u_{i,w}' u_{j,w}' \rangle = \frac{1}{M - \sum H} \sum_{p=1}^{M} [1 - H(r,z,t_p)]u_i'(r,z,t_p)u_j'(r,z,t_p) \tag{4.4}$$

where $\langle \; \rangle$ indicates ensemble averaging. The Reynolds averaged momentum equation for each phase, neglecting the viscous terms, can be written as (Drew and Lahey, 1993),

$$\frac{\partial(\gamma U_{i,o} U_{j,o})}{\partial x_i} = -\frac{1}{\rho_o}\frac{\partial(\gamma p)}{\partial x_j} - \frac{\partial(\gamma \langle u_{i,o}' u_{j,o}' \rangle)}{\partial x_i} + K_{i,o} + g_i \tag{4.5}$$

$$\frac{\partial[(1-\gamma)U_{i,w}U_{j,w}]}{\partial x_i} = -\frac{1}{\rho_w}\frac{\partial[(1-\gamma)p]}{\partial x_j} - \frac{\partial[(1-\gamma)\langle u_{i,w}' u_{j,w}' \rangle]}{\partial x_i} - K_{i,o} + g_i \tag{4.6}$$

where the $K_{i,o}$ is the so-called interaction term accounting for the effect of the water phase on the momentum of the oil. Combining the momentum equations for both phases, the fraction weighted Reynolds stresses then becomes:

$$\widetilde{\langle u_i' u_j' \rangle} = \gamma \langle u_{i,o}' u_{j,o}' \rangle + (1 - \gamma) \langle u_{i,w}' u_{j,w}' \rangle \qquad (4.7)$$

The discussion starts with a comparison between the fraction weighted Reynolds stresses of the oil jet and those of the single-phase jet. Figure 4.11, 4.12 and 4.13 shows the axial evolution of the profiles of $\widetilde{\langle u_z' u_z' \rangle}^{1/2}$, $\widetilde{\langle u_r' u_r' \rangle}^{1/2}$, $\widetilde{\langle u_z' u_r' \rangle}$, and the corresponding results for the single-phase jet, respectively. In general, the scaled near field turbulence in the oil jet is significantly higher than that in the single-phase jet, but the difference between them decreases with increasing z/d. Initially, both the axial and radial components of the turbulence have peaks coinciding with the azimuthal shear layer along the periphery of the jet. Further downstream, the location of the highest turbulence level shifts to the center of the jet. This transition occurs between $z/d = 6$ to 7 for the oil jet and further downstream for the single-phase jet. For the latter, both the transition and the magnitude of the turbulence components are consistent with previously published results at similar Reynolds numbers (Todde, Spazzini, and Sandberg, 2009). Also, for both jets, the scaled axial and radial RMS values increase with z/d, but this increase diminishes at $z/d = 12.5 - 13.5$, especially for the oil jet. It appears that in this range, the two profiles already collapse, indicating that the streamwise (and radial) velocity fluctuations can already be scaled using $b_{1/2}$ and U_{cl}. Even at this location, the centerline axial RMS peak of the oil jet, being around 0.29, is higher than that of the single-phase jet by about 14%, but the radial peak (0.21) of the oil jet is only slightly higher. For both cases and at all locations, the radial fluctuations are smaller than the axial ones, also consistent with

77
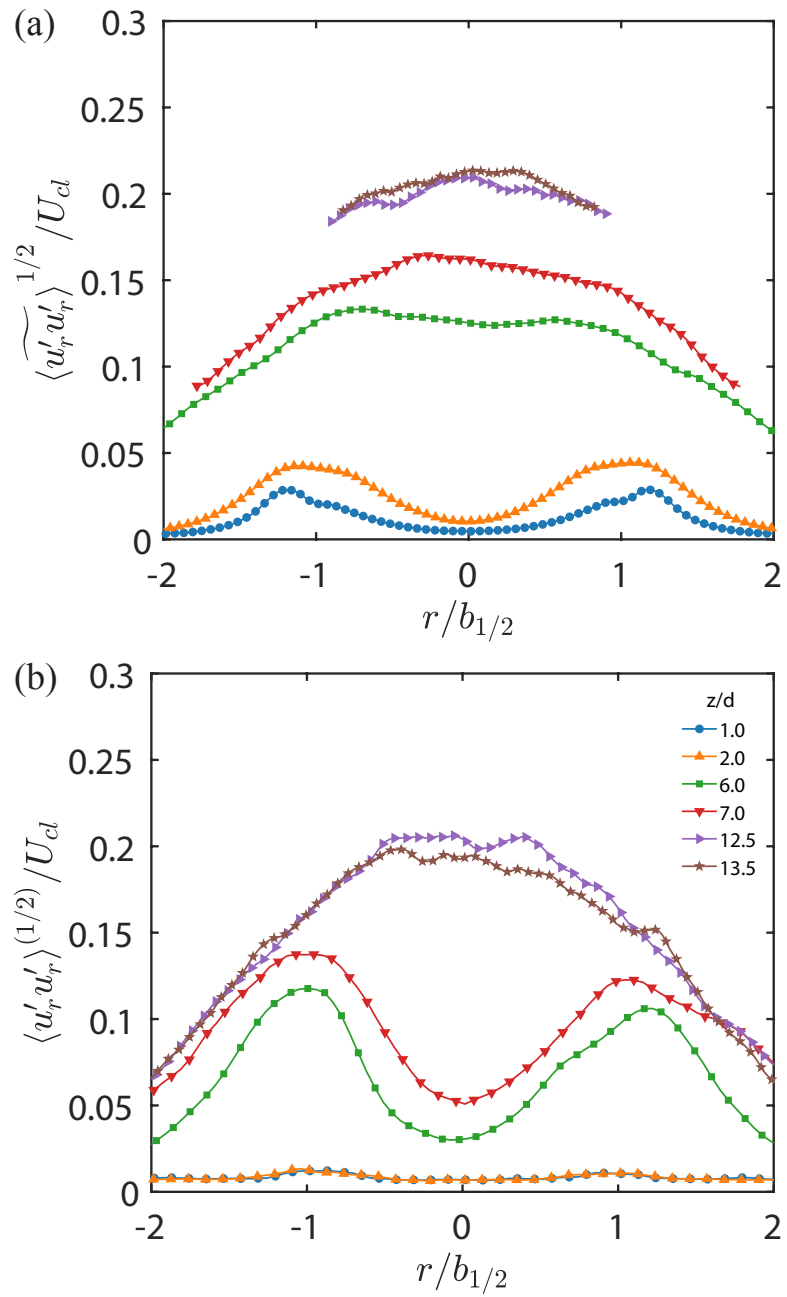
Figure 4.11: Radial profiles of the axial RMS velocity for (a) oil jet in water, and (b) single-phase jet.
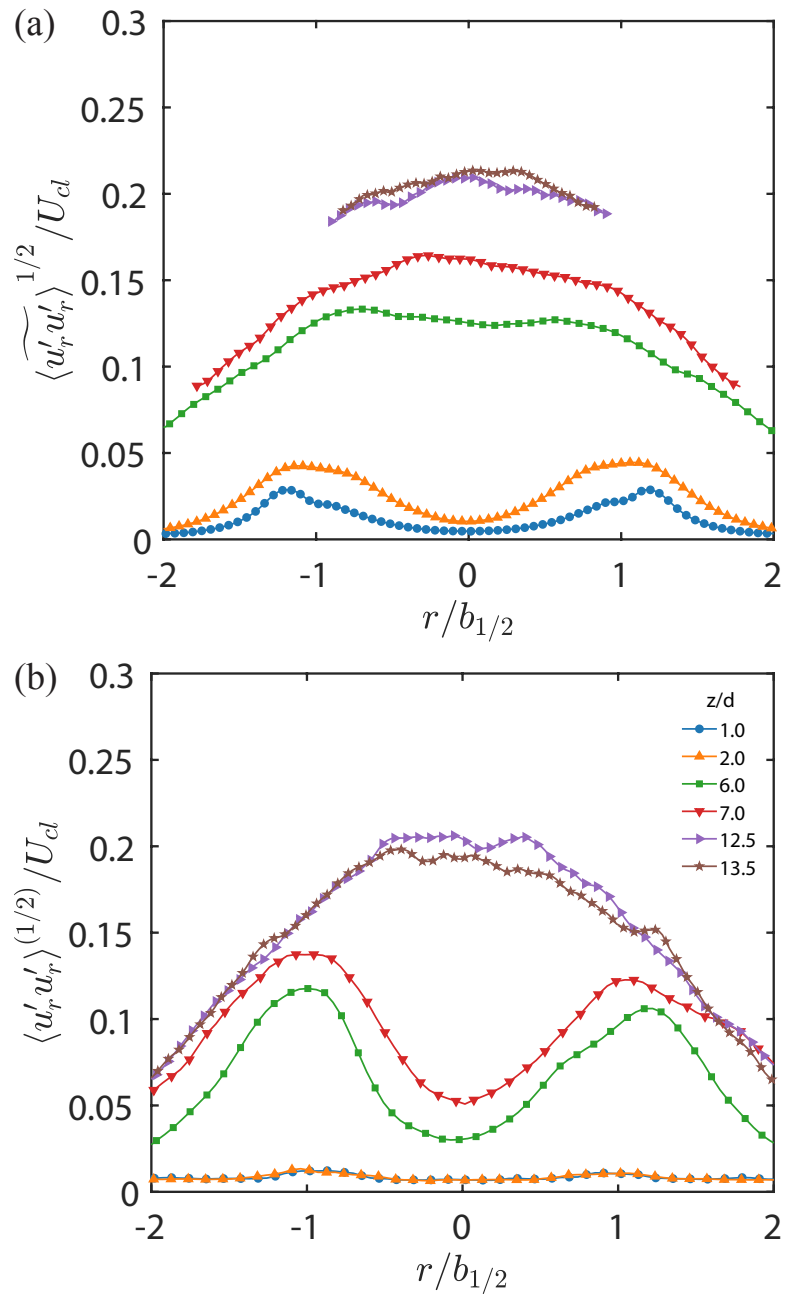
Figure 4.12: Radial profiles of the radial RMS velocity for (a) oil jet in water, and (b) single-phase jet.

published results for single phase jets (Hussein, Capp, and George, 1994; Lai and Socolofsky, 2019). The scaled Reynolds shear stresses (figure 4.13a and b), as expected, show growing double peaks near the jet periphery, with the centerline value being zero. Similar to the normal components, the shear stresses in the oil jet are higher than those in the single-phase jet at all elevations, but the difference between them decreases with increasing z/d. The maximum value for the single phase jet at $z/d = 12.5 - 13.5$, 0.021, is in good agreement with previous results (Hussein, Capp, and George, 1994; Lai and Socolofsky, 2019). At $z/d = 1$ and 2, the single-phase values are very small, indicating that the flow there is essentially laminar. In the oil jet, entrainment of the surrounding water, formation of ligaments, and the previously discussed vortices (figure 4.6 and 4.7) already result in low magnitude stresses of about 1.6×10^{-3}, which are highlighted in the insert.

Another notable difference between the jets is the secondary hump in the $\langle u'_z u'_z \rangle^{1/2}$ profile of the single phase jet at $z/d = 7$, which does not appear a short distance upstream ($z/d = 6$). Examination of the instantaneous realizations indicates that this phenomenon is associated with pairing of the K-H vortex that occurs preferentially at this elevation. As demonstrated in figure 4.14 and 4.15, while the vortices start to roll up at a lower elevation, they do not begin to pair until $z/d = 6.8 - 7.4$. Here, figure 4.15 shows multiple distinct clusters of vorticity peaks, with one of them being pushed radially inward to $r/d = -0.55$, and the others being pushed outward to $r/d > 0.7$. The locations of $\langle u'_z u'_z \rangle^{1/2}$ peaks and humps, which are marked with red symbols, can be used for comparing the scaled profiles to the physical
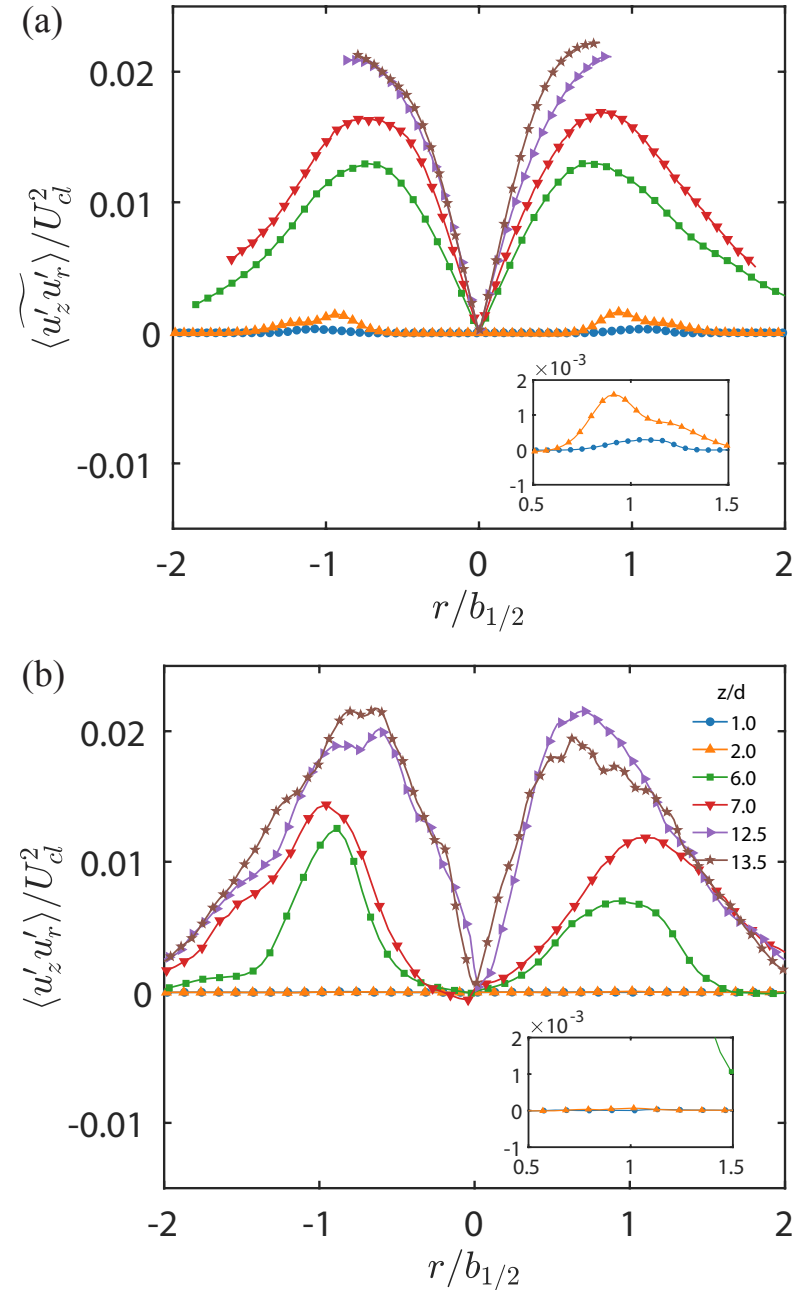
Figure 4.13: Radial profiles of the Reynolds shear stress for (a) oil jet in water, and (b) single-phase jet.

ones. Further downstream, the secondary hump no longer exists beyond the potential core of the jet. These phenomena are not observed in the oil jet.

4.4   Phase conditioned Statistics

To investigate the contribution of each phase to the mean velocity profiles, figure 4.16 compares the axial evolution of the normalized mean velocity profiles of the two phases. Owing to the differences in magnitude, the streamwise velocity plots appear to be smooth, but the radial ones jitter, in part due to the uncertainty limit (10% of U_0), and in part due to the limited sample size of water in the middle of the jet, and oil along the periphery. Close to the nozzle, at $z/d = 1$ and 2, the streamwise velocity profile of the oil remains a flat top, and there is a very small overlap with the water along the jet periphery. The water in this overlap region has nearly the same axial velocity as that of the oil. However, at $z/d = 2$, the velocity of the oil is slightly larger than that of the water (by 7% of U_{cl}). The corresponding radial velocity profiles (figure 4.16b) indicate that the oil radial velocity is essentially zero in the jet core with a slight increase near $r/b_{1/2} = \pm 1$. In contrast, the radial water velocity outside the jet remains negative, presumably owing to entrainment, with a slight magnitude increase in the overlap region. Hence, in the small overlap region, the oil is moving radially outward while the water is moving inward. This trend persists at $z/d = 6$ and 7, where some water has already penetrated to the center of the jet (figure 4.4). Here, the oil has a significantly higher axial velocity than that of the water across the entire jet, but the profiles of each

82
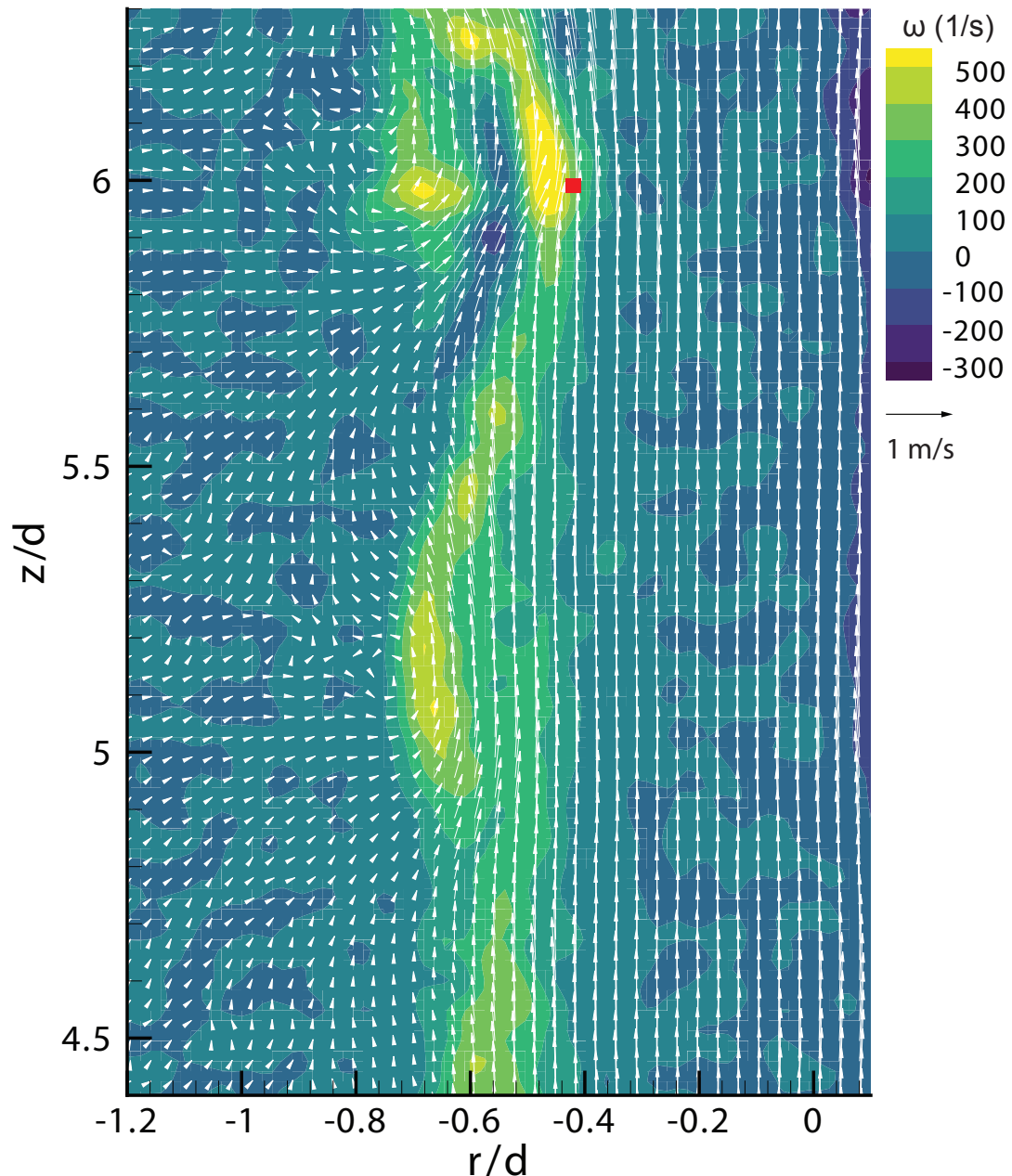
Figure 4.14: Single-phase jet velocity vector overlaid with the vorticity magnitude at $z/d = 4.4 - 6.3$. The primary peak location in the RMS velocity is shown by the square symbol. Vectors are diluted and rescaled for clarity.
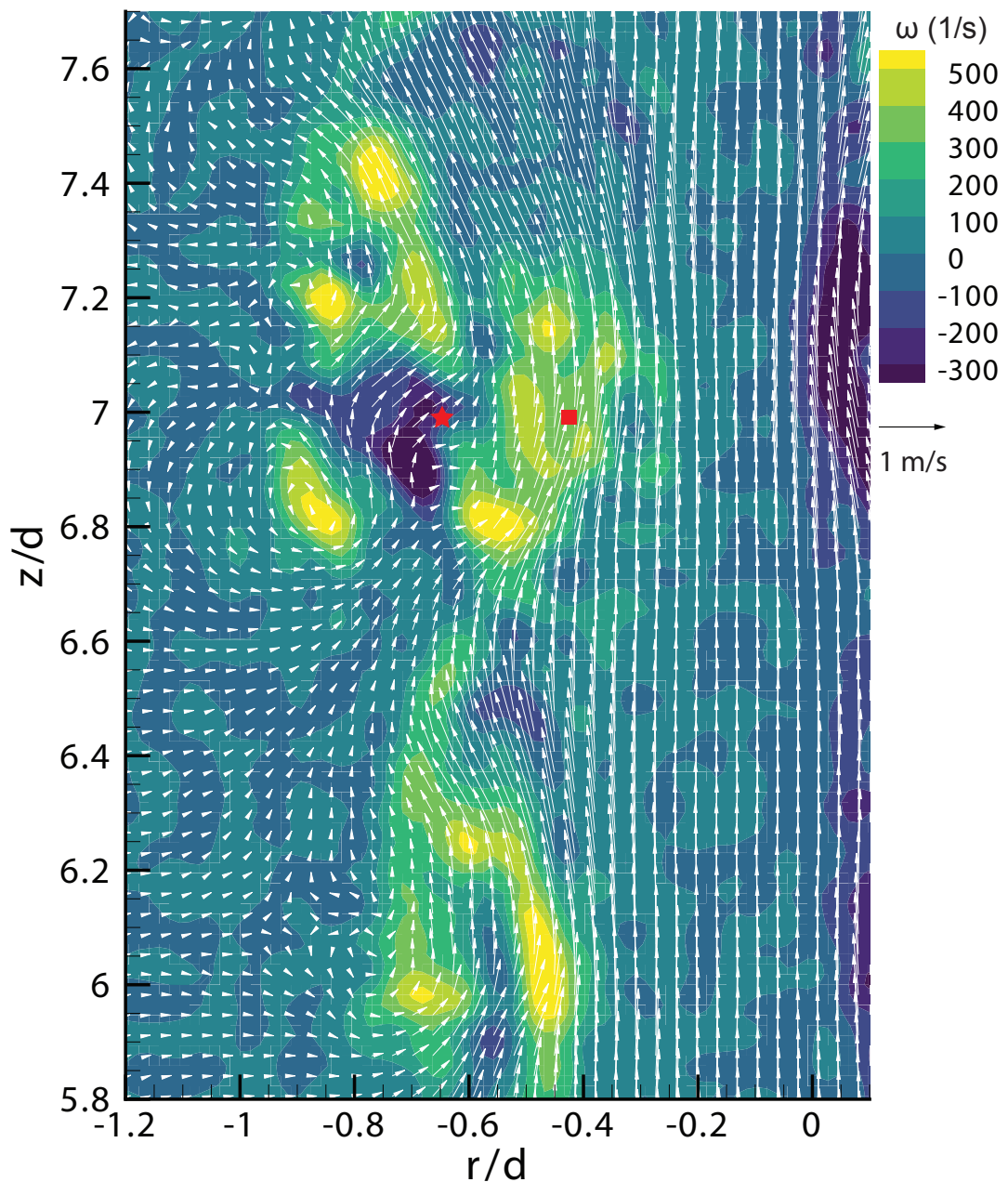
Figure 4.15: Single-phase jet velocity vector overlaid with the vorticity magnitude at $z/d = 5.7 - 7.8$. The primary peak location in the RMS velocity is shown by the square symbol. Vectors are diluted and rescaled for clarity.

phase nearly collapse. The difference between the phase velocity varies with radial location, peaking at 18% near the center, and being the smallest (11% of U_{cl}) at $r/b_{1/2} = \pm 0.75$. Presuming that the interaction between phases is associated with drag, the momentum transfer between phases should peak near the center. As the scaled magnitudes of the radial velocity of both phases increase at $z/d = 6$ and 7, the difference in their direction persists. The oil is dispersed outward, and its velocity increases with $r/b_{1/2}$ near the center, and then plateaus at $|r/b_{1/2}| > 1.2$. In contrast, the water is moving inward, and its velocity magnitude at $z/d = 6$ peaks at $r/b_{1/2} \approx \pm 0.5$. At $z/d = 7$, the peaks are less distinct and have lower magnitudes.

As most of the oil is already broken up into droplets by $z/d = 12.5$ and 13.5, its streamwise velocity remains higher than that of the water, but the difference between them (13% of U_{cl}) does not vary significantly in the radial direction. This velocity difference can be explained in terms of buoyancy effects as follows: The Sauter mean diameter of the droplet, D_{32}, is 8.7 mm by integrating the blob size distribution presented in figure 4.17. These oil patches are substantially larger than those measured further downstream under the same conditions, e.g., $D_{32} = 1.8$ mm at $z/d = 30.6$ (Xue and Katz, 2019), indicating that the breakup process is still ongoing. Following the discussions in Friedman and Katz, 2002 and Gopalan, Malkiel, and Katz, 2008, the corresponding rise velocity in quiescent flows is $U_q = 0.15$ m/s. In a turbulent flow with $\langle \widetilde{u'_z u'_z} \rangle^{1/2} / U_q \sim 2$, which corresponds to the present conditions, the mean rise velocity increases to 0.19 m/s. The latter is consistent with the measured average difference between the mean axial velocity of the
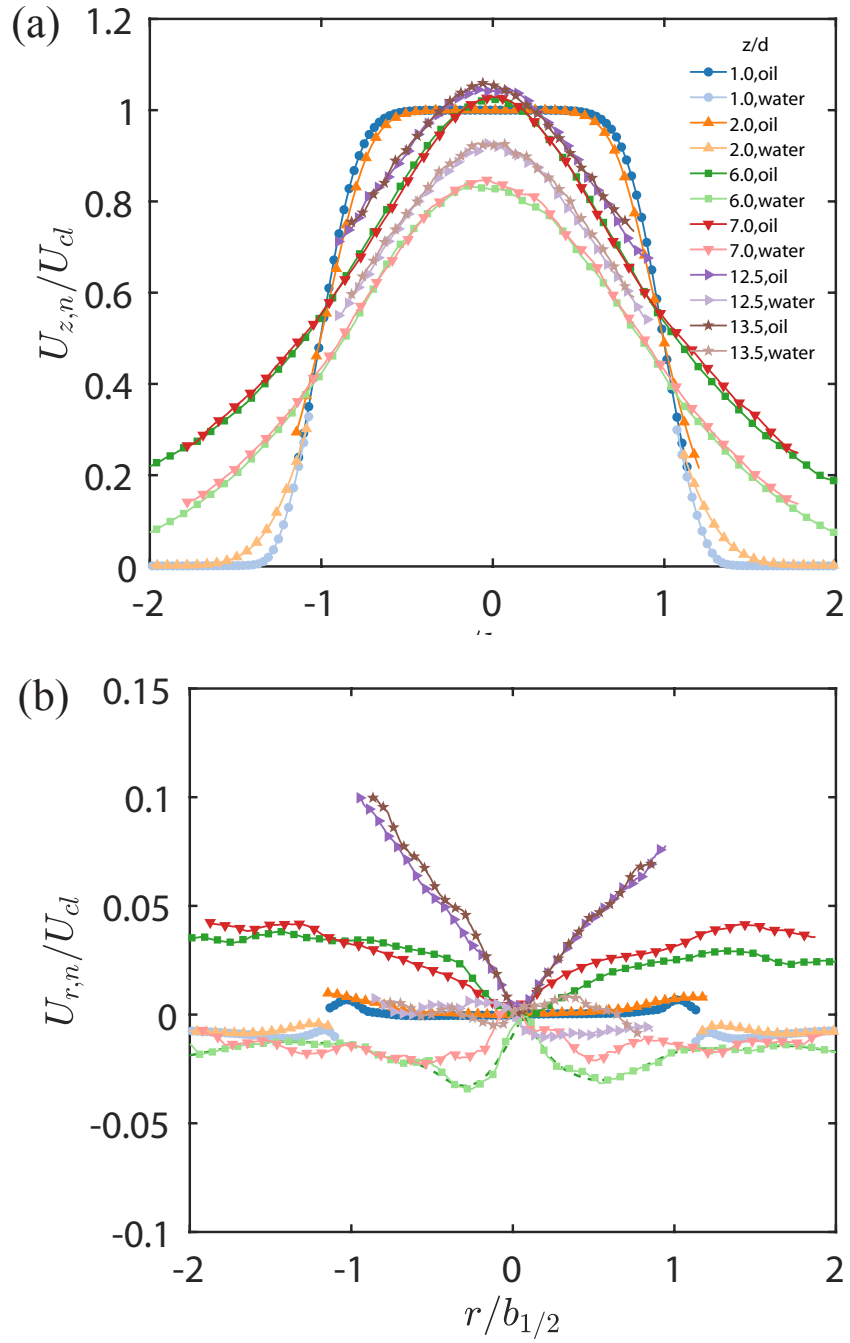
Figure 4.16: Radial profiles of (a) axial mean velocity and (b) radial mean velocity with different downstream location, conditioned on the local presence of oil phase or water phase. Dashed line show a spline fit of the water phase radial velocity.
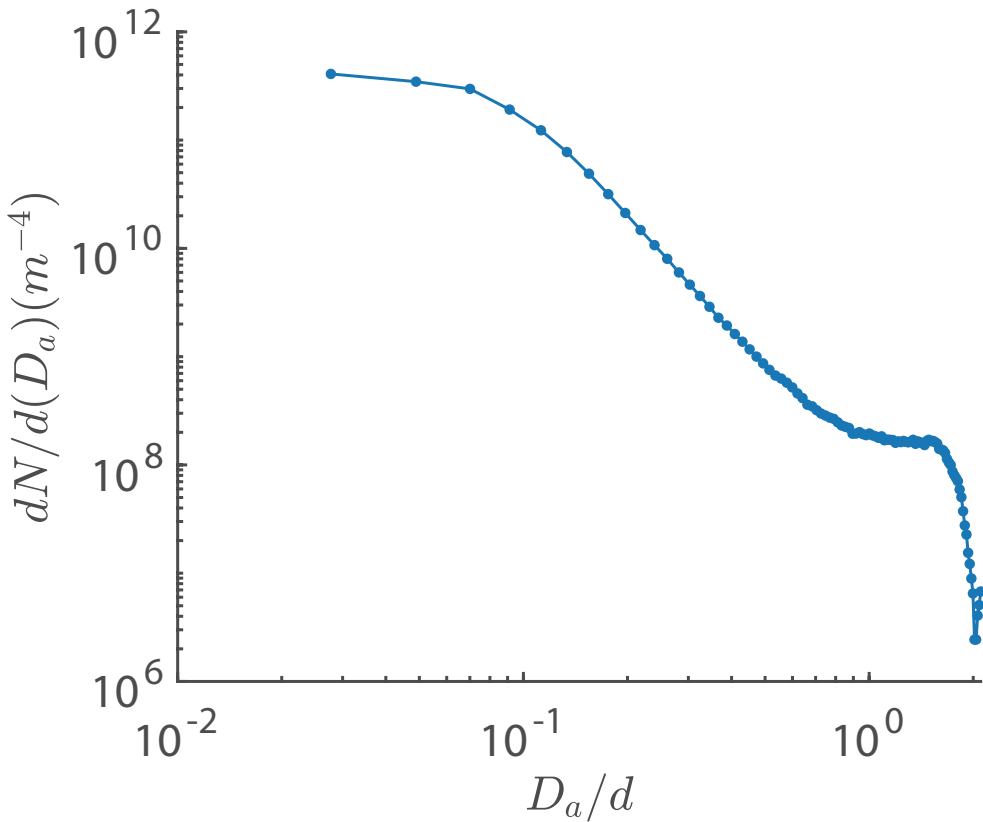
Figure 4.17: Number density distribution of oil blobs at $z/d = 11.8 - 13.8$.

two phases (0.20 m/s), i.e. this difference is driven by buoyancy and enhanced by turbulence.

Finally, at $z/d = 12.5$ and 13.5, the radial velocity of water, i.e., its entrainment rate diminishes as the water fraction reaches nearly 40% (figure 4.10a) near the jet centerline. While the scaled radial oil velocity is higher than those measured at lower z/d, its actual magnitude is lower. This radial oil outflux should be expected since the oil fraction and (absolute) axial velocity keep on decreasing in this region. In fact, the measured values of $\partial(\gamma U_{z,o})/\partial z$ matches that of $\partial(\gamma r U_{r,o})/r\partial r$ to within 15% (not shown), owing to combined effects of
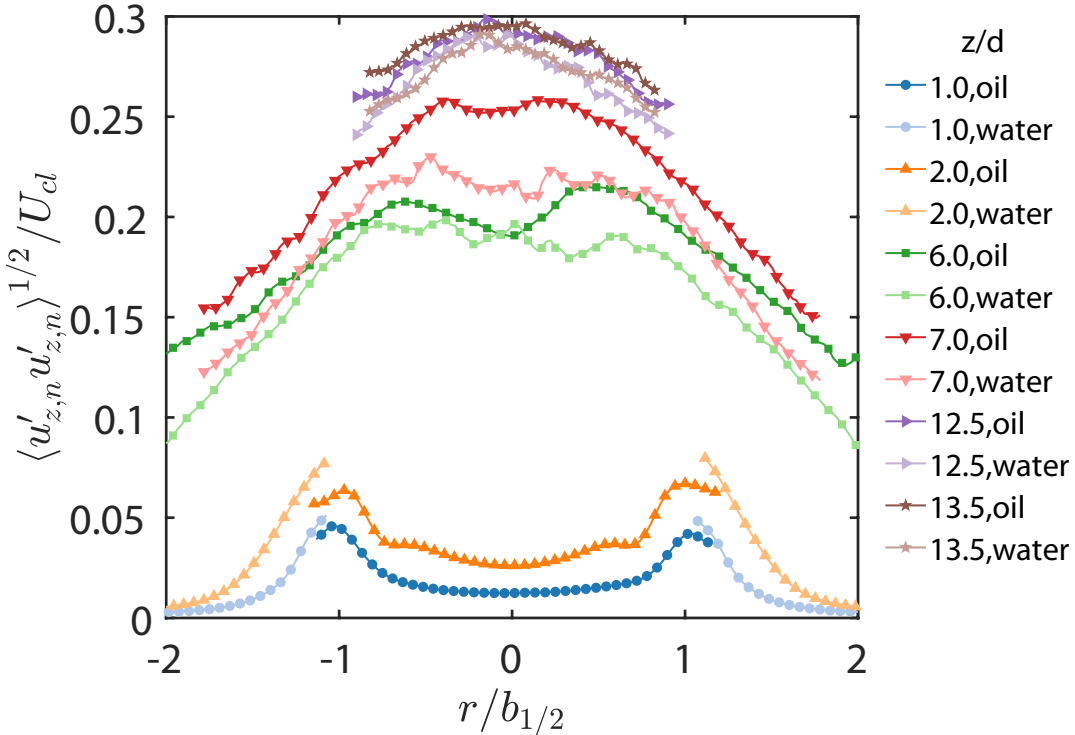
Figure 4.18: Radial profiles of the axial RMS velocity with different downstream location, conditioned on the local presence of oil phase or water phase.

uncertainty in velocity (radial component mostly) and volume fraction. The axial velocity of the water also decreases, but its fraction increases, resulting in a low radial influx.

The phase conditioned radial profiles of the normal, and shear Reynolds stresses are plotted in figures 4.18, 4.19, and 4.20. Here again, the jitter of the water data near the jet centerline at $z/d = 6 - 7$ is attributable to the limited fraction of water there. The differences between Reynolds stress components of oil and water vary with elevation. At $z/d = 1$ and 2, in the narrow overlap region, where the oil ligaments form and entrain water, $\langle u'_{z,w} u'_{z,w} \rangle^{1/2}$ and to a lesser extent $\langle u'_{z,w} u'_{r,w} \rangle$ of the water are slightly higher than those of the oil.
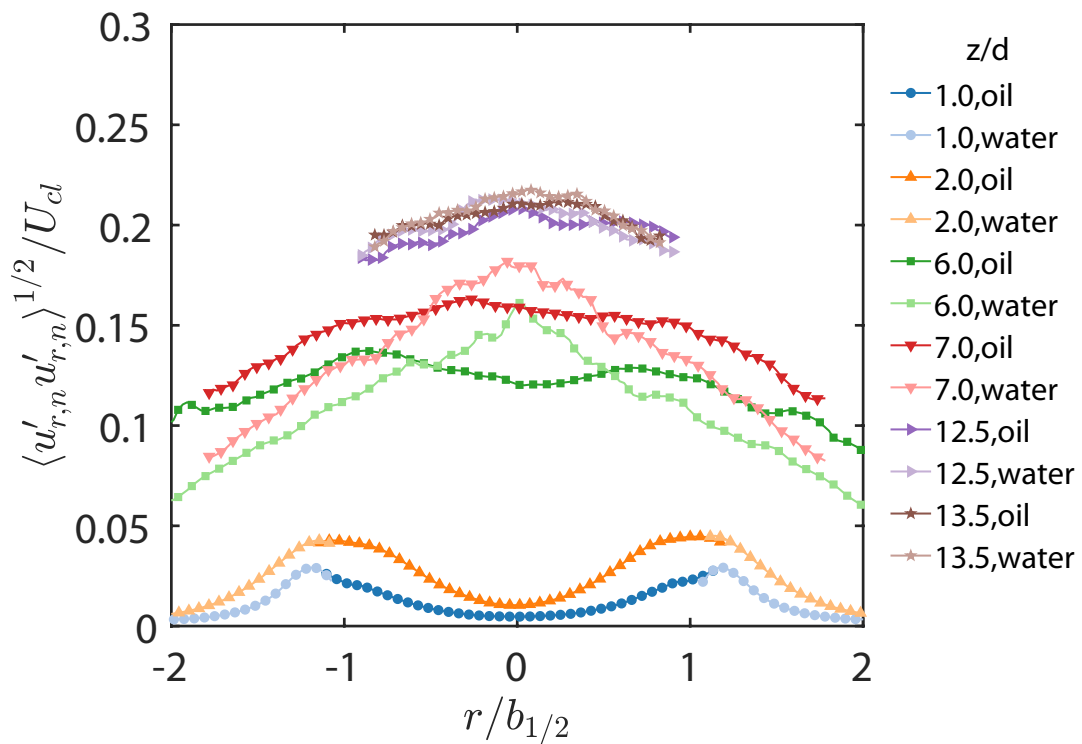
Figure 4.19: Radial profiles of the radial RMS velocity with different downstream location, conditioned on the local presence of oil phase or water phase.
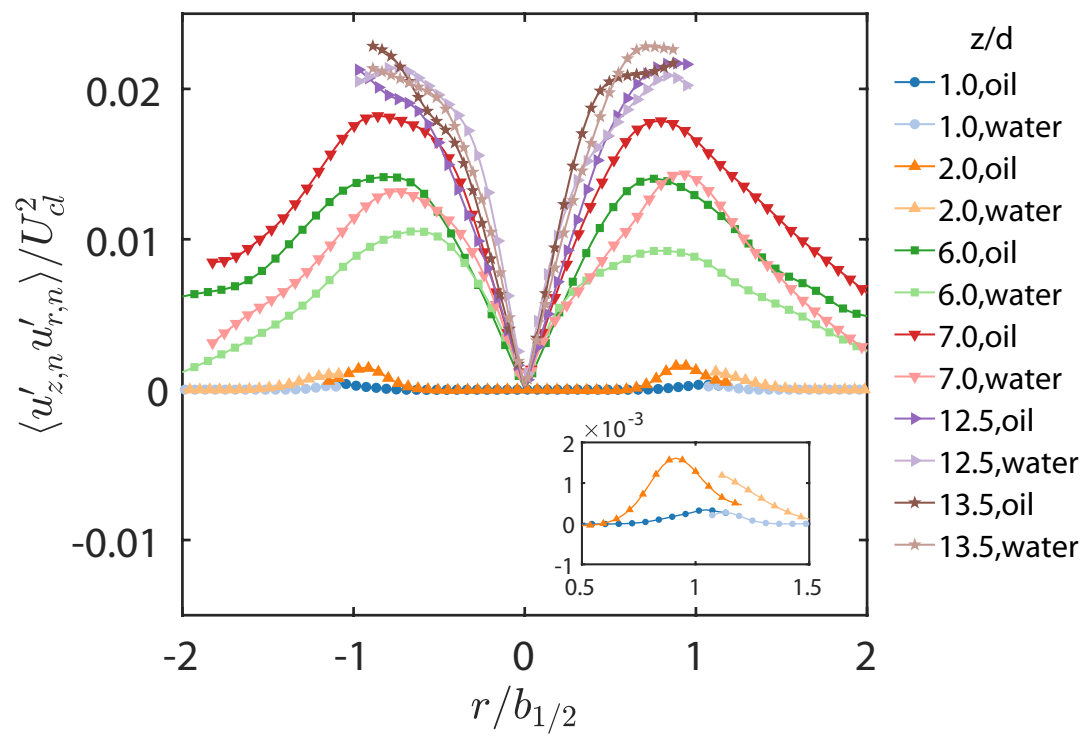
Figure 4.20: Radial profiles of the Reynolds shear stress with different downstream location, conditioned on the local presence of oil phase or water phase.

At $z/d = 1$, the radial velocity fluctuations peak in the water region where vortices form around the ligament tips, but the profiles of the oil and water almost collapse in the overlap region. At $z/d = 2$, it appears that the peaks in $\langle u'_{z,o} u'_{r,o} \rangle$ and $\langle u'_{z,w} u'_{r,w} \rangle$ do not coincide, indicating that the former is mostly contained in the azimuthal shear layer within the oil (figure 4.7), whereas the latter is centered in the ligament/water vortex region (figure 4.6). For these reasons, the combined stress (figure 4.13) has two humps. At $z/d = 6$ and 7, the trends are reversed, and the differences between the normal and shear stress in the water and the oil become significantly more substantial. The axial fluctuations and shear stresses in the oil are almost always higher than those of the water. In contrast, while the radial velocity fluctuations in the oil are higher along the jet periphery, those of the water are higher at the center. The following discussion will show that the latter trend can be attributed to the difference in the corresponding turbulence production rates. As the oil phase breaks up into droplets at $z/d = 12.5$ and 13.5, the differences between all the stress components in the oil and those in the water and near the center of the jet nearly diminish, and the distributions scaled using $b_{1/2}$ and U_{cl} for each phase appear to collapse.

The next discussion investigates the reason why the turbulence level in the oil is higher than that in the water along the jet periphery at $z/d = 6$ and 7. Potential buoyancy effects, such as variations in the rise velocity of droplets (and blobs) with size in regions where they are sparse, are examined first. Figure 4.21 and figure 4.22 presents the joint probability density function (p.d.f) of the oil blob equivalent diameter, D_e/d, and the axial and radial
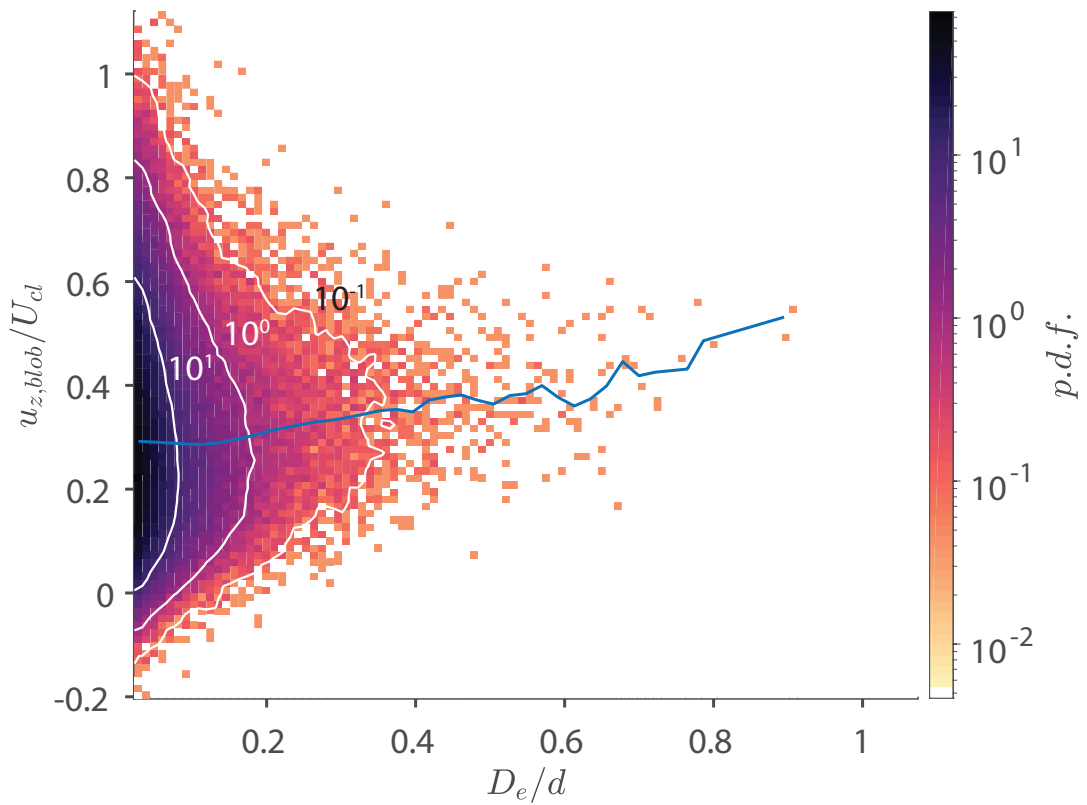
Figure 4.21: The probability distributions of the oil blob axial velocity at z/d=5.8-7.7. The blue lines shows the averaged velocity components for each diameter. Only the oil blobs which located outside the jet (radial location of the blob's center of mass larger than $b_{1/2}$) are included.
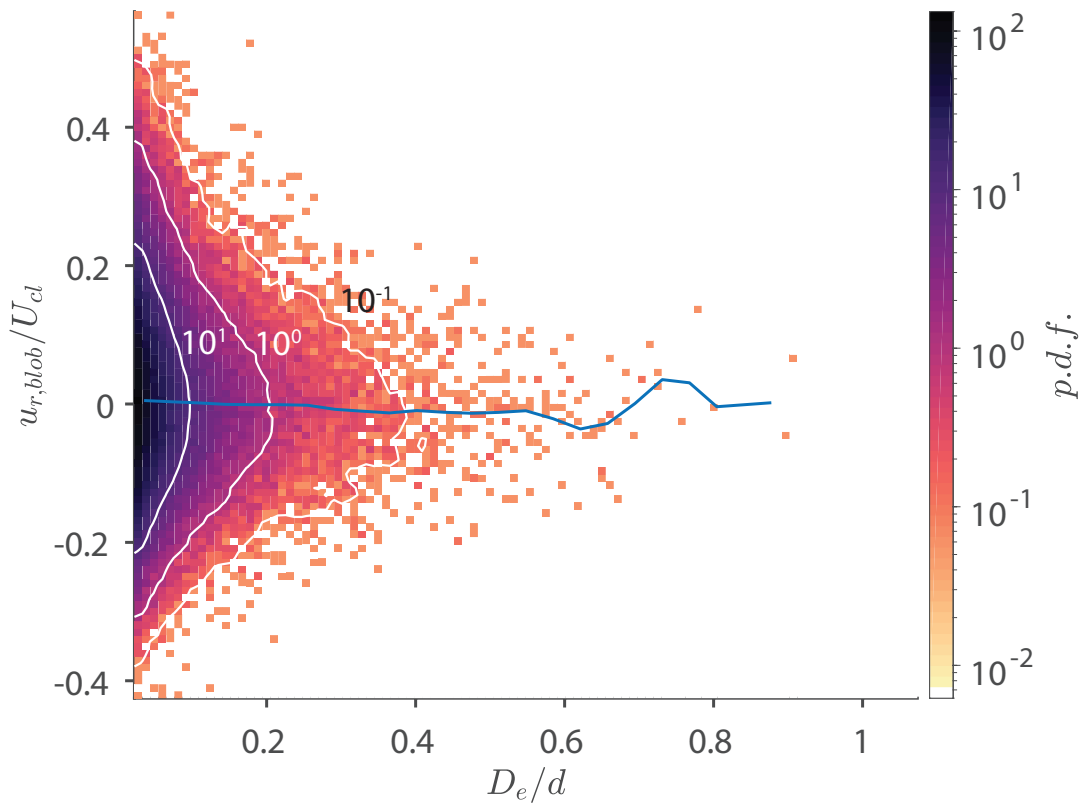
Figure 4.22: The probability distributions of the oil blob radial velocity at z/d=5.8-7.7. The blue lines shows the averaged velocity components for each diameter. Only the oil blobs which located outside the jet (radial location of the blob's center of mass larger than $b_{1/2}$) are included.

velocity components of the oil blobs, $u_{i,blob}/U_{cl}$. Here, D_e is defined as the diameter of a circle with the same area as the oil area cross section, regardless of whether it is compound or not, and $u_{i,blob}$ is calculated by spatially averaging all the instantaneous velocity vectors within this blob. Only oil patches with centers located at $r/b_{1/2} > 0$ are included. As is evident, while the blob population becomes broader and its concentration increases with decreasing D_e, the conditionally averaged values of $u_{z,blob}/U_{cl}$ increase with the oil blob diameter. The joint p.d.f of the radial velocity component scatters in a similar fashion, yet, the conditionally averaged distribution of $u_{r,blob}$ remains nearly zero across the entire size spectrum. The difference between the trends of the two velocity components indicates that there is a clear buoyancy effect on the axial velocity component of the oil. However, since the radial velocity is not dependent on size, yet the oil radial fluctuations are higher than those of the water, the difference is not associated with blob size. Furthermore, the variance in velocity (either component) for oil blobs of similar size is much larger (98%) than the variations with oil patch size. Hence, buoyancy is not the cause of the higher level of peripheral turbulence in the oil.

The next step examines the impact of turbulence intermittency, especially in the water, resulting from entrainment of low momentum water into the jet. Besides the oil-water interface, another distinct feature along the jet periphery is the presence of a turbulent/non-turbulent interface (TNTI) (Silva et al., 2014). Here, we use the normalized vorticity as a criterion for separating vortical (i.e., turbulent) regions from the surrounding irrotational flow, as suggested by Da Silva, Taveira, and Borrell, 2014. For free shear flows, including jets, the

94

recommended normalization for each elevation (z_0) is

$$|\omega|^+ (r, z_0, t) = \frac{|\omega|(r, z_0, t)}{max(\langle \omega'(r, z_0)\omega'(r, z_0)\rangle^{1/2})} \quad (4.8)$$

Here $|\omega| = (\omega_i\omega_i)^{1/2}$ is the instantaneous vorticity magnitude, and the denominator is the maximum RMS value of the vorticity along with the radial profile. In the present case, the analysis is performed based on the circumferential vorticity. Following Taveira et al., 2013, the threshold should be selected as the inflection point in the vorticity magnitude histogram for the entire sample volume. Based on the present data (not shown), $|\omega|^+ = 0.5$ has been selected as the threshold. Therefore, an additional step function, $I(r, z, t)$, is defined, whose value is unity for $|\omega|^+ > 0.5$ ("turbulent region") and zero where $|\omega|^+ < 0.5$. Partitioning the jet flow by combining the phase distribution and turbulent regions, four zones can be delineated: (i) turbulent & oil: $I(r, z, t)H(r, z, t) = 1$, (ii) non-turbulent & oil: $[1 - I(r, z, t)]H(r, z, t) = 1$, (iii) turbulent & water: $I(r, z, t)[1 - H(r, z, t)] = 1$, and (iv) non-turbulent & water: $[1 - I(r, z, t)][1 - H(r, z, t)] = 1$. The corresponding fractions for each zone can then be determined by ensemble-averaging. For example, for a turbulent zone containing oil:

$$\chi_{T,o} = \frac{1}{M} \sum_{p=1}^{M} I(r, z, t_p)H(r, z, t_p), \quad (4.9)$$

where M corresponds to the total number of samples at a given location, and the T represents the turbulence. The rest of the fractions are determined in the same manner.
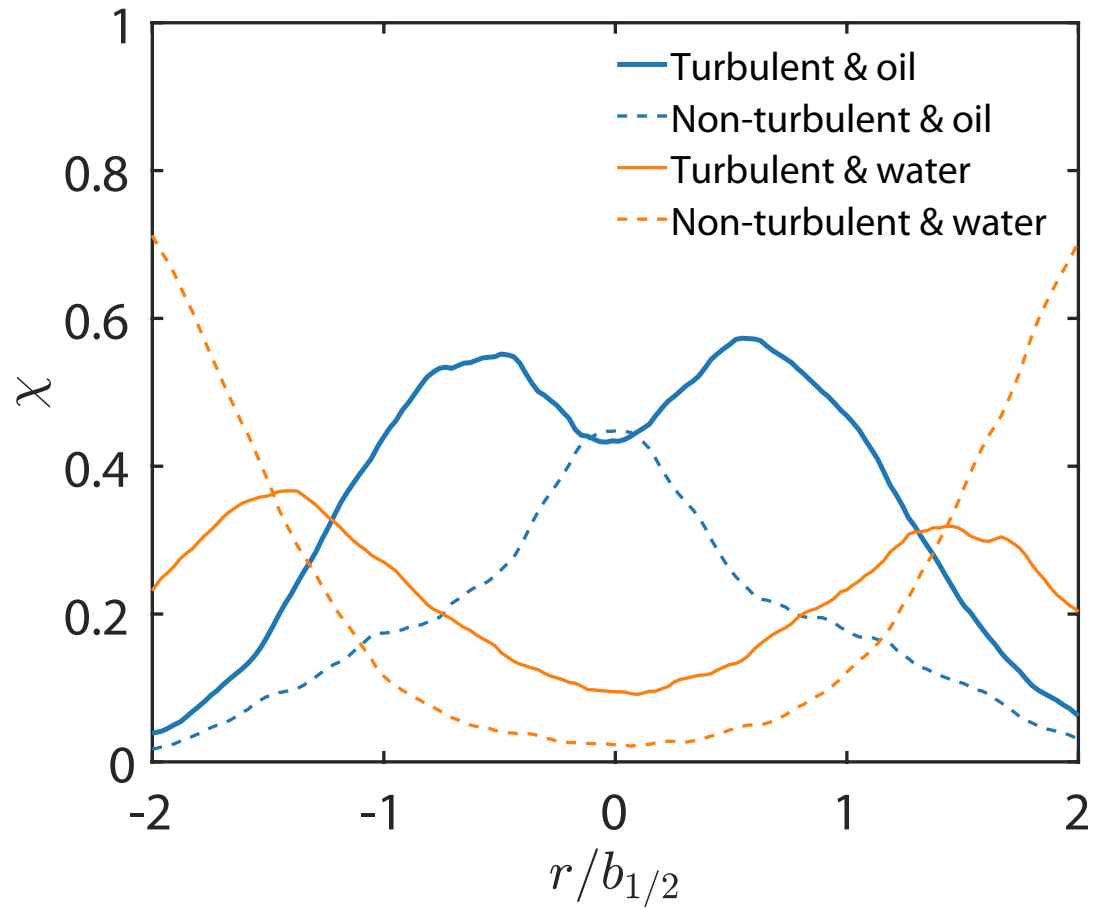
Figure 4.23: Radial profiles of the fraction budget of the turbulent/non-turbulent and oil/water phase zones at $z/d = 6$, blue: oil phase; orange: water phase; solid line: turbulent; dashed line: non-turbulent. The fractions add up to one for a given radial location.

Figure 4.23 shows the fraction budgets at $z/d = 6$. For the oil phase, the turbulent fraction peaks at $r/b_{1/2} = \pm 0.5$, at the same locations as the corresponding peaks in $\langle u'_{z,o} u'_{r,o} \rangle$ (Fig. 11a). The oil in the centerline is less turbulent. Here, $\chi_{T,o}$ is 0.43. slightly lower than the non-turbulence fraction (0.45). At $r/b_{1/2} > \pm 1$, both the turbulent and non-turbulent oil fractions diminish due to the decreasing oil fraction. For the water phase, the are turbulent peaks are centered around $r/b_{1/2} = \pm 1.4$, i.e., outward from those of the oil, and from the jet half-width. Near the centerline, the fraction of non-turbulent water is almost zero, but it increases rapidly at $r/b_{1/2} > 1.0$. Another convenient approach for examining the trends of intermittency is based on calculating the fraction of turbulent regions in each phase separately using

$$\xi_o = \frac{1}{\sum H} \sum_{p=1}^{M} I(r,z,t_p) H(r,z,t_p), \tag{4.10}$$

and

$$\xi_w = \frac{1}{M - \sum H} \sum_{p=1}^{M} I(r,z,t_p)[1 - H(r,z,t_p)] \tag{4.11}$$

The results, presented in figure 4.24, indicate that near the center of the jet, a little less than 50% of the oil is turbulent, but this fraction increases along the perimeter and remains high. In contrast, while the water blobs entrained into the center are mostly turbulent, the fraction of turbulent zones decreases rapidly with increasing r/d. Therefore, substantial fractions of ambient water penetrating into the jet are still not turbulent, resulting in lower axial and radial velocity fluctuations as well as shear stress along the periphery. However, while the turbulent fraction in the water is higher than that of the
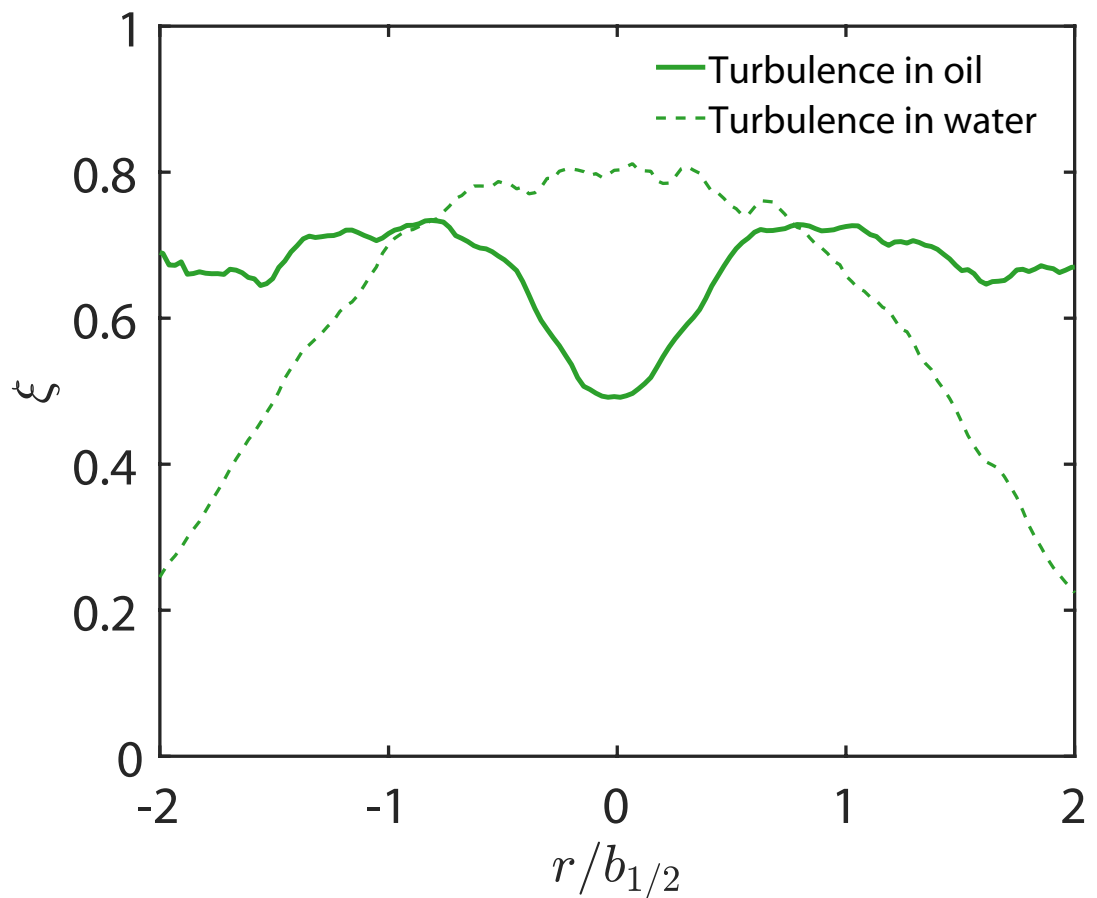
Figure 4.24: Radial profiles of the fraction of turbulent zones in oil phase (solid line) and turbulent zone in water phase (dashed line).

oil near the jet center, the oil streamwise velocity fluctuations (figure 4.18), which are the largest component, are still higher than those of the water. These conflicting trends imply that the amplitude of fluctuations in the turbulent oil fraction must be higher than those in the water. In contrast, the water radial velocity fluctuations near the jet center are higher than those in the oil (figure 4.19). While being consistent with the trends of turbulent fractions, the reason for the different trends among the components is not clear. The next section attempts to provide a plausible explanation for this discrepancy by examining the corresponding turbulent production rates. Before concluding this section, it should be noted that the differences between turbulence levels have also been measured in the periphery of the far field of miscible buoyancy-driven liquid plumes (Burridge et al., 2017). In that study, in the outer perimeter, the axial velocity fluctuations are higher in the dispersed phase, consistent with the present finding. However, further inward (but far from the center), the trends are reversed. The authors postulate that the latter trend is a result of differences in the turbulence production rate.

4.5   Turbulent kinetic energy production

This section investigates the production rates of the turbulent kinetic energy (TKE) and normal Reynolds stresses components as well as the flow phenomena affecting them. In multiphase flow containing n phases with volume fraction fractions, γ_n, the TKE production rate derived from the Reynolds averaged momentum equation and expressed in a cylindrical coordinate system

is

$$\widetilde{P} = -\sum_n \left(\langle u'_{r,n} u'_{r,n} \rangle \frac{\partial \gamma_n U_{r,n}}{\partial r} + \langle u'_{z,n} u'_{r,n} \rangle \left(\frac{\partial \gamma_n U_{r,n}}{\partial z} + \frac{\partial \gamma_n U_{z,n}}{\partial r} \right) + \right.$$
$$\left. \langle u'_{\theta,n} u'_{\theta,n} \rangle \frac{\gamma_n U_{r,n}}{r} + \langle u'_{z,n} u'_{z,n} \rangle \frac{\partial \gamma_n U_{z,n}}{\partial z} \right), \quad (4.12)$$

Since $\langle u'_{\theta,n} u'_{\theta,n} \rangle$ is not measured, in the following analysis, it is assumed to be equal to $\langle u'_{r,n} u'_{r,n} \rangle$, i.e., assuming axial symmetry and isotropy. Many previous measurements (Darisse, Lemay, and Benaïssa, 2015; Lai and Socolofsky, 2019; Panchapakesan and Lumley, 1993a; Panchapakesan and Lumley, 1993b) have shown that this assumption is reasonable for single-phase and buoyant jet. Using this assumption, the TKE and individual normal stress production rates of each phase are

$$P_n = -\left(\langle u'_{r,n} u'_{r,n} \rangle \frac{\partial \gamma_n U_{r,n}}{\partial r} + \langle u'_{z,n} u'_{r,n} \rangle \left(\frac{\partial \gamma_n U_{r,n}}{\partial z} + \frac{\partial \gamma_n U_{z,n}}{\partial r} \right) + \right.$$
$$\left. \langle u'_{r,n} u'_{r,n} \rangle \frac{\gamma_n U_{r,n}}{r} + \langle u'_{z,n} u'_{z,n} \rangle \frac{\partial \gamma_n U_{z,n}}{\partial z} \right), \quad (4.13)$$

$$P_{\langle u'_{r,n} u'_{r,n} \rangle} = -2 \left(\langle u'_{r,n} u'_{r,n} \rangle \frac{\partial U_{r,n}}{\partial r} + \langle u'_{z,n} u'_{r,n} \rangle \frac{\partial U_{r,n}}{\partial z} \right), \quad (4.14)$$

$$P_{\langle u'_{z,n} u'_{z,n} \rangle} = -2 \left(\langle u'_{z,n} u'_{r,n} \rangle \frac{\partial U_{z,n}}{\partial r} + \langle u'_{z,n} u'_{z,n} \rangle \frac{\partial U_{z,n}}{\partial z} \right), \quad (4.15)$$

$$P_{\langle u'_{\theta,n} u'_{\theta,n} \rangle} = -2 \langle u'_{\theta,n} u'_{\theta,n} \rangle \frac{U_{r,n}}{r}, \tag{4.16}$$

Since the calculations involve velocity gradients, which are sensitive to the jitter in the radial velocity distributions, their profiles are fitted with cubic smoothing splines, as illustrated in figure 4.16(b). For the azimuthal term near the jet centerline ($\langle u'_{r,n} u'_{r,n} \rangle U_{r,n}/r$), the singularity is removed using L'Hopital's rule. Figure 4.25 shows the radial profile of $\widetilde{P}$ and the terms contributing to it at $z/d = 6$. Here, data for both sides of the jet are combined. Evidently, the shear production term, $\langle u'_{z,n} u'_{r,n} \rangle (\partial U_{r,n}/\partial z + \partial U_{z,n}/\partial r)$, is the dominant contributor with a peak located near $r/b_{1/2} = 0.78$. While the axial term contributes to the centerline production, it becomes negative along the jet periphery. The radial and azimuthal components are both very small and negative near the center. The location of the total TKE production rate, $r/b_{1/2} = 0.67$ is not significantly different than that measured in the far field of single-phase jets (Lai and Socolofsky, 2019). While the present single-phase jet is still undergoing transition at $z/d = 6$, the peak TKE production of this jet at $z/d = 13.5$ is also located at a similar radius ($r/b_{1/2} = 0.61$).

The corresponding terms in each of the phases are compared in figure 4.26. As is evident, the shear and axial production rate in the oil are significantly higher than that in the water at all radial locations, especially near the corresponding peaks. There are also noticeable differences in the trends of the radial contraction ($\langle u'_{r,n} u'_{r,n} \rangle \partial U_{r,n}/\partial r$) and azimuthal terms ($\langle u'_{r,n} u'_{r,n} \rangle U_{r,n}/r$) near the center of the jet, with those of the oil being negative (but small), and those of the water being positive. The sign difference in radial production is

101
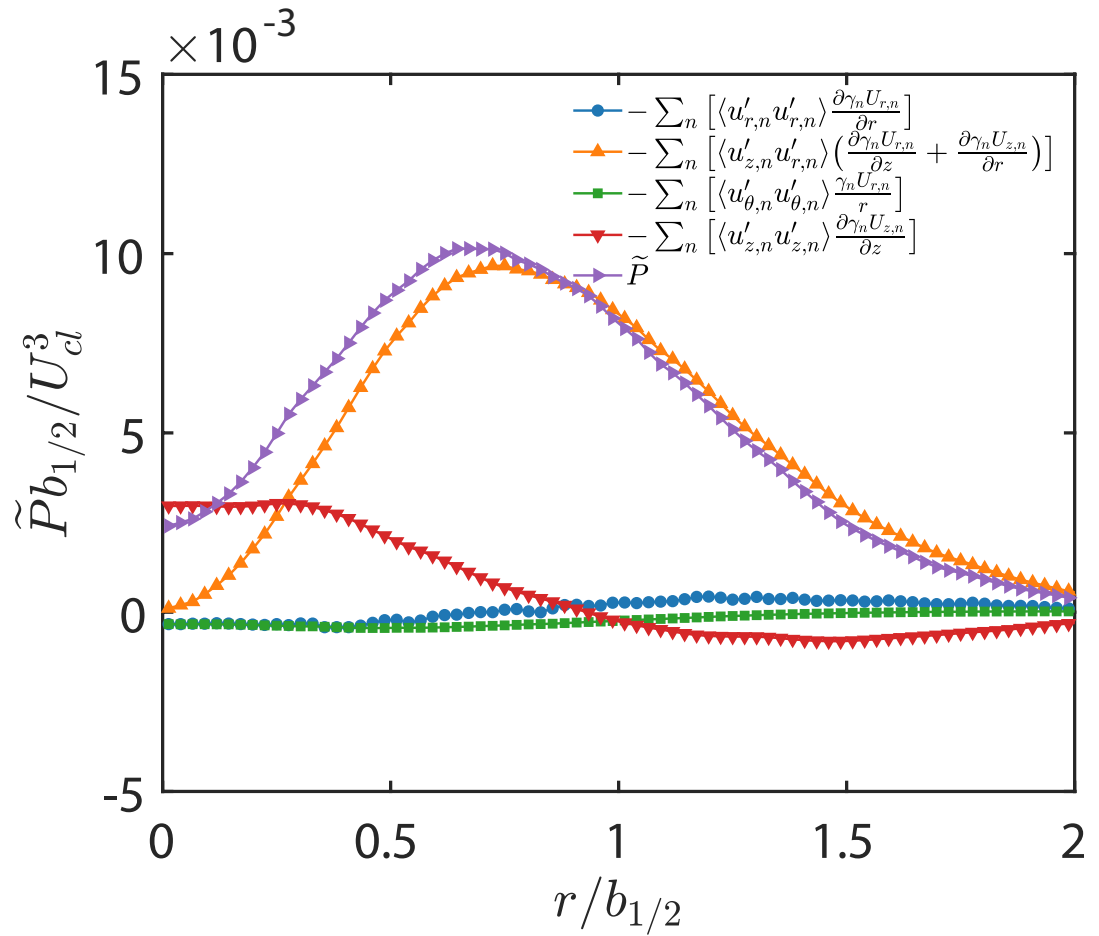
Figure 4.25: Radial profiles of the combined turbulent kinetic energy (TKE) production term and its components scaled with $U_{cl}^3/b_{1/2}$.

caused by the radial contraction of the water and the radial extension of the oil. The difference in azimuthal terms is associated with the direction of the radial velocity components (figure 4.19). Consequently, the distributions of oil and water TKE production rate near the center of the jet take very different forms, with that of the water being almost five times higher. Consequently, as shown in figure 4.27, the turbulent kinetic energy in the water, estimated using $k_n = (\langle u'_{z,n} u'_{z,n} \rangle + 2\langle u'_{r,n} u'_{r,n} \rangle)/2$, is higher than that of the oil near the jet centerline. It might also explain the higher fraction of turbulent regions in the water compared to those in the oil near the center. In contrast, along the jet perimeter, the oil turbulence is higher, also consistent with the distribution of production rate. These observations imply that in addition to the previously discussed effects of intermittency, the lower turbulence level in the water along the periphery is also affected by the lower production rate there.

Finally, it would also be interesting to compare the production rates of specific normal Reynolds stress components. The results, summarized in figure 4.28, demonstrate that while $P_{\langle u'_{z,n} u'_{z,n} \rangle}$ of the oil is higher than that of the water along the entire jet radius, $P_{\langle u'_{r,n} u'_{r,n} \rangle}$ and $P_{\langle u'_{\theta,n} u'_{\theta,n} \rangle}$ of the water are positive, and those of the oil are negative in the vicinity of the jet centerline. These trends are consistent with those of the axial and radial velocity fluctuations as well as the turbulent fractions in each phase. For example, at $z/d = 6$, $\langle u'_{r,o} u'_{r,o} \rangle$ is almost equal to $\langle u'_{r,w} u'_{r,w} \rangle$ and $\langle u'_{r,o} u'_{r,o} \rangle < \langle u'_{r,w} u'_{r,w} \rangle$ near the centerline. Furthermore, $\langle u'_{z,o} u'_{z,o} \rangle$ is significantly higher than $\langle u'_{r,o} u'_{r,o} \rangle$ along the entire radius, with the difference reaching 58% along the centerline. Also, $\langle u'_{r,w} u'_{r,w} \rangle$ has a sharp peak near the center, wheres $\langle u'_{r,o} u'_{r,o} \rangle$ has a broad
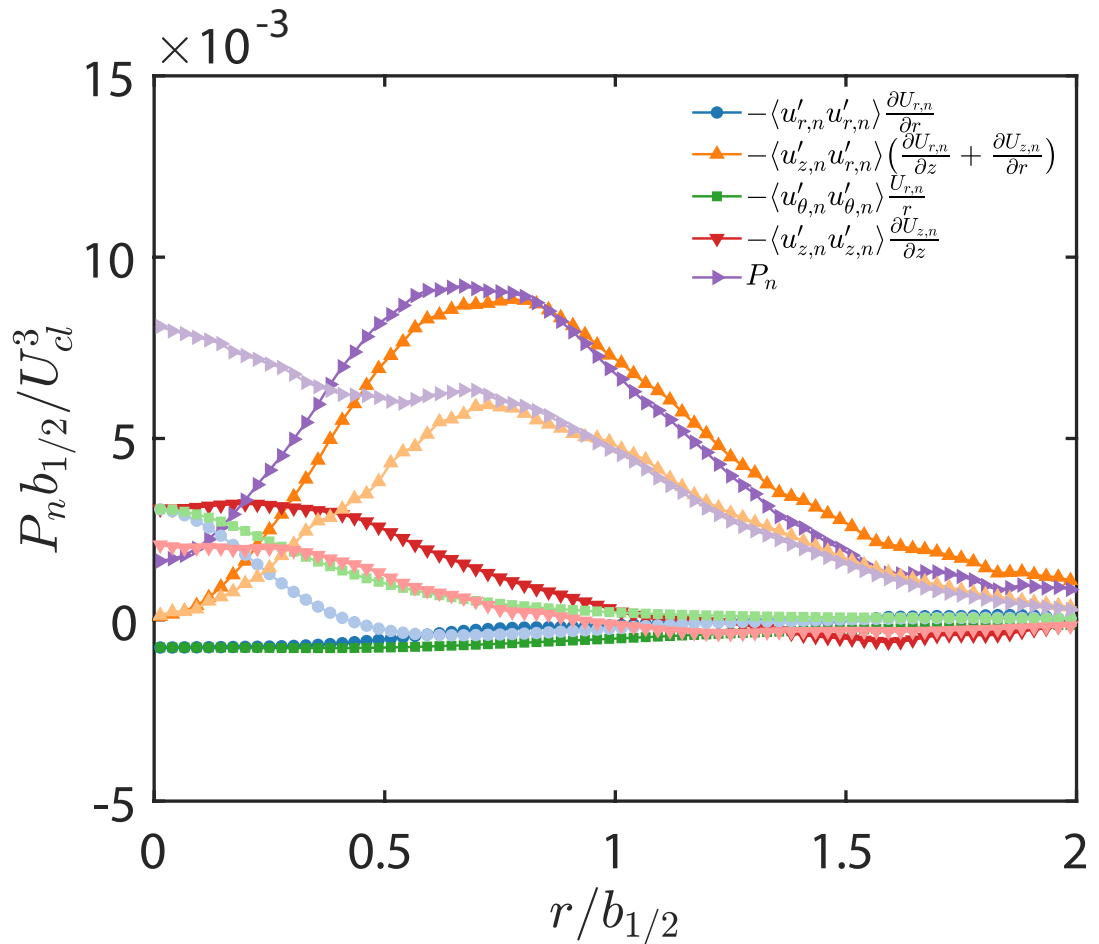
Figure 4.26: Radial profiles of the turbulent kinetic energy production term of each phase and its components at $z/d = 6$ scaled with $U_{cl}^3/b_{1/2}$.
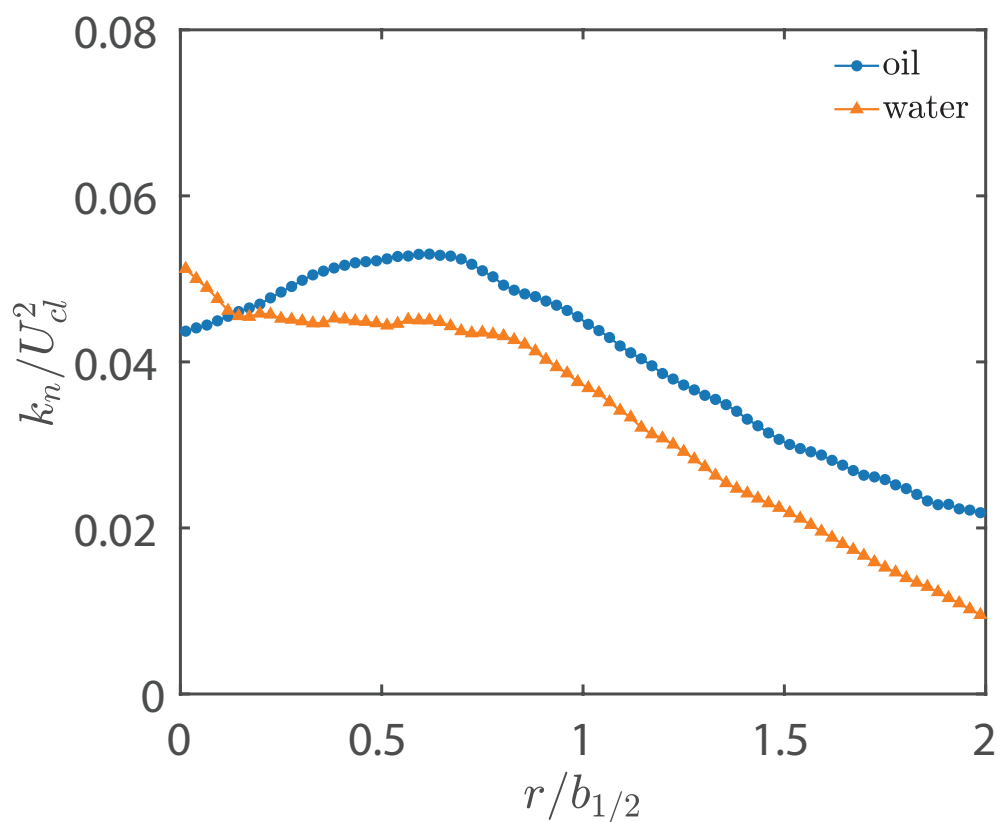
Figure 4.27: Radial profiles of the turbulent kinetic energy of each phase at $z/d = 6$.
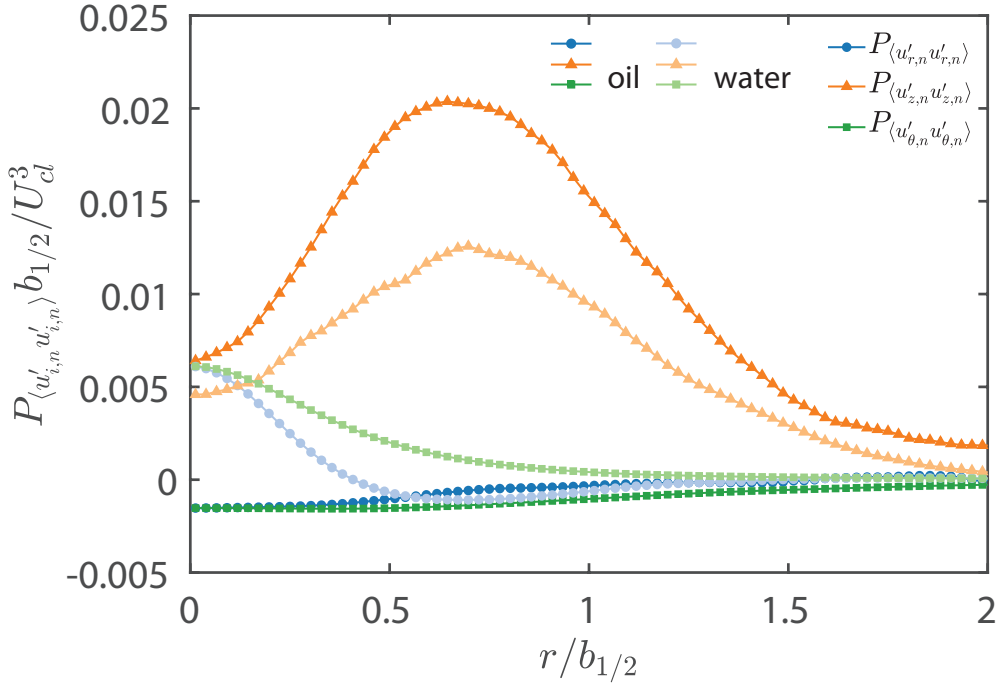
Figure 4.28: Radial profiles of the normal Reynolds stress production term for each phase at $z/d = 6$. Both are normalized by $U_{cl}^3/b_{1/2}$. solid line: oil phase, fade line: water phase.

distribution, both consistent with the trends of the corresponding production rates.

4.6 Summary

This chapter examines the flow structure, and turbulence in the near field of an immiscible buoyant oil jet injected into quiescent water at a moderate Reynolds number. Velocity and phase distribution measurements are performed simultaneously by applying particle image velocimetry, and planar

laser-induced fluorescence in a refractive index matched setup involving silicone oil and sugar water. These fluids have similar viscosity and density ratios, as well as the interfacial tension with those of the crude oil and seawater. The results include distributions of the phase, number density of the droplet diameter, and profiles of the mean velocity, RMS values of the axial and radial velocity fluctuations as well as Reynolds shear stress. Data analysis examines the mean flow and turbulence structures in both phases separately and combined. Trends are compared to those of a single-phase jet at the same Reynolds number. The discussion attempt to elucidate causes for differences in the evolution of turbulent quantities between the oil and single-phase jets, the water and the oil in the immiscible jet, and among the normal Reynolds stress components.

Chapter 5

Discussions and Conclusions

Immiscible turbulent jet and plume are investigated for both crude oil jet in seawater, and a surrogate fluid setup. The behavior of an oil jet transitioning into a plume in a crossflow at high-velocity ratios are elucidated by high-speed imaging. Custom-built *in situ* digital inline holography is applied to measure the size distribution of crude oil droplets. The effects of dispersant concentration on the size spectrum are presented. Experimental techniques capable of yielding simultaneous and measurements of both the carrier and dispersed phase in an immiscible turbulent flow is developed. The phase-dependent turbulent statistics are investigated in a vertical buoyant silicone oil jet injected into quiescent sugar water. These fluids have similar viscosity and density ratios, as well as the interfacial tension with those of the crude oil and seawater. By refractive index matching both fluids, simultaneous Particle Image Velocimetry (PIV) and Planar Laser-Induced Fluorescence (PLIF) are performed to measure the velocity and phase distributions. Machine

learning-based data analysis techniques are applied to obtain droplet size distributions from the PLIF images. Compound droplets containing multiple water droplets, some with smaller oil droplets, regularly form at moderate and high jet Reynolds number, but rarely in low Reynolds number. The origin of some of the encapsulated water droplets is elucidated. The interfacial area increase, volume fraction change, and droplet deformation caused by such phenomena are quantified. In the near field fragmentation region at a moderate Reynolds number, the mean flow and turbulence structures in both phases are investigated separately and combined. Comparison to a single-phase jet at the same Re are performed. The phase-dependent turbulence reveals significant differences in velocity and all Reynolds stress components. Analyses provide plausible explanations of the differences in the evolution of turbulent quantities between the oil and single-phase jets, the water and the oil in the immiscible jet, and among the normal Reynolds stress components.

Droplet sizing procedures are developed for the submerged holography measurements. It includes high-pass filtering of the reconstructed field to separate the analysis for small and large droplets. To detect the sizes and locations of the small droplets, blob analysis, and minimum depth method are applied. For large droplets, a modified Hough transform is implemented using a series of criteria involving image features around the droplet edge, including gradient edge detection. The time evolution of the droplet size distributions for the crude, 1:100 DOR, and 1:25 DOR plumes in crossflow obtained from holography measurements are compared. As expected, the characteristic droplet size dramatically decreases with increasing dispersant

concentration. The rate of decrease for the crude and 1:100 DOR cases are significant but different. A transition to a mild rate is observed at a latter time, corresponding to the bottom region of the plume. The size of droplets retained by the plume for both cases converges with that of the 1:25 DOR case. The overall trajectory of the plume is affected by the dispersant concentration and the corresponding droplet sizes. Large droplets are separated from the upper boundary of the plume due to their higher rise velocity in the crude oil plume, causing a difference in the plume trajectory in the upper edge. The number of droplets entrained by secondary vortex structures under the plume increases with dispersant concentration. The lower boundary of the crude and 1:100 DOR plumes appear to coincide and are, for the most part, higher than that of the 1:25 DOR plume.

To elucidate the flow phenomena occurring during the early stages of the breakup, refractive index matching of a surrogate fluid pair and high-speed PLIF are used to overcome the experimental challenge of resolving a high volume of fraction dispersed oil in water due to optical opacity. Although it rarely happens at $Re = 594$ ($We = 785$), compound droplets form regularly at $Re = 1358$ and $Re = 2122$ and persist at least up to $z/d = 30.6$. The origin of some of the water pockets can be traced back to the engulfment of water ligaments during the roll-up of the K-H vortices near the exit from the jet. In contrast, long thin water ligaments rarely form at $Re = 594$ before the oil breaks up, suggesting that for the present $Oh = 0.047$, the near field shear is not strong enough to generate such ligaments. For the present range, the fraction of compound droplets does not show significant Reynolds number

dependence, but a strong trend of increase that seems scaled with D^2. The small droplets are less likely to be compound, and the number density of large droplets diminishes as the Reynolds number increase, resulting the size distributions of compound droplets have peaks that increase in magnitude but shift to lower diameter with increasing Re. Although the buoyancy reduction is small due to such compound droplets, the interfacial area increase is approximately 15%. While the increased surface area could presumably enhance the dissolution rate of soluble components of oil into the water, the relationship between the enlarged interfacial area and mass diffusion may not be assumed to be simply linear. The turbulence level difference between the interior and the external flow, as well as the balance of soluble oil compounds concentration across the inner and outer oil-water interface, should be considered. Interestingly the interior droplets remain nearly spherical while the outer droplet deforms significantly in the high shear region. Presumably, the higher oil viscosity and the small size of the interior droplet reduce the deformation, create an environment with a low local capillary number.

To provide insights for the dynamics that arise within the immiscible buoyant jet during the fragmentation, we combine the phase distribution data obtained from the refractive index-matched PLIF data to the measurements of the velocity field. In the azimuthal shear layer developing close to the nozzle exit, while some vertical momentum of the water is obtained by shear, significant gain occurs as thin water layers are entrained into the jet, while oil ligaments start to extend outward. Kevin-Helmholtz vortices form in the water, with their centers located at the tip of the extended oil ligaments.

Further downstream, as the oil fragments to large blobs and subsequently to droplets, while entraining water, the axial momentum and oil-containing domain expand, concurrently with a reduction in the centerline oil fraction and velocity. The spreading rate of the oil volume fraction and the decrease in its centerline concentration are lower than those of the axial momentum and centerline velocity. What appears to be universal profiles of either the phase distribution or the axial momentum that could be scaled with the half widths and centerline values develop at $z/d = 6$. In the single-phase jet, the transition from an azimuthal shear layer to a self-similar profile of velocity occurs further downstream. The mean axial velocity of the oil is always higher than that of the water, as expected for a buoyant jet. At $z/d \geq 12.5$, where the scaled profiles collapse, the difference between the axial velocities of the phases is consistent with the buoyant rise velocity of oil droplets with the same Sauter mean diameter in turbulent flows. The radial fluxes of the oil and water have opposite signs as the oil expands, and the water is entrained inward. The turbulence level and shear stress in the oil jet are higher than those in the single-phase jet, but this difference decreases with increasing z/d. There are also significant disparities between the magnitude and trends of velocity fluctuations and shear stress between the two phases of the immiscible jet. Close to the nozzle, the velocity fluctuations and shear stress in the water are higher than those in the oil along the narrow phase-overlap region along the periphery of the jet. Consequently, the combined Reynolds stress profile has two peripheral humps, one corresponding to the shear layer within the oil, and an outer one in the region containing predominantly water.

At $z/d = 6$, where the oil velocity fluctuations still have broad peak off the jet center, along the jet periphery, all the turbulent quantities are higher in the oil. Near the jet center, the water radial velocity fluctuations have a sharp peak with a magnitude that is higher than the corresponding levels in the oil. Several potential contributors are evaluated in attempts to explain the different trends. The higher oil turbulence along the jet periphery cannot be caused by size-dependent differences in the buoyant rise velocity of the oil blobs. However, it appears to be affected by turbulence intermittency in the water as quiescent outer fluid is entrained into the jet, as well as by higher shear-dominated turbulence production rate in the oil. In contrast, near the jet center, the TKE production rate in the water is significantly higher than that in the oil. This latter trend is associated with radial contraction and inward flow of the water, which increase the turbulence production, as opposed to the radial extension of the oil, which decreases it.

Thirteen diameters downstream of the nozzle, where most of the oil is already fragmented into large droplets/blobs, the differences between oil and water turbulence levels diminish, and the scaled profiles of the normal and shear stresses in each phase nearly collapse. Still, the axial velocity fluctuations are substantially higher than the radial ones. The droplet size distributions measured under very similar conditions at z/d=30.6 have a Sauter mean diameter that is four times smaller than those at z/d=13, indicating the fragmentation of the oil persists well beyond the range examined in this paper. The relationship between this persistent fragmentation process and the evolution of the turbulence in the jet is deferred to future studies.

113

Other interesting topics include: (i) the integration of suitable machine learning frameworks to improve the holography droplet sizing and tracking procedures including the robustness of the threshold criteria, the resolution, as well as the accuracy of the depth location; (ii) the effects of dispersant concentration on the formation of compound droplets; (iii) the stability and long term impact of the soluble compounds associated with the inner droplets; and (iv) the mechanisms of turbulent modulation and their parametric dependence of the multiphase flow.

Bibliography

Machicoane, Nathanael, Julie K Bothell, Danyu Li, Timothy B Morgan, Theodore J Heindel, Alan L Kastengren, and Alberto Aliseda (2019). "Synchrotron radiography characterization of the liquid core dynamics in a canonical two-fluid coaxial atomizer". In: *International Journal of Multiphase Flow* 115, pp. 1–8.

Mittal, Rajat, Rui Ni, and Jung-Hee Seo (2020). "The flow physics of COVID-19". In: *Journal of fluid Mechanics* 894.

Woods, Andrew W (2010). "Turbulent plumes in nature". In: *Annual Review of Fluid Mechanics* 42, pp. 391–412.

Gros, Jonas, Scott A Socolofsky, Anusha L Dissanayake, Inok Jun, Lin Zhao, Michel C Boufadel, Christopher M Reddy, and J Samuel Arey (2017). "Petroleum dynamics in the sea and influence of subsea dispersant injection during Deepwater Horizon". In: *Proceedings of the National Academy of Sciences* 114.38, pp. 10065–10070.

Johansen, Øistein, Per Johan Brandvik, and Umer Farooq (2013). "Droplet breakup in subsea oil releases–Part 2: Predictions of droplet size distributions with and without injection of chemical dispersants". In: *Marine Pollution Bulletin* 73.1, pp. 327–335.

Zhao, Lin, Franklin Shaffer, Brian Robinson, Thomas King, Christopher D'Ambrose, Zhong Pan, Feng Gao, Richard S Miller, Robyn N Conmy, and Michel C Boufadel (2016). "Underwater oil jet: Hydrodynamics and droplet size distribution". In: *Chemical Engineering Journal* 299, pp. 292–303.

Zheng, Li, Poojitha D Yapa, and Fanghui Chen (2003). "A model for simulating deepwater oil and gas blowouts-Part I: Theory and model formulation". In: *Journal of hydraulic research* 41.4, pp. 339–351.

Charonko, John J and Katherine Prestridge (2017). "Variable-density mixing in turbulent jets with coflow". In: *Journal of Fluid Mechanics* 825, pp. 887–921.

Darisse, Alexis, Jean Lemay, and Azemi Benaïssa (2015). "Budgets of turbulent kinetic energy, Reynolds stresses, variance of temperature fluctuations and turbulent heat fluxes in a round jet". In: *Journal of Fluid Mechanics* 774, pp. 95–142.

Dowling, David R and Paul E Dimotakis (1990). "Similarity of the concentration field of gas-phase turbulent jets". In: *Journal of Fluid Mechanics* 218, pp. 109–141.

Ezzamel, Adam, Pietro Salizzoni, and Gary R Hunt (2015). "Dynamical variability of axisymmetric buoyant plumes". In: *Journal of Fluid Mechanics* 765, pp. 576–611.

Hussein, Hussein J, Steven P Capp, and William K George (1994). "Velocity measurements in a high-Reynolds-number, momentum-conserving, axisymmetric, turbulent jet". In: *Journal of Fluid Mechanics* 258, pp. 31–75.

Panchapakesan, Nagangudy R and John L Lumley (1993a). "Turbulence measurements in axisymmetric jets of air and helium. Part 1. Air jet". In: *Journal of Fluid Mechanics* 246, pp. 197–223.

Wang, Hongwei and Adrian Wing-keung Law (2002). "Second-order integral model for a round turbulent buoyant jet". In: *Journal of Fluid Mechanics* 459, pp. 397–428.

Mychkovsky, Alexander G and Steven L Ceccio (2012). "LDV measurements and analysis of gas and particulate phase velocity profiles in a vertical jet plume in a 2D bubbling fluidized bed Part II: Mass and momentum transport". In: *Powder technology* 220, pp. 47–54.

Stebe, KJ and D Barthes-Biesel (1995). "Marangoni effects of adsorption—desorption controlled surfactants on the leading end of an infinitely long bubble in a capillary". In: *Journal of Fluid Mechanics* 286, pp. 25–48.

Wegener, M, J Grünig, J Stüber, AR Paschedag, and M Kraume (2007). "Transient rise velocity and mass transfer of a single drop with interfacial instabilities–experimental investigations". In: *Chemical Engineering Science* 62.11, pp. 2967–2978.

Balachandar, S and John K Eaton (2010). "Turbulent dispersed multiphase flow". In: *Annual review of fluid mechanics* 42, pp. 111–133.

Lin, SP and RD Reitz (1998). "Drop and spray formation from a liquid jet". In: *Annual review of fluid mechanics* 30.1, pp. 85–105.

Villermaux, Emmanuel (2007). "Fragmentation". In: *Annu. Rev. Fluid Mech.* 39, pp. 419–446.

Aliseda, Alberto, Emil J Hopfinger, Juan C Lasheras, DM Kremer, A Berchielli, and EK Connolly (2008). "Atomization of viscous and non-Newtonian liquids by a coaxial, high-speed gas jet. Experiments and droplet size modeling". In: *International Journal of Multiphase Flow* 34.2, pp. 161–175.

Desjardins, Olivier, Jeremy McCaslin, Mark Owkes, and Peter Brady (2013). "Direct numerical and large-eddy simulation of primary atomization in complex geometries". In: *Atomization and Sprays* 23.11.

Gorokhovski, Mikhael and Marcus Herrmann (2008). "Modeling primary atomization". In: *Annu. Rev. Fluid Mech.* 40, pp. 343–366.

Lasheras, Juan C and EJ Hopfinger (2000). "Liquid jet instability and atomization in a coaxial gas stream". In: *Annual review of fluid mechanics* 32.1, pp. 275–308.

Jarrahbashi, D, WA Sirignano, PP Popov, and Fazle Hussain (2016). "Early spray development at high gas density: hole, ligament and bridge formations". In: *Journal of Fluid Mechanics* 792, pp. 186–231.

Marmottant, Philippe and Emmanuel Villermaux (2004). "On spray formation". In: *Journal of fluid mechanics* 498, pp. 73–111.

Shinjo, J and A Umemura (2010). "Simulation of liquid jet primary breakup: Dynamics of ligament and droplet formation". In: *International Journal of Multiphase Flow* 36.7, pp. 513–532.

Lowe, Albyn, Agisilaos Kourmatzis, and Assaad R Masri (2017). "Turbulent spray flames of intermediate density: Stability and near-field structure". In: *Combustion and Flame* 176, pp. 511–520.

Brandvik, Per Johan, Øistein Johansen, Frode Leirvik, Daniel F Krause, and Per S Daling (2018). "Subsea dispersants injection (SSDI), effectiveness of different dispersant injection techniques–An experimental approach". In: *Marine pollution bulletin* 136, pp. 385–393.

Crounse, BC, EJ Wannamaker, and EE Adams (2007). "Integral model of a multiphase plume in quiescent stratification". In: *Journal of Hydraulic Engineering* 133.1, pp. 70–76.

Socolofsky, Scott A, E Eric Adams, and Christopher R Sherwood (2011). "Formation dynamics of subsurface hydrocarbon intrusions following the Deepwater Horizon blowout". In: *Geophysical Research Letters* 38.9.

Yang, Di, Bicheng Chen, Scott A Socolofsky, Marcelo Chamecki, and Charles Meneveau (2016). "Large-eddy simulation and parameterization of buoyant plume dynamics in stratified flow". In: *Journal of Fluid Mechanics* 794, pp. 798–833.

Masutani, Stephen M and E Eric Adams (2001). "Experimental study of multiphase plumes with application to deep ocean oil spills". In: *Final report to the US Department of Interior, Minerals Management Service* 147, p. 147.

Eggers, Jens (1997). "Nonlinear dynamics and breakup of free-surface flows". In: *Reviews of modern physics* 69.3, p. 865.

Homma, Shunji, Jiro Koga, Shiro Matsumoto, Museok Song, and Grétar Tryggvason (2006). "Breakup mode of an axisymmetric liquid jet injected into another immiscible liquid". In: *Chemical engineering science* 61.12, pp. 3986–3996.

Martínez-Bazán, Carlos, JL Montanes, and Juan C Lasheras (1999). "On the breakup of an air bubble injected into a fully developed turbulent flow. Part 2. Size PDF of the resulting daughter bubbles". In: *Journal of Fluid Mechanics* 401, pp. 183–207.

Zhao, Lin, Jagadish Torlapati, Michel C Boufadel, Thomas King, Brian Robinson, and Kenneth Lee (2014b). "VDROP: A comprehensive model for

droplet formation of oils and gases in liquids-Incorporation of the interfacial tension and droplet viscosity". In: *Chemical Engineering Journal* 253, pp. 93–106.

Cohen, Ruben D (1990). "Steady-state cluster size distribution in stirred suspensions". In: *Journal of the Chemical Society, Faraday Transactions* 86.12, pp. 2133–2138.

Aiyer, AK, Di Yang, Marcelo Chamecki, and Charles Meneveau (2019). "A population balance model for large eddy simulation of polydisperse droplet evolution". In: *Journal of Fluid Mechanics* 878, pp. 700–739.

North, Elizabeth W, E Eric Adams, Zachary Schlag, Christopher R Sherwood, Ruoying He, Kyung Hoon Hyun, and Scott A Socolofsky (2011). "Simulating oil droplet dispersal from the Deepwater Horizon spill with a Lagrangian approach". In: *Geophys. Monogr. Ser* 195, pp. 217–226.

Socolofsky, Scott A, E Eric Adams, Michel C Boufadel, Zachary M Aman, Øistein Johansen, Wolfgang J Konkel, David Lindo, Mads N Madsen, Elizabeth W North, Claire B Paris, et al. (2015). "Intercomparison of oil spill prediction models for accidental blowout scenarios with and without subsea chemical dispersant injection". In: *Marine pollution bulletin* 96.1-2, pp. 110–126.

Aman, Zachary M, Claire B Paris, Eric F May, Michael L Johns, and David Lindo-Atichati (2015). "High-pressure visual experimental studies of oil-in-water dispersion droplet size". In: *Chemical Engineering Science* 127, pp. 392–400.

Zhang, Wenming and David Z Zhu (2014). "Trajectories of air-water bubbly jets in crossflows". In: *Journal of Hydraulic Engineering* 140.7, p. 06014011.

Smith, SH and MG Mungal (1998). "Mixing, structure and scaling of the jet in crossflow". In: *Journal of fluid mechanics* 357, pp. 83–122.

Decrop, Boudewijn, Tom De Mulder, Erik Toorman, and Marc Sas (2015). "Large-eddy simulations of turbidity plumes in crossflow". In: *European Journal of Mechanics-B/Fluids* 53, pp. 68–84.

Fric, TF and A Roshko (1994). "Vortical structure in the wake of a transverse jet". In: *Journal of Fluid Mechanics* 1994, pp. 1–47.

Kelso, Richard Malcolm, TT Lim, and AE Perry (1996). "An experimental study of round jets in cross-flow". In: *Journal of fluid mechanics* 306, pp. 111–144.

Squires, Kyle D and John K Eaton (1990). "Particle response and turbulence modification in isotropic turbulence". In: *Physics of Fluids A: Fluid Dynamics* 2.7, pp. 1191–1203.

Feng, Jinyong and Igor A Bolotnov (2017). "Evaluation of bubble-induced turbulence using direct numerical simulation". In: *International Journal of Multiphase Flow* 93, pp. 92–107.

Ferrand, V, Rudy Bazile, J Borée, and Georges Charnay (2003). "Gas–droplet turbulent velocity correlations and two-phase interaction in an axisymmetric jet laden with partly responsive droplets". In: *International journal of multiphase flow* 29.2, pp. 195–217.

Lee, Joseph Hun-wei and Vincent Chu (2012). *Turbulent jets and plumes: a Lagrangian approach*. Springer Science & Business Media.

Bellani, Gabriele, Margaret L Byron, Audric G Collignon, Colin R Meyer, and Evan A Variano (2012). "Shape effects on turbulent modulation by

large nearly neutrally buoyant particles". In: *Journal of Fluid Mechanics* 712, pp. 41–60.

Bunner, Bernard and Grétar Tryggvason (2003). "Effect of bubble deformation on the properties of bubbly flows". In: *Journal of Fluid Mechanics* 495, pp. 77–118.

Rensen, J and Véronique Roig (2001). "Experimental study of the unsteady structure of a confined bubble plume". In: *International journal of multiphase flow* 27.8, pp. 1431–1449.

Morton, BR, Geoffrey Ingram Taylor, and John Stewart Turner (1956). "Turbulent gravitational convection from maintained and instantaneous sources". In: *Proceedings of the Royal Society of London. Series A. Mathematical and Physical Sciences* 234.1196, pp. 1–23.

Turner, JS (1986). "Turbulent entrainment: the development of the entrainment assumption, and its application to geophysical flows". In: *Journal of Fluid Mechanics* 173, pp. 431–471.

Carlotti, Pierre and Gary R Hunt (2005). "Analytical solutions for turbulent non-Boussinesq plumes". In: *Journal of Fluid Mechanics* 538, pp. 343–359.

Dissanayake, Anusha L, Jonas Gros, and Scott A Socolofsky (2018). "Integral models for bubble, droplet, and multiphase plume dynamics in stratification and crossflow". In: *Environmental Fluid Mechanics* 18.5, pp. 1167–1202.

Rooney, GG and PF Linden (1996). "Similarity considerations for non-Boussinesq plumes in an unstratified environment". In: *Journal of fluid mechanics* 318, pp. 237–250.

Reeuwijk, Maarten van and John Craske (2015). "Energy-consistent entrainment relations for jets and plumes". In: *Journal of Fluid Mechanics* 782, pp. 333–355.

Brandvik, Per Johan, Chris Storey, Emlyn John Davies, and Frode Leirvik (2019). "Quantification of oil droplets under high pressure laboratory experiments simulating deep water oil releases and subsea dispersants injection (SSDI)". In: *Marine pollution bulletin* 138, pp. 520–525.

Landeau, M., R. Deguen, and P. Olson (2014). "Experiments on the fragmentation of a buoyant liquid volume in another liquid". In: *Journal of Fluid Mechanics* 749, 478—518.

Saito, Shimpei, Yutaka Abe, and Kazuya Koyama (2017). "Flow transition criteria of a liquid jet into a liquid pool". In: *Nuclear Engineering and Design* 315, pp. 128–143.

Boufadel, Michel C, Scott Socolofsky, Joseph Katz, Di Yang, Cosan Daskiran, and William Dewar (2020). "A Review on Multiphase Underwater Jets and Plumes: Droplets, Hydrodynamics, and Chemistry". In: *Reviews of Geophysics*, e2020RG000703.

Murphy, David W, Cheng Li, Vincent d'Albignac, David Morra, and Joseph Katz (2015). "Splash behaviour and oily marine aerosol production by raindrops impacting oil slicks". In: *Journal of Fluid Mechanics* 780, p. 536.

Brandvik, Per Johan, Øistein Johansen, Frode Leirvik, Umer Farooq, and Per S Daling (2013). "Droplet breakup in subsurface oil releases–Part 1: Experimental study of droplet breakup and effectiveness of dispersant injection". In: *Marine Pollution Bulletin* 73.1, pp. 319–326.

Brandvik, PJ, Ø Johansen, U Farooq, G Angell, and F Leirvik (2014). "Subsur-
face oil releases–Experimental study of droplet distributions and different
dispersant injection techniques Version 2". In: *SINTEF Report No. A26122*.

Malkiel, Edwin, Jian Sheng, Joseph Katz, and J Rudi Strickler (2003). "The
three-dimensional flow field generated by a feeding calanoid copepod
measured using digital holography". In: *Journal of Experimental Biology*
206.20, pp. 3657–3666.

Sheng, Jian, Edwin Malkiel, and Joseph Katz (2006). "Digital holographic
microscope for measuring three-dimensional particle distributions and
motions". In: *Applied optics* 45.16, pp. 3893–3901.

Gopalan, Balaji, Edwin Malkiel, and Joseph Katz (2008). "Experimental in-
vestigation of turbulent diffusion of slightly buoyant droplets in locally
isotropic turbulence". In: *Physics of Fluids* 20.9, p. 095102.

Katz, Joseph and Jian Sheng (2010). "Applications of holography in fluid
mechanics and particle dynamics". In: *Annual Review of Fluid Mechanics* 42,
pp. 531–555.

Talapatra, Siddharth, Jiarong Hong, Malcolm McFarland, Aditya R Nayak,
Cao Zhang, Joseph Katz, James Sullivan, Michael Twardowski, Jan Rines,
and Percy Donaghay (2013). "Characterization of biophysical interactions
in the water column using in situ digital holography". In: *Marine Ecology
Progress Series* 473, pp. 29–51.

Gopalan, Balaji and Joseph Katz (2010). "Turbulent shearing of crude oil
mixed with dispersants generates long microthreads and microdroplets".
In: *Physical review letters* 104.5, p. 054501.

Zhao, Lin, Michel C Boufadel, Scott A Socolofsky, Eric Adams, Thomas King, and Kenneth Lee (2014a). "Evolution of droplets in subsea oil and gas blowouts: Development and validation of the numerical model VDROP-J". In: *Marine Pollution Bulletin* 83.1, pp. 58–69.

Li, Zhengkai, Kenneth Lee, Thomas King, Michel C Boufadel, and Albert D Venosa (2008). "Oil droplet size distribution as a function of energy dissipation rate in an experimental wave tank". In: *International Oil Spill Conference*. Vol. 2008. 1. American Petroleum Institute, pp. 621–626.

Reid, Jeffrey S and Peter V Hobbs (1998). "Physical and optical properties of young smoke from individual biomass fires in Brazil". In: *Journal of Geophysical Research: Atmospheres* 103.D24, pp. 32013–32030.

Murphy, David W, Xinzhi Xue, Kaushik Sampath, and Joseph Katz (2016). "Crude oil jets in crossflow: Effects of dispersant concentration on plume behavior". In: *Journal of Geophysical Research: Oceans* 121.6, pp. 4264–4281.

Münch, Beat, Pavel Trtik, Federica Marone, and Marco Stampanoni (2009). "Stripe and ring artifact removal with combined wavelet—Fourier filtering". In: *Optics express* 17.10, pp. 8567–8591.

Arganda-Carreras, Ignacio, Verena Kaynig, Curtis Rueden, Kevin W Eliceiri, Johannes Schindelin, Albert Cardona, and H Sebastian Seung (2017). "Trainable Weka Segmentation: a machine learning tool for microscopy pixel classification". In: *Bioinformatics* 33.15, pp. 2424–2426.

Wu, Jin, Michael Halter, Raghu N Kacker, John T Elliot, and Anne L Plant (2013). *Measurement uncertainty in cell image segmentation data analysis*. Tech. rep. National Institute of Standards and Technology. DOI: 10.6028/nist.ir.7954.

Xue, Xinzhi and Joseph Katz (2019). "Formation of compound droplets during fragmentation of turbulent buoyant oil jet in water". In: *Journal of Fluid Mechanics* 878, pp. 98–112.

Liepmann, Dorian and Morteza Gharib (1992). "The role of streamwise vorticity in the near-field entrainment of round jets". In: *Journal of Fluid Mechanics* 245, pp. 643–668.

Amiri, A, F Larachi, and SM Taghavi (2016). "Buoyant miscible displacement flows in vertical pipe". In: *Physics of Fluids* 28.10, p. 102105.

Hasnain, A, E Segura, and K Alba (2017). "Buoyant displacement flow of immiscible fluids in inclined pipes". In: *Journal of Fluid Mechanics* 824, p. 661.

Crow, S Cj and FH Champagne (1971). "Orderly structure in jet turbulence". In: *Journal of Fluid Mechanics* 48.3, pp. 547–591.

Wu, P-K, RF Miranda, and GM Faeth (1995). "Effects of initial flow conditions on primary breakup of nonturbulent and turbulent round liquid jets". In: *Atomization and sprays* 5.2.

Brennen, Christopher E (2005). *Fundamentals of multiphase flow*. Cambridge university press.

Simmons, HC (1977). "The correlation of drop-size distributions in fuel nozzle sprays". In: *Journal of Engineering for Power* 99.3, pp. 309–319.

Stone, HA and LG Leal (1990). "Breakup of concentric double emulsion droplets in linear flows". In: *Journal of Fluid Mechanics* 211, pp. 123–156.

Mandal, Shubhadeep, Uddipta Ghosh, and Suman Chakraborty (2016). "Effect of surfactant on motion and deformation of compound droplets in arbitrary unbounded Stokes flows". In: *Journal of Fluid Mechanics* 803, pp. 200–249.

Kim, Sangkyu and Sadegh Dabiri (2017). "Transient dynamics of eccentric double emulsion droplets in a simple shear flow". In: *Physical Review Fluids* 2.10, p. 104305.

Smith, KA, Julio M Ottino, and M Olvera de la Cruz (2004). "Encapsulated drop breakup in shear flow". In: *Physical review letters* 93.20, p. 204501.

Roth, GI and J Katz (2001). "Five techniques for increasing the speed and accuracy of PIV interrogation". In: *Measurement Science and Technology* 12.3, p. 238.

Lai, Chris CK and Scott A Socolofsky (2019). "Budgets of turbulent kinetic energy, Reynolds stresses, and dissipation in a turbulent round jet discharged into a stagnant ambient". In: *Environmental Fluid Mechanics* 19.2, pp. 349–377.

Todde, Valentino, Pier Giorgio Spazzini, and Mats Sandberg (2009). "Experimental analysis of low-Reynolds number free jets". In: *Experiments in fluids* 47.2, pp. 279–294.

Burridge, HC, DA Parker, ES Kruger, Jamie Partridge, and Paul Linden (2017). "Conditional sampling of a high Péclet number turbulent plume and the implications for entrainment". In: *Journal of Fluid Mechanics* 823, pp. 26–56.

Panchapakesan, NR and JL Lumley (1993b). "Turbulence measurements in axisymmetric jets of air and helium. Part 2. Helium jet". In: *Journal of Fluid Mechanics* 246, pp. 225–247.

Papanicolaou, Panos N and E John List (1988). "Investigations of round vertical turbulent buoyant jets". In: *Journal of Fluid Mechanics* 195, pp. 341–391.

Djeridane, T, M Amielh, F Anselmet, and L Fulachier (1996). "Velocity turbulence properties in the near-field region of axisymmetric variable density jets". In: *Physics of Fluids* 8.6, pp. 1614–1630.

Drew, D. A. and R. T. Jr. Lahey (1993). "Analytical modeling of multiphase flow". In: *Particulate two-phase flow*. Ed. by M. C. Roco. Butterworth-Heinemann, pp. 509–566.

Friedman, PD and J Katz (2002). "Mean rise rate of droplets in isotropic turbulence". In: *Physics of Fluids* 14.9, pp. 3059–3073.

Silva, Carlos B da, Julian CR Hunt, Ian Eames, and Jerry Westerweel (2014). "Interfacial layers between regions of different turbulence intensity". In: *Annual review of fluid mechanics* 46, pp. 567–590.

Da Silva, Carlos B, Rodrigo R Taveira, and Guillem Borrell (2014). "Characteristics of the turbulent/nonturbulent interface in boundary layers, jets and shear-free turbulence". In: *Journal of Physics: Conference Series*. Vol. 506. 1. IOP Publishing, p. 012015.

Taveira, Rodrigo R, José S Diogo, Diogo C Lopes, and Carlos B da Silva (2013). "Lagrangian statistics across the turbulent-nonturbulent interface in a turbulent plane jet". In: *Physical Review E* 88.4, p. 043001.

Vita

Place of birth: Daqing, Heilongjiang, China

Year of birth: 1991

EDUCATION

Johns Hopkins University
  Ph.D., Mechanical Engineering   August, 2020
Johns Hopkins University
  M.S., Mechanical Engineering   December, 2015
Harbin Institute of Technology
  B.E., Mechanical Engineering Honors School   July, 2013

PUBLICATIONS

Journal Articles

Xue, X., Chandrala, L., Katz, J. (2020) Flow structure and turbulence in the near field of an immiscible buoyant oil jet. _Physical Review Fluids, Submitted._

Daskiran, C., **Xue, X.**, Cui, F., Katz, J., Boufadel, M.C. (2020) Large eddy simulation and experiment of shear breakup in liquid-liquid jet: formation of ligaments and droplets. _International Journal of Multiphase Flow, Submitted._

Xue, X., Katz, J. (2019) Formation of compound droplets during fragmentation of turbulent buoyant oil jet in water. _Journal of Fluid Mechanics_, 878, 98-112.

Murphy, D., **Xue, X.**, Sampath, K., Katz, J. (2016) Crude oil jets in crossflow: effects of dispersant concentration on plume behavior. _Journal of Geophysical Research: Oceans_, 121 (6), 4264-4281.

Li, S., Aung, N. Z., Zhang, S., Cao, J., **Xue, X.** (2013). Experimental and numerical investigation of the cavitation phenomenon in flapper–nozzle pilot stage of an electrohydraulic servo-valve. _Computers & Fluids_, 88, 590-598.

Conference Proceeding

Xue, X., Katz, J. (2017) Refractive index matched visualization and particle image velocimetry measurements of the initial breakup of turbulent oil jet. _International Oil Spill Conference Proceedings 2017_, (1), 2017328

CONFERENCE PRESENTATIONS

Xue, X., Katz, J. (2020). Measurements of flow structure and turbulence in the nearfield of an oil jet in water. *The Gulf of Mexico Oil Spill & Ecosystem Science Conference 2020,* February 3-7, Tampa, FL.

Xue, X., Katz, J. (2019). Formation of compound droplets by turbulent buoyant oil jet and plume. *The 42nd AMOP Technical Seminar on Environmental Contamination and Response,* June 4-6, Halifax, Canada.

Xue, X., Katz, J. (2019). Fragmentation of a turbulent buoyant oil jet in water. *The 9th International Conference on Multiphase Flow,* May 19-24, Rio de Janeiro, Brazil.

Xue, X., Katz, J. (2019). Simultaneous PLIF and PIV measurements on refractive index-matched immiscible buoyant oil jet fragmentation in water. *The Gulf of Mexico Oil Spill & Ecosystem Science Conference 2019,* February 4-7, New Orleans, LA.

Xue, X., Katz, J. (2018). Experimental statistics of compound droplets generated by immiscible buoyant oil jet fragmentation in water. *The 71st Annual Meeting of the APS Division of Fluid Dynamics,* November 18-20, Atlanta, GA.

Li, C., Murphy, D., Sampath, K., **Xue, X.,** Chandrala, L., AfsharMohajer, N., Nishida, K., Ronzhes, Y., Koehler, K., Sidhaye, R., Katz, J. (2018). Dispersion and health impacts of crude oil spills by physical and chemical processes. *The ASLO 2018 Summer Meeting,* June 10-15, Victoria, Canada.

Xue, X., Katz, J. (2017). Simultaneous PLIF and PIV measurement of a near field turbulent immiscible buoyant oil jet fragmentation in water using liquid-liquid refractive index matching. *The 70th Annual Meeting of the APS Division of Fluid Dynamics,* November 19-21, Denver, CO.

Xue, X., Katz, J. (2017). Index-matched simultaneous laser induced-fluorescence and particle image velocimetry measurement of oil jet fragmentation. *The 12th International Symposium on Particle Image Velocimetry,* June 19-21, Busan, Korea.

Xue, X., Katz, J. (2017). Refractive index-matched turbulent immiscible buoyant oil jet breakup in water. *The Gulf of Mexico Oil Spill & Ecosystem Science Conference 2017*, February 6-9, New Orleans, LA.

Xue, X., Katz, J. (2016). Experimental study on immiscible jet breakup using refractive index matched oil-water pair. *The 69th Annual Meeting of the APS Division of Fluid Dynamics*, November 20-22, Portland, OR.

Murphy, D., **Xue, X.**, Katz, J. (2016). Turbulent crude oil plumes in crossflow: Effect of counter-rotating vortex pair structures on oil residence in plume. *The 9th International Conference on Multiphase Flow*, May 22-27, Firenze, Italy.

Xue, X., Murphy, D., Sampath, K., Katz, J. (2016). Turbulent crude oil plume in crossflow: Effect of vortex structures on oil residence in plume. *The Gulf of Mexico Oil Spill & Ecosystem Science Conference 2016*, February 1-4, Tampa, FL.

Xue, X., Murphy, D., Katz, J. (2015). Turbulent crude oil jets in crossflow: Holographic measurements of droplet size distributions. *The 68th Annual Meeting of the APS Division of Fluid Dynamics*, November 22-24, Boston, MA.

Murphy, D., **Xue, X.**, & Katz, J. (2015). Turbulent crude oil jets in crossflow. *The Gulf of Mexico Oil Spill & Ecosystem Science Conference 2015*, February 16-19, Houston, TX.